

INFORMATION TO USERS

The most advanced technology has been used to photograph and reproduce this manuscript from the microfilm master. UMI films the text directly from the original or copy submitted. Thus, some thesis and dissertation copies are in typewriter face, while others may be from any type of computer printer.

The quality of this reproduction is dependent upon the quality of the copy submitted. Broken or indistinct print, colored or poor quality illustrations and photographs, print bleedthrough, substandard margins, and improper alignment can adversely affect reproduction.

In the unlikely event that the author did not send UMI a complete manuscript and there are missing pages, these will be noted. Also, if unauthorized copyright material had to be removed, a note will indicate the deletion.

Oversize materials (e.g., maps, drawings, charts) are reproduced by sectioning the original, beginning at the upper left-hand corner and continuing from left to right in equal sections with small overlaps. Each original is also photographed in one exposure and is included in reduced form at the back of the book. These are also available as one exposure on a standard 35mm slide or as a 17" x 23" black and white photographic print for an additional charge.

Photographs included in the original manuscript have been reproduced xerographically in this copy. Higher quality 6" x 9" black and white photographic prints are available for any photographs or illustrations appearing in this copy for an additional charge. Contact UMI directly to order.



University Microfilms International
A Bell & Howell Information Company
300 North Zeeb Road, Ann Arbor, MI 48106-1346 USA
313/761-4700 800/521-0600



Order Number 8909849

**Radiation, scattering, and guidance of electromagnetic fields by
conducting objects of arbitrary shape in layered media**

Zheng, Dalian, Ph.D.

The University of Mississippi, 1988

U·M·I
300 N. Zeeb Rd.
Ann Arbor, MI 48106



RADIATION, SCATTERING, AND GUIDANCE OF ELECTROMAGNETIC
FIELDS BY CONDUCTING OBJECTS OF ARBITRARY SHAPE
IN LAYERED MEDIA

BY

DALIAN ZHENG

B.E., Beijing Institute of Aeronautics and Astronautics, 1982
M.S., The Ohio State University, 1985

A Dissertation
Submitted to the Faculty of
The University of Mississippi
in Partial Fulfillment of the Requirements
for the Degree of Doctor of Philosophy
in the School of Engineering

The University of Mississippi

December, 1988

RADIATION, SCATTERING, AND GUIDANCE OF ELECTROMAGNETIC
FIELDS BY CONDUCTING OBJECTS OF ARBITRARY SHAPE
IN LAYERED MEDIA

BY

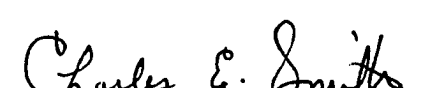
DALIAN ZHENG



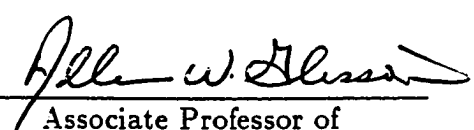
Allen M. Smith
Dean of the School of
Engineering



R.A. Mishalshin
Adjunct Associate Professor of
Electrical Engineering
(Director of Dissertation)



Charles E. Smith
Professor and Chairman of the
Department of Electrical
Engineering



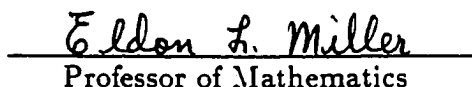
Allen W. Glaser
Associate Professor of
Electrical Engineering
(Co-Director of Dissertation)



Michael H. Engleman
Dean of the Graduate School



Wesham A. Andra
Assistant Professor
Electrical Engineering



Eldon L. Miller
Professor of Mathematics

ABSTRACT

RADIATION, SCATTERING, AND GUIDANCE OF ELECTROMAGNETIC FIELDS BY CONDUCTING OBJECTS OF ARBITRARY SHAPE IN LAYERED MEDIA

ZHENG, DALIAN. B.E., Beijing Institute of Aeronautics and Astronautics, 1982. M.S., The Ohio State University, 1985. Ph.D., The University of Mississippi, 1988. Dissertation directed by Dr. Krzysztof A. Michalski.

A rigorous and general procedure is developed for the analysis of radiation, scattering, and guidance of electromagnetic fields by conducting objects of arbitrary shape embedded in a medium consisting of an arbitrary number of planar, dielectric layers. The key step in this procedure is the transformation of the electric field integral equation into a mixed-potential form, which is amenable to well-established numerical solution techniques originally developed for arbitrarily-shaped objects in free space. Three alternative mixed-potential electric field integral equations are derived and their relative merits discussed. One of them, called Formulation C, which is found to be particularly well suited for the application of the moment method, is implemented to analyze problems involving arbitrarily-shaped, open or closed, conducting surfaces, which penetrate the interface between contiguous dielectric half-spaces. Thin wire structures are included as special cases. Formulation C is also specialized to the case of an open transmission line consisting of an infinite conductor of arbitrary cross-section embedded in a grounded dielectric slab. Numerical results are presented for cases of interest and, where possible, are compared with published computed and measured data.

ACKNOWLEDGMENTS

The author sincerely acknowledges the guidance and assistance rendered by the dissertation director, Dr. Krzysztof A. Michalski.

The advice and comments provided by the members of the Doctoral Committee, consisting of Dr. Krzysztof A. Michalski, Dr. Allen W. Glisson, and Dr. Hesham A. Auda from the Department of Electrical Engineering, and Dr. Eldon L. Miller from the Mathematics Department, are gratefully acknowledged. The numerous technical discussions and suggestions of Dr. Allen W. Glisson are especially appreciated.

The author wished to express special thanks to Dr. Donald R. Wilton (University of Houston) for useful comments regarding this research, and to Dr. Charles E. Smith, Dr. Xiao-bang Xu (Clemson University), and Gerald J. Burke (Lawrence Livermore National Laboratory), who provided measured and computed data to corroborate our results.

The support of the National Science Foundation under Grant No. ECS-8505678 and of the Office of Naval Research under Contract No. N00014-87-K-0688 is gratefully acknowledged. It is also a pleasure to acknowledge the expert typing of Clifford D. Krumvieda.

Last, but not least, the author wishes to thank his wife, Luo Yan, for her encouragement and assistance throughout his graduate studies.

TABLE OF CONTENTS

	Page
LIST OF TABLES.....	vii
LIST OF FIGURES.....	viii
Chapter	
1. INTRODUCTION.....	1
2. PRELIMINARIES.....	6
2.1. Statement of the Problem	6
2.2. Electric Field Integral Equation (EFIE).....	6
2.3. Mixed-Potential EFIE (MPIE)	10
3. DERIVATION OF GREEN'S FUNCTIONS FOR	
THE MAGNETIC VECTOR POTENTIAL.....	14
3.1. Reduction of Maxwell's Equations to Transmission-line	
Equations for Sources in Layered Media	14
3.2. Solution of Transmission-line Equations.....	23
3.3. Derivation of the Dyadic Green's Functions for the	
Magnetic Vector Potential in a Plane-Stratified Medium	29
3.3.1. Traditional Form of the Green's Function.....	32
3.3.2. Alternative Form of the Green's Function	34
3.4 Electric Field in the Layered Medium due to	
Plane Wave Incident in Region 1	35

Chapter	Page
4. FORMULATION OF THE MIXED-POTENTIAL ELECTRIC FIELD INTEGRAL EQUATION	37
4.1. Formulation A	38
4.2. Formulation B	40
4.3. Formulation C	43
4.4. Discussion.....	46
5. NUMERICAL METHOD.....	50
5.1. Surface of Arbitrary Shape	53
5.2. Thin Wire of Arbitrary Shape	59
5.3. Transmission Line of Arbitrary Cross-Section	64
6. NUMERICAL EVALUATION OF SOMMERFELD INTEGRALS.....	72
6.1. Sommerfeld Integrals for the Half-Space Problem	72
6.2. Sommerfeld Integrals for the Transmission Line Problem	89
7. NUMERICAL RESULTS.....	97
7.1. Sufaces.....	97
7.2. Thin Wires	104
7.3. Open Microstrip Lines	111

Chapter	Page
8. CONCLUSION.....	129
APPENDIX. KERNEL ELEMENTS OF FORMULATION C FOR CONTIGUOUS HALF-SPACES AND FOR A GROUNDED SLAB.....	132
A.1. Kernel Elements for Contiguous Half-Spaces.....	132
A.2. Kernel Elements for a Grounded Slab	135
REFERENCES	138
BIOGRAPHICAL SKETCH OF THE AUTHOR	145

LIST OF TABLES

Table	Page
4.1. Summary of the properties of the three mixed-potential formulations	47

LIST OF FIGURES

Figure	Page
2.1. Scatterer of arbitrary shape embedded in a layered dielectric medium.....	7
2.2. (a) Arbitrarily shaped surface penetrating two adjacent interfaces. (b) Detail of contour C_i with unit vectors \hat{u}_i , \hat{t}_i and \hat{n}_i	13
3.1. (a) Plane-stratified dielectric medium and (b) its transmission-line network representation.....	15
3.2. Definition of the distance ξ and angle ζ	17
3.3. Reflection coefficients and impedances associated with the i th interface... 21	
3.4. (a) Voltage source and (b) current source in the i th transmission-line section.....	26
5.1. A PEC object of arbitrary shape embedded in (a) contiguous half-spaces, and (b) a grounded slab.....	51
5.2. Triangle-patch model of an arbitrary surface penetrating the interface between dissimilar media.....	54
5.3. Local coordinates associated with an edge.....	55
5.4. (a) Side view and (b) cross-sectional view of a triangle pair straddling the interface between contiguous half-spaces.....	58
5.5. Straight segment model of a thin-wire of arbitrary shape penetrating the interface between dissimilar media.....	60
5.6. Straight line segment model of a cylinder of arbitrary cross-section embedded in a grounded slab.....	65
6.1. Two sheets of the k_{zi}^2 -plane. (a) Top sheet ($\text{Im}(k_{zi}) < 0$) and (b) bottom sheet ($\text{Im}(k_{zi}) > 0$).....	75
6.2. Two sheets of k_p^2 -plane. (a) Top sheet ($\text{Im}(k_{zi}) < 0$) and (b) bottom sheet ($\text{Im}(k_{zi}) > 0$).....	76
6.3. The two-sheeted k_p -plane. (a) Top sheet ($\text{Im}(k_{zi}) < 0$) and (b) bottom sheet ($\text{Im}(k_{zi}) > 0$).....	77

Figure	Page
6.4. (a) The k_ρ -plane showing the branch cuts for k_{z1} and k_{z2} . (b) The Riemann surface of four sheets in the k_ρ -plane.	78
6.5. Various integration paths of (a) Path I, (b) Path II, (c) Path III and (d) Path IV in the complex k_ρ -plane.	81
6.6. Schematic view of the selection of integration paths.	90
6.7. The k_x -plane showing the branch cuts, the poles and the integration paths for (a) bound modes, region (i), (b) leaky modes, region (ii) and (c) leaky modes, region (iii).	94
6.8. Various integration paths in the computer implementation for (a) bound modes, region (i), (b) leaky modes, region (ii) and (c) leaky modes, region (iii).	96
7.1. (a) Inclined thin-wire antenna partially buried in earth and (b) its strip model.	98
7.2. Current distribution on the strip model of Fig. 7.1 for (a) $\alpha = 45^\circ$ and (b) $\alpha = 80^\circ$	99
7.3. Vertical, cylindrical antenna penetrating the interface between two media. The antenna is approximated by triangular patches.	101
7.4. Current distribution on an open-ended and closed cylindrical antenna of Fig. 7.3 partially buried in (a) dry earth and (b) salt water.	102
7.5. (a) Magnitude and (b) phase of the current J_t on a horizontal tube partially buried in a dielectric medium. The current is normalized to the incident magnetic field at $\phi = 90^\circ$ on the surface of the tube.	103
7.6. (a) Magnitude and (b) phase of the current J_t along the center line of a rectangular plate partially buried in dry earth for the inclination angle $\alpha = 30^\circ$. The current is normalized to the incident magnetic field at $l_0 = 0.125$ m.	105
7.7. Magnitude of (a) the longitudinal and (b) the transverse component of the current induced on the rectangular plate of Fig. 7.6 for $\alpha = 30^\circ$ by a normally-incident plane wave with $H_x^i = 1$ A/m.	106

Figure	Page
7.8. (a) Magnitude and (b) phase of the current J_l along the center line of a rectangular plate of Fig. 7.6 for $\alpha = 60^\circ$. The current is normalized to the incident magnetic field at $l_0 = 0.125$	107
7.9. Magnitude of (a) the longitudinal and (b) the transverse component of the current induced on the rectangular plate of 7.6 for $\alpha = 60^\circ$ by a normally-incident plane wave with $H_x^i = 1 \text{ A/m}$	108
7.10. Inclined thin-wire antenna partially buried in moist earth.	109
7.11. Current distribution on the antenna of Fig. 7.10 for (a) $\alpha = 45^\circ$ and (b) $\alpha = 80^\circ$	110
7.12. Vertical, rectangular, loop antenna partially immersed in water.....	112
7.13. (a) Magnitude and (b) phase of the current J_l on the lower arm of the antenna of Fig. 7.12 ($\epsilon_r = 81$, $\sigma = 0$). The current is normalized to its value at the point $l_0 = 0$	113
7.14. (a) Magnitude and (b) phase of the current J_l on the lower arm of the antenna of Fig. 7.12 ($\epsilon_r = 79$, $\sigma = 1 \text{ S/m}$). The current is normalized to its value at the point $l_0 = 23.3 \text{ cm}$	114
7.15. (a) Magnitude and (b) phase of the current J_l on the lower arm of the antenna of Fig. 7.12 ($\epsilon_r = 76$, $\sigma = 1.75 \text{ S/m}$). The current is normalized to its value at the point $l_0 = 23.3 \text{ cm}$	115
7.16. Open microstrip line.....	116
7.17. Variation with frequency (a) of the normalized phase constant for the lowest mode (EH_0) and the first higher mode (EH_1), and (b) of the normalized attenuation constant for the EH_1 modes. The microstrip line dimensions are: $w = 1.5 \text{ cm}$, $d = 0.794 \text{ mm}$, $\epsilon_r = 2.32$	117
7.18. (a) Longitudinal and (b) transverse current distribution of the EH_0 mode at $f = 5 \text{ GHz}$ and $f = 10 \text{ GHz}$ for an infinitely thin microstrip with $w = 1.5 \text{ cm}$, $d = 0.794 \text{ mm}$, and $\epsilon_r = 2.32$	118

Figure	Page
7.19. (a) Longitudinal and (b) transverse current distribution of the EH_1 mode at $f = 5 \text{ GHz}$ (leaky regime (iii)) and $f = 10 \text{ GHz}$ (bound regime (i)) for the microstrip: $w = 1.5 \text{ cm}$, $d = 0.794 \text{ mm}$, $t/w = 0.$, $\epsilon_r = 2.32$	119
7.20. (a) Longitudinal and (b) transverse current distribution of the EH_0 mode at $f = 5 \text{ GHz}$ and $f = 10 \text{ GHz}$ for the microstrip line with finite thickness: $w = 1.5 \text{ cm}$, $d = 0.794 \text{ mm}$, $t/w = 0.1$, $\epsilon_r = 2.32$	121
7.21. (a) Longitudinal and (b) transverse current distribution of the EH_1 mode at $f = 5 \text{ GHz}$ (leaky regime (iii)) and $f = 10 \text{ GHz}$ (bound regime (i)) for the microstrip line with finite thickness with $w = 1.5 \text{ cm}$, $d = 0.794 \text{ mm}$, $t/w = 0.1$, $\epsilon_r = 2.32$	122
7.22. Variation with frequency (a) of the normalized phase constant for the lowest mode (EH_0) and the first three higher modes (EH_1 , EH_2 , EH_3), and (b) of the normalized attenuation constant for the EH_1 , EH_2 and EH_3 modes. The microstrip line dimensions are: $w = 3 \text{ mm}$, $d = 0.635 \text{ mm}$, $t/w = 0$, $\epsilon_r = 9.8$	123
7.23. Normalized phase constant for the EH_2 mode and the boundary of region (iii) corresponding to this mode.....	124
7.24. (a) Longitudinal and (b) transverse current distribution of the EH_2 mode at $f = 25 \text{ GHz}$ (leaky regime (iii)) and $f = 35 \text{ GHz}$ (bound regime (i)) for the microstrip line: $w = 3 \text{ mm}$, $d = 0.635 \text{ mm}$, $t/w = 0$, $\epsilon_r = 9.8$	125
7.25. (a) Longitudinal and (b) transverse current distribution of the EH_3 mode at $f = 35 \text{ GHz}$ (leaky regime (iii)) and $f = 50 \text{ GHz}$ (leaky regime (ii)) for the microstrip line with $w = 3 \text{ mm}$, $d = 0.635 \text{ mm}$, $t/w = 0$, $\epsilon_r = 9.8$	126
7.26. Effective dielectric constant for the lowest mode (EH_0) for a microstrip with $\epsilon_r = 9.7$	128

CHAPTER 1

INTRODUCTION

Simple and efficient method of moments (MOM) [1] procedures have recently been developed for the solution of the electromagnetic scattering and radiation problems involving objects of arbitrary shape in free space [2,3,4,5,6,7]. These procedures are based on the so-called mixed-potential form of the electric field integral equation (EFIE)—so named, because it involves both the vector and scalar potentials, the former expressed in terms of the induced current, and the latter in terms of the induced charge. In the case of perfectly electrically conducting (PEC) objects, the EFIE is more general than the magnetic field integral equation (MFIE) [8], since it is applicable to both closed and open surfaces [9]. The mixed-potential EFIE (MPIE, for short) is preferable to the several other possible variants of the EFIE, because it only requires potential forms of the Green's functions, which are less singular than their derivatives needed in other forms of the EFIE [4]. In the MOM technique originally developed by Rao, Wilton, and Glisson [5], the surface of the PEC object is modeled in terms of triangular patches and specially designed basis functions defined on pairs of adjacent triangles are used, which yield a surface current representation free of line or point charges at subdomain boundaries. This technique also employs a testing scheme in which the derivatives of the scalar potential are in effect replaced by finite differences. More recently, Schaubert, Wilton, and Glisson [10] extended this procedure to volume integral equations for penetrable bodies, which they modeled in terms of tetrahedral elements.

The procedures described above were originally developed for antennas and scatterers residing in a homogeneous space. Although this restriction is not severe in some aerospace applications where the effect of the environment can be neglected, it does exclude many problems of practical interest in which the proximity of the earth must be taken into account. Indeed, often the influence of the ground or the ocean, which in many cases can be adequately represented by a model consisting of one or more planar, dielectric layers, is the dominant effect in the problem. Therefore, in this dissertation we develop, for arbitrarily shaped objects in layered media, an MPIE formulation that is amenable to the MOM procedures originated by Wilton and his co-workers, which culminated in the development of the triangle-patch code [5,7,11], and its thin-wire counterpart, MININEC [12,13]. Since a great amount of effort went into the development of these codes, which can presently only handle objects in free space or over a PEC ground, it is desirable to have a formulation that would allow one to easily extend them to the case of bodies in stratified media. Although, for simplicity, we limit attention to PEC objects and surface integral equations, our formulation can, if desired, be easily extended to dielectric bodies in conjunction with either volume [10] or surface [6] integral equations.

Unlike in free space, or even in some complex environments with PEC boundaries, it is not a trivial task to formulate an MPIE for objects of arbitrary shape in a layered medium. This is due to the fact that in the layered medium the vector and scalar potentials are not unique [14] and that the scalar potentials of point charges associated with horizontal and vertical dipoles are not, in general, identical [15]. Additional complications arise when the objects penetrate one or more of

the interfaces between dielectric layers.

The advantages of the MPIE over the other forms of the EFIE are even more pronounced in a layered medium than in free space. This is due to the fact that the Green's functions in layered media comprise Sommerfeld-type integrals [16], which are extremely laborious to evaluate. Since the MPIE only involves potential forms of the Green's functions, rather than field forms, the Sommerfeld integrals it requires converge faster than those present in any other form of the EFIE [4].

Several researchers have previously recognized the advantages of the mixed-potential formulation in solving antenna problems in layered media. Mosig and Gardiol [17,18] have applied the MPIE in conjunction with Glisson and Wilton's [4] MOM procedure to a rectangular microstrip antenna. Johnson [19] has used a similar approach to solve the problem of a vertical cylinder penetrating the interface between contiguous half-spaces. Wilton and Singh [20] have applied an MPIE to analyze a periodic array of slots in a conducting screen backed with a layered dielectric. Michalski, Smith, and Butler [21,22] have used an MPIE to solve the problem of a horizontal two-element wire array above and on opposite sides of the interface between two media. As was pointed out in [23,24], the success of these efforts can be attributed to the fact that the structures considered could only support either vertical or horizontal components of the current. To our knowledge, an MPIE for arbitrarily shaped objects in a layered medium was first published in [24]. However, it was assumed in that paper that the antenna or scatterer was confined to a single layer. In a two-dimensional case, an MPIE has been derived by Xu [25].

Numerous papers have been published on the subject of antennas and scatterers in layered media, but—with the exception of the geophysics literature—most of

them only deal with planar geometries, such as microstrip antennas, transmission lines, etc. Since the emphasis here is on objects of arbitrary shape, we reference only a few of these papers, to conserve space. The problem of arbitrarily shaped thin wires which are near to or penetrate an interface between contiguous half-spaces has been solved by Burke and Miller [26]. However, their approach, which is implemented in the powerful Numerical Electromagnetics Code (NEC) [27], is not easily extendable to arbitrary surfaces. From the many works devoted to electromagnetic modeling of buried inhomogeneities in the context of geophysical prospecting, we only mention the recent representative papers by Hohmann [28] and by Wan-namaker, Hohmann, and SanFilipo [29]. These authors use the volume integral equation technique in conjunction with a rather crude—but entirely adequate in the quasi-static regime—MOM procedure employing piece-wise constant current expansion and point-matching [1]. To overcome the problems associated with the singular behavior of the electric Green's function, Hohmann [28] employed a mixed-potential formulation, but only to the primary (or whole-space) component of the kernel; the part comprising the Sommerfeld integrals was left in the slowly convergent field form. Mention should also be made of the work by Karlsson and Kristensson [30], who employed the extended boundary condition integral equation in conjunction with the T-matrix approach to compute the field scattered by obstacles buried in a stratified ground. This method, however, is only applicable to closed, smooth bodies and is only practical for simple shapes.

The outline of this dissertation is as follows. Chapter 2 contains the statement of the problem and a general discussion of various forms of the EFIE in a layered medium. In Chapter 3, alternative forms of the vector potential Green's function

are derived for the layered medium. These are utilized in Chapter 4, where three alternative mixed-potential formulations, referred to as Formulations A, B and C, are developed for arbitrarily shaped PEC objects. Formulation C, which is found to be particularly well suited for the application of the moment method, is specialized in the Appendix to two particularly important situations, where the object resides in contiguous half-spaces or is partially embedded in a grounded dielectric slab. In Chapter 5, the MOM procedures introduced in [4,5,7] are adapted to solve the MPIE based on Formulation C of Chapter 4. For surfaces of arbitrary shape, the triangle-patch model [5] is employed, while thin-wire structures are modeled by straight tubular segments [7]. Formulation C is also specialized in Chapter 5 to the case of an open transmission line consisting of an infinite conductor of arbitrary cross-section partially embedded in a grounded dielectric slab. In the numerical procedure, the conductor is modeled by straight line segments [4]. In Chapter 6, the numerical procedures used to evaluate the Sommerfeld-type integrals are discussed. In Chapter 7, sample numerical results are presented for several cases of interest involving PEC plates, cylinders, thin-wire antennas, and open microstrip lines. Where possible, comparisons are made with measured data or with computed results obtained by other researchers. Finally, in Chapter 8, we draw conclusions and make recommendations for future work.

CHAPTER 2

PRELIMINARIES

2.1. Statement of the Problem

Consider a medium consisting of $n + 1$ dielectric layers separated by n planar interfaces parallel to the xy plane of a Cartesian coordinate system and located at $z = z_l$, $l = 1, 2, \dots, n$, as illustrated in Fig. 2.1. The medium of the i th layer is characterized by permeability μ_i and permittivity ϵ_i , which may be complex if the medium is lossy. Let the PEC object (or collection of objects) in Fig. 2.1 occupy p layers with indices l_1, l_2, \dots, l_p , where $1 \leq p \leq n + 1$. For later convenience, define the ordered set of indices $L = \{l_1, l_2, \dots, l_p\}$, in which $l_k < l_{k+1}$. Let S_i denote the surface of the object(s) in the i th layer and let \hat{n}_i be a unit vector normal to S_i . The quantity of interest is the surface current density $\underline{J}(\underline{r})$ excited on the object(s) by a given time-harmonic incident electric field \underline{E}^{inc} . The $e^{j\omega t}$ time variation is assumed and suppressed.

2.2. Electric Field Integral Equation (EFIE)

The EFIE for the current density \underline{J} on the surface S of the PEC object(s) embedded in a layered medium is obtained by enforcing the boundary condition [31]

$$-\hat{n}_m \times \underline{E}_m^s(\underline{r}) = \hat{n}_m \times \underline{E}_m^{inc}(\underline{r}), \quad \underline{r} \text{ on } S_m, \quad m \in L \quad (2-1)$$

where \underline{r} is the position vector defined with respect to a global coordinate origin, \underline{E}_m^{inc} is the “incident” electric field (*i.e.*, the field in the absence of the object) in

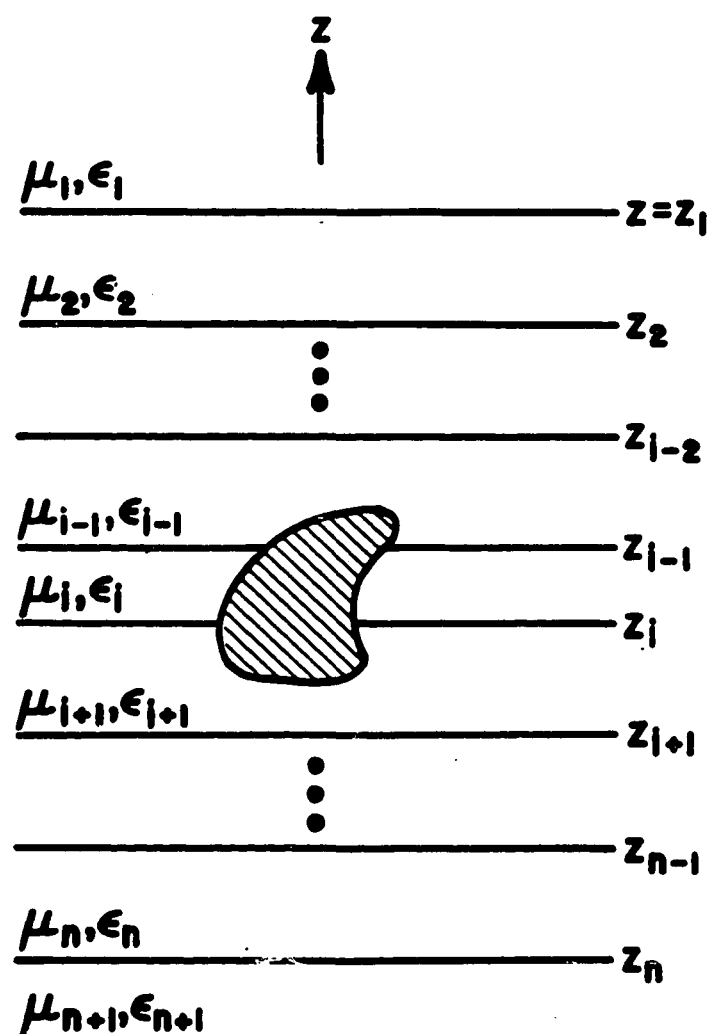


Fig. 2.1. Scatterer of arbitrary shape embedded in a layered dielectric medium.

the m th layer, and \underline{E}_m^s is the scattered field in the m th layer. For the structure of Fig. 2.1, \underline{E}_m^s and the scattered magnetic field \underline{H}_m^s can be expressed as

$$-\underline{E}_m^s(\underline{r}) = \sum_{i \in L} [j\omega \underline{A}^{mi}(\underline{r}) + \nabla \phi^{mi}(\underline{r})] \quad (2-2)$$

$$\underline{H}_m^s(\underline{r}) = \frac{1}{\mu_m} \nabla \times \sum_{i \in L} \underline{A}^{mi}(\underline{r}) \quad (2-3)$$

where \underline{A}^{mi} is the magnetic vector potential in the m th layer due to the current density \underline{J} in the i th layer, and is given as

$$\underline{A}^{mi}(\underline{r}) = \int_{S_i} \underline{\underline{G}}_A^{mi}(\underline{r} | \underline{r}') \cdot \underline{J}(\underline{r}') dS' \quad (2-4)$$

and $\phi^{mi}(\underline{r})$ is the corresponding scalar potential which is related to $\underline{A}^{mi}(\underline{r})$ through the Lorentz condition

$$\phi^{mi}(\underline{r}) = \frac{j\omega}{k_m^2} \nabla \cdot \underline{A}^{mi}(\underline{r}) \quad (2-5)$$

where $k_m^2 = \omega^2 \epsilon_m \mu_m$. In (2-4), $\underline{\underline{G}}_A^{mi}$ is the dyadic Green's function which represents the magnetic vector potential in region m due to a unit-strength, arbitrarily oriented current dipole in region i . $\underline{\underline{G}}_A^{mi}$ can be found by solving the inhomogeneous Helmholtz equation

$$(\nabla^2 + k_m^2) \underline{\underline{G}}_A^{mi}(\underline{r} | \underline{r}') = -\mu_m \underline{\underline{I}} \delta(\underline{r} - \underline{r}') \quad (2-6)$$

where $\underline{\underline{I}}$ is the idemfactor, subject to the condition that the tangential component of \underline{E}_m^s and \underline{H}_m^s be continuous across the interfaces between dielectric layers. As is well known [16], for a horizontal, say, x -directed dipole, two components of the vector potential are required to satisfy the boundary conditions at the interfaces. Tradi-

tionally [32], the z component has been selected in addition to the x component. The Green's function in this case takes the form [24]

$$\underline{\underline{G}}_A^{mi} = (\hat{x}\hat{x} + \hat{y}\hat{y}) G_{xx}^{mi} + \hat{z}\hat{x} G_{zx}^{mi} + \hat{z}\hat{y} G_{zy}^{mi} + \hat{z}\hat{z} G_{zz}^{mi}. \quad (2-7)$$

However, one may as well postulate the y component of the vector potential to accompany the primary x component [14]. This strategy leads to an alternative form of the Green's function,

$$\underline{\underline{G}}_A^{mi} = \hat{x}\hat{x} G_{xx}^{mi} + \hat{y}\hat{y} G_{yy}^{mi} + (\hat{x}\hat{y} + \hat{y}\hat{x}) G_{xy}^{mi} + \hat{z}\hat{z} G_{zz}^{mi}. \quad (2-8)$$

In (2-7) and (2-8) G_{xx}^{mi} denotes the x -component of $\underline{\underline{A}}^{mi}$ due to an x -directed, unit-strength electric dipole, G_{xy}^{mi} the x -component of $\underline{\underline{A}}^{mi}$ due to a similar, y -directed dipole, etc. We note that, except for G_{zz}^{mi} , the corresponding components in (2-7) and (2-8) are different, even though the same notation is used. The entries of the dyadics in (2-7) and (2-8) are developed in the next chapter, and are shown to comprise improper integrals of the Sommerfeld [16] type.

Still other Green's functions, in addition to those in (2-7) and (2-8) are possible. For example, one can obtain another form of $\underline{\underline{G}}_A^{mi}$ by postulating that the y and z components of the vector potential, instead of the x and z or x and y components, accompany an x -directed dipole. However, this and other forms of $\underline{\underline{G}}_A^{mi}$ are less attractive for our purpose than (2-7) and (2-8), and are not considered here.

Substitution of (2-2) into (2-1) yields

$$\hat{n}_m \times \sum_{i \in L} [j\omega \underline{\underline{A}}^{mi}(\underline{r}) + \nabla \phi^{mi}(\underline{r})] = \hat{n}_m \times \underline{\underline{E}}_m^{inc}(\underline{r}), \quad \underline{r} \text{ on } S_m, \quad m \in L \quad (2-9)$$

which, by invoking (2-4) and (2-5), can be further transformed to

$$\frac{j\omega}{k_m^2} \hat{\underline{n}}_m \times (\nabla \cdot + k_m^2) \sum_{i \in L} \int_{S_i} \underline{G}_A^{mi}(\underline{r} | \underline{r}') \cdot \underline{J}(\underline{r}') dS' = \hat{\underline{n}}_m \times \underline{E}_m^{inc}(\underline{r}), \quad \underline{r} \text{ on } S_m, \quad m \in L. \quad (2-10)$$

This equation is referred to as vector-potential EFIE [33], since it only involves the magnetic vector potential. Although (2-10) has often been used in MOM analyses of straight wire antennas or planar scatterers, the presence of the mixed tangential derivatives makes it less suitable for objects of arbitrary shape. By introducing the differential operator under the integral sign in (2-10), we may obtain another form of the EFIE, in which the dyadic kernel is the Green's function for the electric field. However, this EFIE is not attractive because the kernel is highly singular, which makes the evaluation of the integrals required by the MOM procedure difficult when the observation point is within the integration interval [34]. Also, the required differentiation of the Sommerfeld-type integrals adversely affects their convergence. These difficulties can be avoided if only one of the operators nabla is introduced inside the integral in (2-10) and then transferred, by a series of transformations, to act on the current. The result is the mixed-potential EFIE discussed below.

2.3. Mixed-Potential EFIE (MPIE)

We note that (2-9) would be in the desired mixed-potential form if the scalar potential were expressed in terms of the surface charge density $q(\underline{r})$. With this goal in mind, we substitute (2-4) into (2-5) and introduce the operator nabla under the integral sign (this step can be justified [35,36]) to obtain

$$\phi^{mi}(\underline{r}) = \frac{j\omega}{k_m^2} \int_{S_i} [\nabla \cdot \underline{G}_A^{mi}(\underline{r} | \underline{r}')] \cdot \underline{J}(\underline{r}') dS'. \quad (2-11)$$

Obviously, our objective would be achieved if we transferred the divergence operator to act on the current, in view of the equation of continuity, $\nabla \cdot \underline{J} = -j\omega q$. It is shown below that this can only be accomplished if a scalar function G_ϕ^{mi} can be found, such that

$$\frac{j\omega}{k_m^2} \nabla \cdot \underline{\underline{G}}_A^{mi}(\underline{r} | \underline{r}') = \frac{1}{j\omega} \nabla' G_\phi^{mi}(\underline{r} | \underline{r}'). \quad (2-12)$$

In a homogeneous medium, where G_ϕ^{mi} may be interpreted as the Green's function for the scalar potential, this is a quite trivial task. If the medium is stratified, however, G_ϕ^{mi} satisfying (2-12) does not in general exist [24], which can be attributed to the fact that the scalar potentials of point charges associated with horizontal and vertical current dipoles in a layered medium are in general different [15]. Hence, in order to achieve our goal, we follow the procedure proposed in [23,24], and introduce a scalar function K_ϕ^{mi} and a vector function \underline{P}^{mi} according to

$$\frac{j\omega}{k_m^2} \nabla \cdot \underline{\underline{G}}_A^{mi}(\underline{r} | \underline{r}') = \frac{1}{j\omega} \nabla' K_\phi^{mi}(\underline{r} | \underline{r}') + j\omega \underline{P}^{mi}(\underline{r} | \underline{r}'). \quad (2-13)$$

One should note that in the above the choice of K_ϕ^{mi} and \underline{P}^{mi} is not unique.

Upon substituting (2-13) into (2-11) and using a vector identity (p. 487, [37]) and the Gauss theorem (p. 503, [37]), we can express the scalar potential as

$$\begin{aligned} \phi^{mi}(\underline{r}) &= \int_{S_i} K_\phi^{mi}(\underline{r} | \underline{r}') q(\underline{r}') dS' + j\omega \int_{S_i} \underline{P}^{mi}(\underline{r} | \underline{r}') \cdot \underline{J}(\underline{r}') dS' \\ &\quad + \frac{1}{j\omega} \left[\oint_{C_i} K_\phi^{mi}(\underline{r} | \underline{r}') \underline{J}(\underline{r}') \cdot \hat{\underline{u}}_i dC' - \oint_{C_{i-1}} K_\phi^{mi}(\underline{r} | \underline{r}') \underline{J}(\underline{r}') \cdot \hat{\underline{u}}_{i-1} dC' \right] \end{aligned} \quad (2-14)$$

where C_i and C_{i-1} are the contours formed by the intersection of the surface S_i

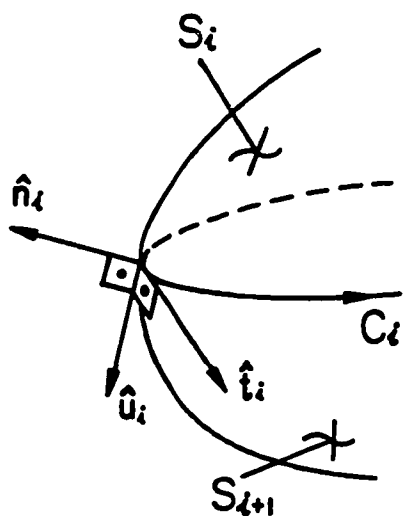
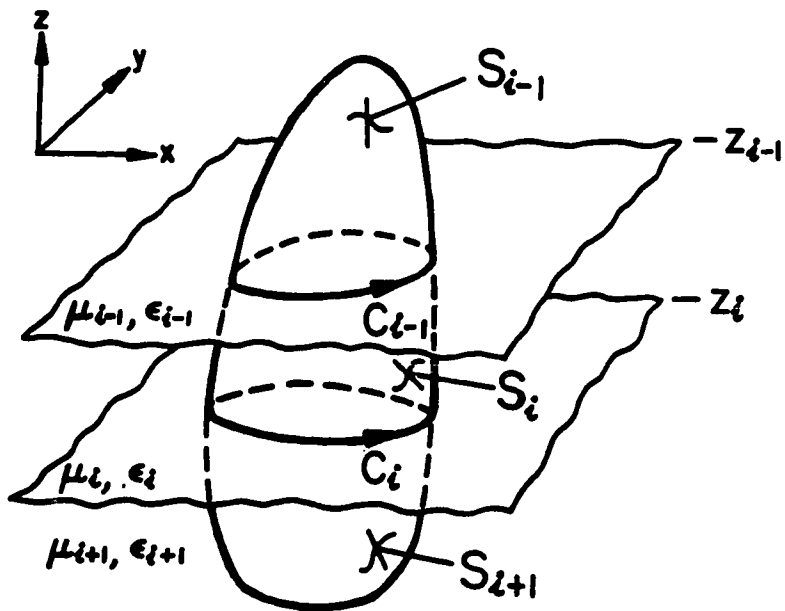
with the interfaces at $z = z_i$ and $z = z_{i-1}$, respectively, and \hat{u}_i and \hat{u}_{i-1} are the unit vectors perpendicular at \underline{r}' to C_i and C_{i-1} , respectively, in the planes tangent to S_i (Fig. 2.2). Substituting (2-14) into (2-9), we finally obtain

$$\begin{aligned} \hat{n}_m \times \sum_{i \in L} \left\{ j\omega \int_{S_i} \underline{\underline{K}}_A^{mi}(\underline{r} | \underline{r}') \cdot \underline{J}(\underline{r}') dS' + \nabla \int_{S_i} K_\phi^{mi}(\underline{r} | \underline{r}') q(\underline{r}') dS' \right. \\ \left. + \frac{\nabla}{j\omega} \left[\oint_{C_i} K_\phi^{mi}(\underline{r} | \underline{r}') J(\underline{r}') \cdot \hat{u}_i dC' - \oint_{C_{i-1}} K_\phi^{mi}(\underline{r} | \underline{r}') J(\underline{r}') \cdot \hat{u}_{i-1} dC' \right] \right\} \\ = \hat{n}_m \times \underline{E}_m^{inc}(\underline{r}), \quad \underline{r} \text{ on } S_m, \quad m \in L \end{aligned} \quad (2-15)$$

where we have introduced the dyadic kernel

$$\underline{\underline{K}}_A^{mi}(\underline{r} | \underline{r}') = \underline{\underline{G}}_A^{mi}(\underline{r} | \underline{r}') + \nabla \underline{P}^{mi}(\underline{r} | \underline{r}'). \quad (2-16)$$

We note that (2-15) would be in the desired mixed-potential form [4,5] if it were not for the presence of the term contributed by the contour integrals, which occur when the object penetrates one or more of the interfaces. In Chapter 4 we show that with a proper choice of $\underline{\underline{G}}_A^{mi}$ and K_ϕ^{mi} in (2-13) the contour integrals cancel out. We note, however, that even if a formulation is chosen in which the contour integrals persist, the MOM procedures developed in [4,5] can be extended to accommodate these terms. As a matter of fact, the “correction term” $\nabla \underline{P}^{mi}$ could also be handled in this manner, instead of being incorporated into the vector potential kernel via (2-16).



$$\hat{u}_i = \hat{t}_i \times \hat{n}_i$$

Fig. 2.2. (a) Arbitrarily shaped surface penetrating two adjacent interfaces. (b) Detail of contour C_i with unit vectors \hat{u}_i , \hat{t}_i and \hat{n}_i .

CHAPTER 3
DERIVATION OF GREEN'S FUNCTIONS
FOR THE MAGNETIC VECTOR POTENTIAL

The dyadic Green's function $\underline{\underline{G}}_A^{mi}(\underline{r}|\underline{r}')$ in (2-4) in region m is the vector potential due to a unit-strength, arbitrarily-oriented Hertzian dipole in the i th layer. The direct solution of (2-6) for $\underline{\underline{G}}_A^{mi}$ is extremely tedious, since various components of this dyadic couple in the boundary conditions at the interfaces between dielectric layers. Therefore, in this chapter, we derive the Green's function by means of a Fourier transformation, which in effect reduces the original problem to that of solving an equivalent transmission-line network along the z coordinate.

3.1. Reduction of Maxwell's Equations to Transmission-line Equations for Sources in Layered Media

For the geometry of Fig. 3.1a, we are interested in the electromagnetic field ($\underline{E}, \underline{H}$) everywhere in the medium due to prescribed distributions of time-harmonic electric and magnetic currents \underline{J} and \underline{M} , respectively. Since the structure is infinite along the x and y coordinates, we can simplify the analysis by utilizing the "shifted" Fourier transform pair

$$\tilde{\mathcal{F}}\{f(x-x', y-y')\} = \tilde{f}(k_x, k_y) = \int_{-\infty}^{\infty} \int_{-\infty}^{\infty} f(x-x', y-y') e^{j[k_x(x-x')+k_y(y-y')]} dx dy \quad (3-1)$$

$$\tilde{\mathcal{F}}^{-1}\{\tilde{f}(k_x, k_y)\} = f(x-x', y-y') = \frac{1}{(2\pi)^2} \int_{-\infty}^{\infty} \int_{-\infty}^{\infty} \tilde{f}(k_x, k_y) e^{-j[k_x(x-x')+k_y(y-y')]} dk_x dk_y \quad (3-2)$$

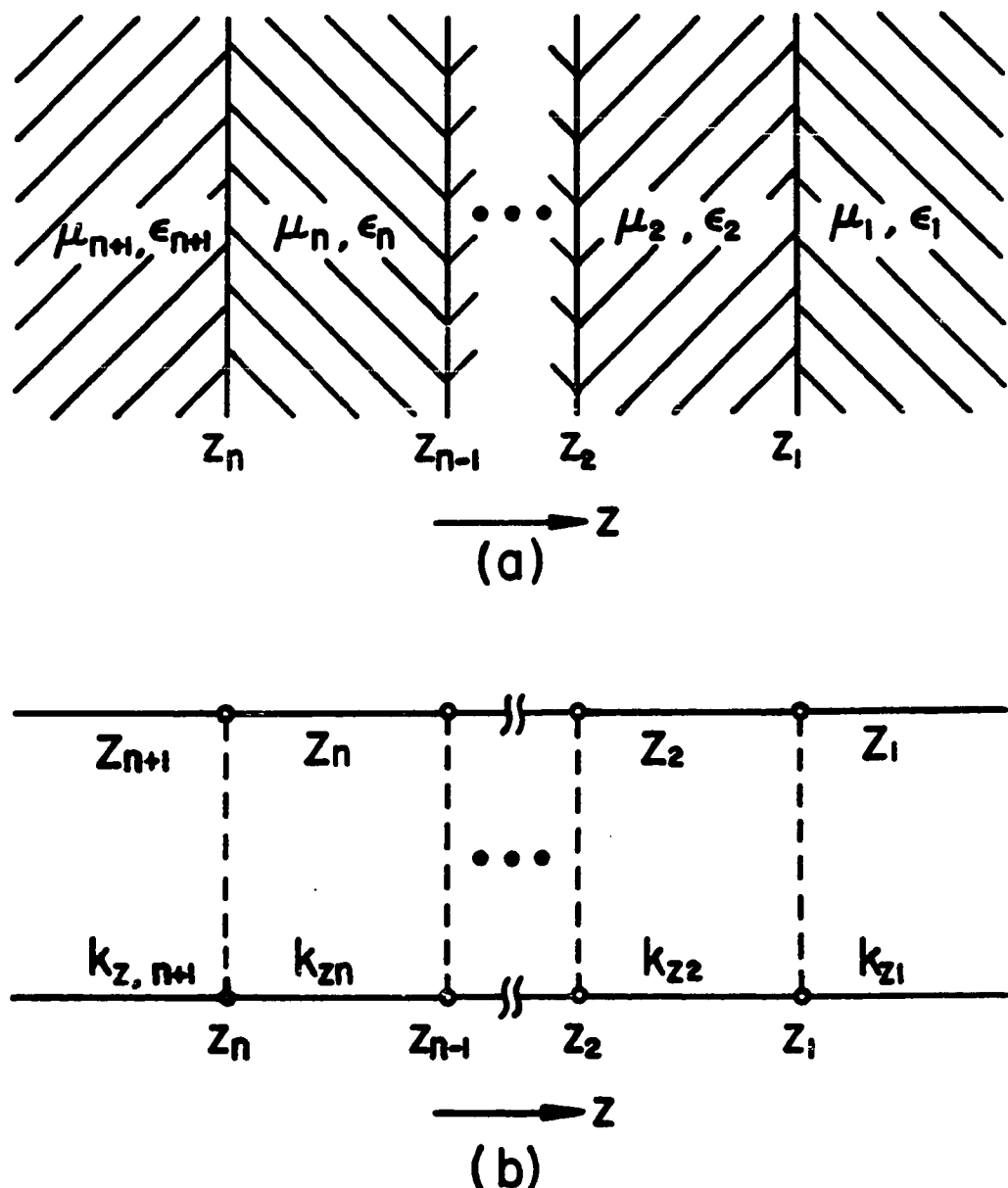


Fig. 3.1. (a) Plane-stratified dielectric medium and (b) its transmission-line network representation.

where (x', y') locates the projection of the source point on the xy -plane (Fig. 3.2).

The inverse Fourier integrals (3-2) can be conveniently expressed in terms of the Sommerfeld-type integrals [16] of the form

$$S_n [\tilde{f}(k_\rho)] = \int_0^\infty \tilde{f}(k_\rho) J_n(k_\rho \xi) k_\rho^{n+1} dk_\rho \quad (3-3)$$

by changing to polar coordinates in both the transform and space domains according to

$$x - x' = \xi \cos \zeta, \quad y - y' = \xi \sin \zeta \quad (3-4)$$

$$k_x = k_\rho \cos \alpha, \quad k_y = k_\rho \sin \alpha \quad (3-5)$$

where (Fig. 3.2)

$$\xi = \sqrt{(x - x')^2 + (y - y')^2}, \quad \zeta = \arctan \left(\frac{y - y'}{x - x'} \right) \quad (3-6)$$

$$k_\rho = \sqrt{k_x^2 + k_y^2}, \quad \alpha = \arctan \left(\frac{k_y}{k_x} \right) \quad (3-7)$$

and where J_n is the Bessel function of order n . Hence, using (3-3), we express (3-2) as

$$\mathfrak{F}^{-1} \{ \tilde{f}(k_\rho) \} = \frac{1}{2\pi} S_0 [\tilde{f}(k_\rho)]. \quad (3-8)$$

We also have

$$\mathfrak{F}^{-1} \{ j k_x \tilde{f}(k_\rho) \} = \frac{\cos \zeta}{2\pi} S_1 [\tilde{f}(k_\rho)] \quad (3-9)$$

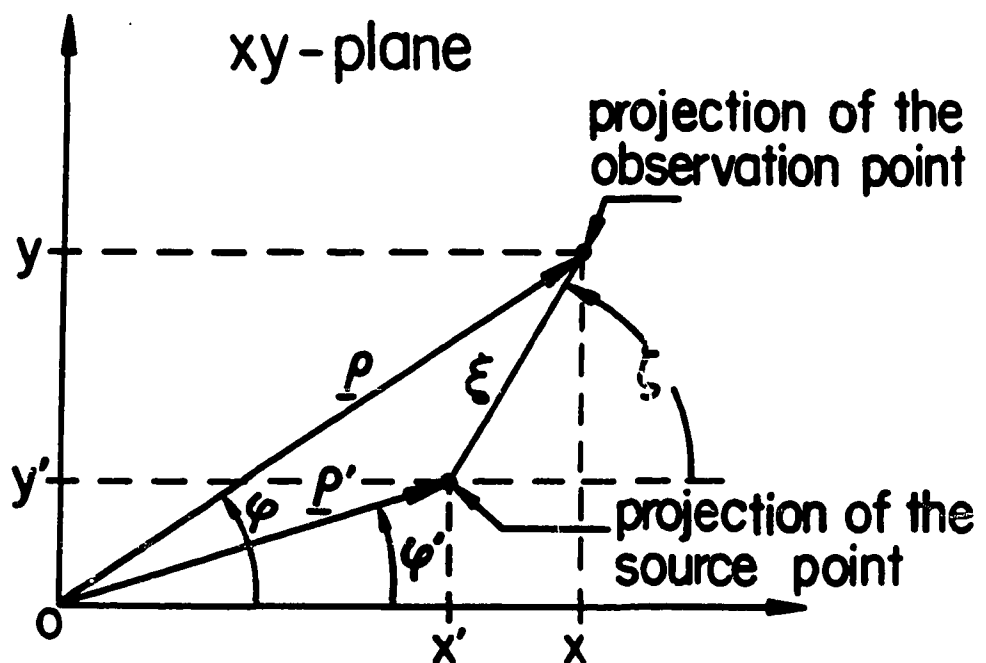


Fig. 3.2. Definition of the distance ξ and angle ζ .

$$\mathfrak{F}^{-1}\{jk_y\tilde{f}(k_\rho)\} = \frac{\sin\zeta}{2\pi} S_1[\tilde{f}(k_\rho)] \quad (3-10)$$

$$\mathfrak{F}^{-1}\{k_x^2\tilde{f}(k_\rho)\} = -\frac{1}{4\pi} \left\{ \cos 2\zeta S_2[\tilde{f}(k_\rho)] - S_0[k_\rho^2 \tilde{f}(k_\rho)] \right\} \quad (3-11)$$

$$\mathfrak{F}^{-1}\{k_y^2\tilde{f}(k_\rho)\} = \frac{1}{4\pi} \left\{ \cos 2\zeta S_2[\tilde{f}(k_\rho)] + S_0[k_\rho^2 \tilde{f}(k_\rho)] \right\} \quad (3-12)$$

$$\mathfrak{F}^{-1}\{k_x k_y \tilde{g}(k_\rho)\} = -\frac{1}{4\pi} \sin 2\zeta S_2[\tilde{g}(k_\rho)]. \quad (3-13)$$

These relationships will be used in the formulation of vector potential Green's functions. We list them here for later convenience.

Since the structure of Fig. 3.1a can be regarded as a uniform cylindrical waveguide (of infinite cross-section) with z as the longitudinal (axial) coordinate, it is fruitful to decompose the field and source vectors into their transverse and longitudinal parts: $\underline{E} = \underline{E}_t + \hat{z}E_z$, $\underline{H} = \underline{H}_t + \hat{z}H_z$, etc. The solution of the field equations for \underline{E} and \underline{H} is facilitated by eliminating the dependent longitudinal components from the Maxwell's equations [38,39]. Hence, by eliminating E_z and H_z and invoking the Fourier transform (3-1), we arrive at

$$-\frac{d}{dz}\tilde{\underline{E}}_t = j\omega\mu \left(\underline{\underline{I}} + \frac{\widetilde{\nabla}_t \widetilde{\nabla}_t}{k^2} \right) \cdot (\widetilde{\underline{H}}_t \times \hat{z}) + \widetilde{\underline{M}}_{te} \times \hat{z} \quad (3-14)$$

$$-\frac{d}{dz}\widetilde{\underline{H}}_t = j\omega\epsilon \left(\underline{\underline{I}} + \frac{\widetilde{\nabla}_t \widetilde{\nabla}_t}{k^2} \right) \cdot (\hat{z} \times \tilde{\underline{E}}_t) + \hat{z} \times \tilde{\underline{J}}_{te} \quad (3-15)$$

where the equivalent transverse electric and magnetic current distributions are

given, respectively, as

$$\underline{\tilde{J}}_{te} = \underline{\tilde{J}}_t - \hat{z} \times \frac{\widetilde{\nabla}_t \widetilde{M}_z}{j\omega\mu} \quad (3-16)$$

and

$$\underline{\widetilde{M}}_{te} = \underline{\widetilde{M}}_t + \hat{z} \times \frac{\widetilde{\nabla}_t \widetilde{J}_z}{j\omega\epsilon}, \quad (3-17)$$

\underline{I} is a unit dyadic, and $\widetilde{\nabla}_t = -jk_x \hat{x} - jk_y \hat{y}$ is the transform domain counterpart of the transverse operator nabla. The longitudinal field components are derivable from the transverse components as [39]

$$\underline{\tilde{E}}_z = \frac{1}{j\omega\epsilon} \left\{ \widetilde{\nabla}_t \cdot (\underline{\widetilde{H}}_t \times \hat{z}) - \underline{\tilde{J}}_z \right\} \quad (3-18)$$

$$\underline{\widetilde{H}}_z = \frac{1}{j\omega\mu} \left\{ \widetilde{\nabla}_t \cdot (\hat{z} \times \underline{\tilde{E}}_t) - \underline{\widetilde{M}}_z \right\}. \quad (3-19)$$

Equations (3-14)–(3-19) hold for each layer of the stratified medium (Fig. 3.1a). The layer subscript has been suppressed in these equations for simplicity.

Since any vector can be represented as a sum of two parts, one of which is solenoidal and the other irrotational, we may express the vectors $\underline{\tilde{E}}_t$ and $\underline{\widetilde{H}}_t \times \hat{z}$ as [39]

$$\underline{\tilde{E}}_t = -\widetilde{\nabla}_t V^e - \widetilde{\nabla}_t V^h \times \hat{z} \quad (3-20)$$

$$\underline{\widetilde{H}}_t \times \hat{z} = -\widetilde{\nabla}_t I^e - \widetilde{\nabla}_t I^h \times \hat{z}. \quad (3-21)$$

Using these equations in (3-18) and (3-19), we can express the longitudinal field

components as

$$\tilde{E}_z = \frac{1}{j\omega\epsilon} (k_\rho^2 I^e - \tilde{J}_z) \quad (3-22)$$

$$\tilde{H}_z = \frac{1}{j\omega\mu} (k_\rho^2 V^h - \tilde{M}_z) \quad (3-23)$$

where $k_\rho^2 = k_x^2 + k_y^2$. Equations (3-20)–(3-23) indicate that in source-free regions V^e , I^e , and V^h , I^h generate, respectively, field transverse magnetic (TM) and transverse electric (TE) to z .

To determine the scalar functions V^e , I^e , V^h , and I^h , we use (3-20) and (3-21) to eliminate \tilde{E}_t and \tilde{H}_t from (3-14) and (3-15). As a result, we obtain the equations [39]

$$-\frac{dV^q}{dz} = jk_z Z^q I^q + v^q \quad (3-24)$$

$$-\frac{dI^q}{dz} = jk_z Y^q V^q + i^q \quad (3-25)$$

where the superscript “ q ” stands for either “ e ” or “ h ” and where $k_z^2 = k^2 - k_\rho^2$. The modal impedances Z^q (admittances Y^q) are defined as

$$Z^e = \frac{1}{Y^e} = \frac{k_z}{\omega\epsilon} \quad (3-26)$$

$$Z^h = \frac{1}{Y^h} = \frac{\omega\mu}{k_z} \quad (3-27)$$

and the source functions v^q and i^q are given by

$$v^e = -\frac{\tilde{J}_z}{j\omega\epsilon} + \frac{1}{k_\rho^2} (\hat{z} \times \tilde{\nabla}_t) \cdot \tilde{M}_t \quad (3-28)$$

$$i^e = \frac{1}{k_p^2} \tilde{\nabla}_t \cdot \tilde{J}_t \quad (3-29)$$

$$v^h = \frac{1}{k_p^2} \tilde{\nabla}_t \cdot \tilde{M}_t \quad (3-30)$$

$$i^h = -\frac{\tilde{M}_z}{j\omega\mu} - \frac{1}{k_p^2} (\hat{z} \times \tilde{\nabla}_t) \cdot \tilde{J}_t. \quad (3-31)$$

Equations (3-24) and (3-25) have the form of transmission-line equations for the voltage V^q and current I^q . To the l th layer of the stratified medium (Fig. 3.1a) there corresponds a transmission line section with characteristic impedance Z_l^q and propagation constant k_{z_l} . Hence, the layered medium of Fig. 3.1a may be represented by two transmission-line networks, which may be referred to as the TM and TE networks, each of the form shown in Fig. 3.1b. The TM network has characteristic impedances Z_l^e and sources v^e and i^e ; the TE network has characteristic impedances Z_l^h and is driven by v^h and i^h . Depending on the sources (cf. (3-28)—(3-31)), the TM, the TE or both networks may be excited. These network problems must be solved subject to the condition that the voltages and currents be continuous across the interfaces between contiguous line sections. These conditions are the consequence of the continuity of the transverse components of the electric and magnetic fields across the interfaces between adjacent dielectric layers (Fig. 3.1a).

The solution of the transmission-line equations (3-24) and (3-25) is facilitated if one appeals to the principle of superposition and considers the effect of the voltage and current sources separately. Hence, with only voltage sources present ($i^q = 0$),

(3-24) and (3-25) reduce to

$$\left(\frac{d}{dz^2} + k_z^2 \right) I^q = jk_z Y^q v^q \quad (3-32)$$

$$V^q = -\frac{Z^q}{jk_z} \frac{d}{dz} I^q. \quad (3-33)$$

From these equations, the impedances seen looking to the left and to the right at a point z on the transmission line can be expressed, respectively, as

$$\overleftarrow{Z}^q(z) = -\frac{V^q(z)}{I^q(z)} = \frac{Z^q}{jk_z} \frac{d}{dz} \ln I^q(z) \quad (3-34)$$

and

$$\overrightarrow{Z}^q(z) = \frac{V^q(z)}{I^q(z)} = -\frac{Z^q}{jk_z} \frac{d}{dz} \ln I^q(z). \quad (3-35)$$

Similarly, with only current sources present ($v^q = 0$), (3-24) and (3-25) reduce to

$$\left(\frac{d}{dz^2} + k_z^2 \right) V^q = jk_z Z^q i^q \quad (3-36)$$

$$I^q = -\frac{Y^q}{jk_z} \frac{d}{dz} V^q. \quad (3-37)$$

The admittances seen looking to the left and to the right at a point z on the transmission line can be in this case expressed, respectively, as

$$\overleftarrow{Y}^q(z) = -\frac{I^q(z)}{V^q(z)} = \frac{Y^q}{jk_z} \frac{d}{dz} \ln V^q(z) \quad (3-38)$$

and

$$\vec{Y}^q(z) = \frac{\vec{I}^q(z)}{\vec{V}^q(z)} = -\frac{Y^q}{jk_z} \frac{d}{dz} \ln V^q(z). \quad (3-39)$$

Once the transmission-line equations (3-32), (3-33), (3-36) and (3-37) are solved for V^e , I^e , and V^h , I^h , we determine \underline{E} and \underline{H} from (3-20)–(3-23). Finally, the inverse Fourier transform of (3-2) is employed to recover \underline{E} and \underline{H} . The solution of (3-32), (3-33), (3-36) and (3-37) for the stratified medium of Fig. 3.1a is discussed in the next section.

3.2. Solution of Transmission-Line Equations

It was shown in the last section that the layered medium of Fig. 3.1a can be represented by the transmission-line network of Fig. 3.1b. The voltage and the current in each transmission-line section are governed by (3-24) and (3-25), or equivalently, by (3-32), (3-33), (3-36), and (3-37). In solving these equations, it is helpful to define for each interface the impedances and voltage reflection coefficients, as illustrated in Fig. 3.3. (For notational simplicity, we suppress the superscripts “ q ”.) The solution of (3-32), (3-33), (3-36), and (3-37) is simplified by first considering point-source excitations and then obtaining the total response by use of the superposition theorem [39]. Without loss of generality, we assume that the sources are located in the i th section of the transmission line (which corresponds to the i th layer in Fig. 3.1a) and that the impedances $\overleftarrow{Z}_i(z_i) \equiv \overleftarrow{Z}_i$ and $\overrightarrow{Z}_i(z_{i-1}) \equiv \overrightarrow{Z}_{i-1}$ (or their inverses \overleftarrow{Y}_i and \overrightarrow{Y}_{i-1}) are specified. Hence, if we denote the current I in the i th line section due to a point voltage $v = -\delta(z - z')$ in the same section as \tilde{G}_{ii}^I , we

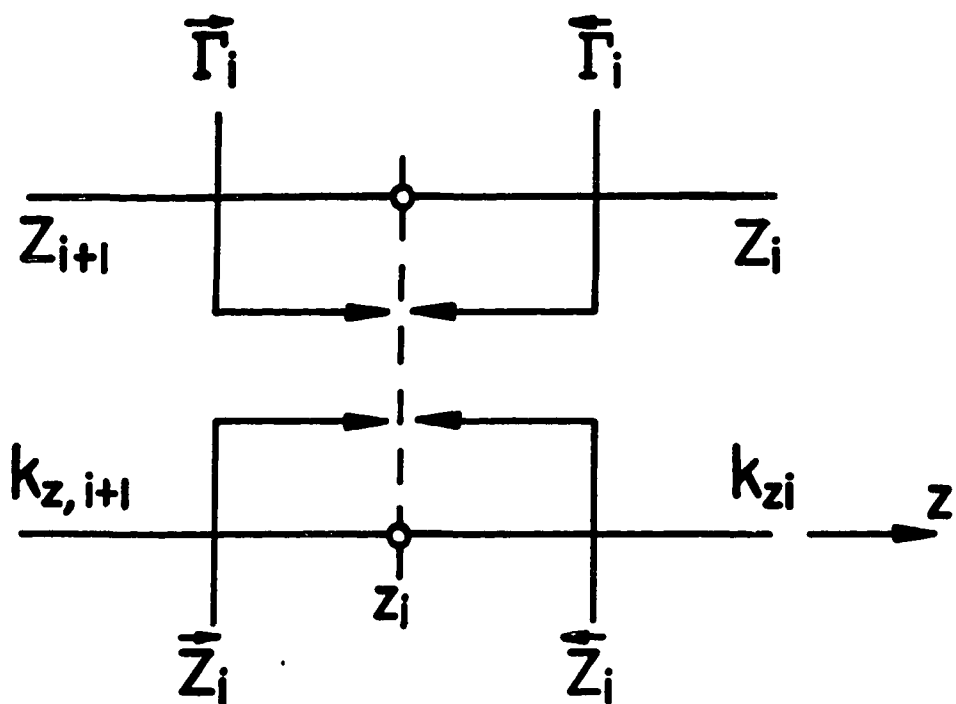


Fig. 3.3. Reflection coefficients and impedances associated with the i th interface.

obtain from (3-32)

$$\left(\frac{d^2}{dz^2} + k_{zi}^2 \right) \tilde{G}_{ii}^I(z, z') = -jk_{zi}Y_i\delta(z - z'). \quad (3-40)$$

This equation must be solved subject to the boundary conditions (cf. (3-34) and (3-35))

$$\overleftarrow{Z}_i = \frac{Z_i}{jk_{zi}} \frac{d}{dz} \ln \tilde{G}_{ii}^I(z, z'), \quad z = z_i \quad (3-41)$$

$$\overrightarrow{Z}_{i-1} = -\frac{Z_i}{jk_{zi}} \frac{d}{dz} \ln \tilde{G}_{ii}^I(z, z'), \quad z = z_{i-1}. \quad (3-42)$$

Equations (3-40)–(3-42) can be represented by the network shown in Fig. 3.4a.

In a like manner, if we denote the voltage V in the i th line section due to the point current $i = -\delta(z - z')$ in the same section as \tilde{G}_{ii}^V , we obtain from (3-36)

$$\left(\frac{d^2}{dz^2} + k_{zi}^2 \right) \tilde{G}_{ii}^V(z, z') = -jk_{zi}Z_i\delta(z - z'). \quad (3-43)$$

The boundary conditions in this case are (cf. (3-38) and (3-39))

$$\overleftarrow{Y}_i = \frac{Y_i}{jk_{zi}} \frac{d}{dz} \ln \tilde{G}_{ii}^I(z, z'), \quad z = z_i \quad (3-44)$$

$$\overrightarrow{Y}_{i-1} = -\frac{Y_i}{jk_{zi}} \frac{d}{dz} \ln \tilde{G}_{ii}^I(z, z'), \quad z = z_{i-1}. \quad (3-45)$$

Equations (3-43)–(3-45) have the network representation shown in Fig. 3.4b.

We first turn attention to (3-43); the solution of (3-40) will follow by duality. Hence, solving (3-43) subject to the boundary conditions in (3-44) and (3-45), we

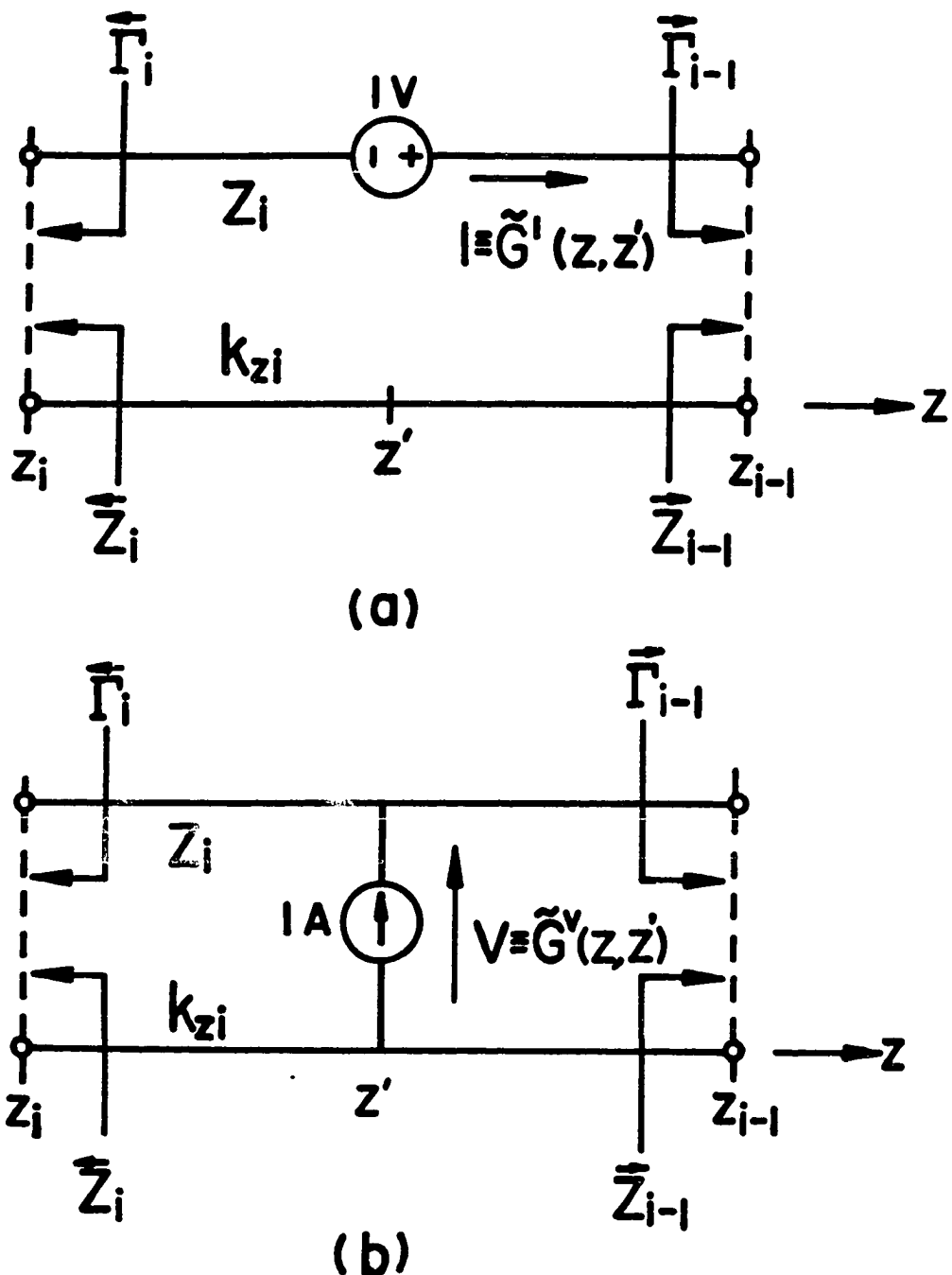


Fig. 3.4. (a) Voltage source and (b) current source in the i th transmission-line section.

obtain

$$\tilde{G}_{ii}^V(z, z') = \frac{Z_i}{2} \left(e^{-jk_{zi}|z-z'|} + \tilde{Q}_i^V(z, z') \right) \quad (3-46)$$

with

$$\begin{aligned} \tilde{Q}_i^V(z, z') = \frac{1}{D_i} & \left(\overleftarrow{\Gamma}_i e^{-jk_{zi}[(z+z')-2z_i]} + \overrightarrow{\Gamma}_{i-1} e^{-jk_{zi}[2z_{i-1}-(z+z')]} \right. \\ & \left. + 2\overleftarrow{\Gamma}_i \overrightarrow{\Gamma}_{i-1} e^{-j2\psi_i} \cos[k_{zi}(z-z')] \right) \end{aligned} \quad (3-47)$$

$$D_i = 1 - \overleftarrow{\Gamma}_i \overrightarrow{\Gamma}_{i-1} e^{-j2\psi_i} \quad (3-48)$$

where $\psi_i = k_{zi}d_i$, $d_i = z_{i-1} - z_i$. The reflection coefficients $\overrightarrow{\Gamma}_k$ and $\overleftarrow{\Gamma}_k$ (see Fig. 3.3) are given by, respectively,

$$\overrightarrow{\Gamma}_k = \frac{\overrightarrow{Z}_k - Z_{k+1}}{\overrightarrow{Z}_k + Z_{k+1}}, \quad k = 1, 2, \dots, n \quad (3-49)$$

and

$$\overleftarrow{\Gamma}_k = \frac{\overleftarrow{Z}_k - Z_k}{\overleftarrow{Z}_k + Z_k}, \quad k = 1, 2, \dots, n \quad (3-50)$$

where $\overrightarrow{\Gamma}_0 \equiv 0 \equiv \overleftarrow{\Gamma}_{n+1}$.

The yet unspecified impedances \overrightarrow{Z}_k and \overleftarrow{Z}_k can be obtained from the analysis of the transmission-line network of Fig. 3.1b. It can be shown that these impedances are given by the recursion formulas

$$\overrightarrow{Z}_k = Z_k \frac{\overrightarrow{Z}_{k-1} + jZ_k t_k}{\overrightarrow{Z}_k + j\overrightarrow{Z}_{k-1} t_k}, \quad k = 2, 3, \dots, n \quad (3-51)$$

and

$$\overleftarrow{Z}_k = Z_{k+1} \frac{\overleftarrow{Z}_{k+1} + j Z_{k+1} t_{k+1}}{Z_{k+1} + j \overleftarrow{Z}_{k+1} t_{k+1}}, \quad k = n-1, n-2, \dots, 1 \quad (3-52)$$

where $\overrightarrow{Z}_1 \equiv Z_1$, $\overleftarrow{Z}_n \equiv Z_{n+1}$, and $t_k = \tan \psi_k$.

From (3-46), one can compute the voltage anywhere in the i th line section, including the terminals, due to a unit current source in the same section (cf. Fig. 3.4b). The voltage in any other, say m th, section due to this source can be easily determined from the analysis of the transmission-line network of Fig. 3.1b as

$$\tilde{G}_{mi}^V(z, z') = \begin{cases} \tilde{G}_{ii}^V(z_{i-1}, z') \overrightarrow{T}_{mi}^V(z), & i-1 \geq m \geq 1 \\ \tilde{G}_{ii}^V(z_i, z') \overleftarrow{T}_{mi}^V(z), & n+1 \geq m \geq i+1 \end{cases} \quad (3-53)$$

where the voltage transfer functions $\overrightarrow{T}_{mi}^V$ and \overleftarrow{T}_{mi}^V are given, respectively, as

$$\overrightarrow{T}_{mi}^V(z) = \frac{e^{-jk_{zm}(z-z_m)}}{1 + \overrightarrow{\Gamma}_{m-1} e^{-j2\psi_m}} \left\{ 1 + \overrightarrow{\Gamma}_{m-1} e^{-j2k_{zm}(z_{m-1}-z)} \right\} \cdot \prod_{k=m}^{i-2} \frac{\left(1 + \overrightarrow{\Gamma}_k \right) e^{-j\psi_{k+1}}}{1 + \overrightarrow{\Gamma}_k e^{-j2\psi_{k+1}}} \quad (3-54)$$

and

$$\overleftarrow{T}_{mi}^V(z) = \frac{e^{-jk_{zm}(z_{m-1}-z)}}{1 + \overleftarrow{\Gamma}_m e^{j2\psi_m}} \left\{ 1 + \overleftarrow{\Gamma}_m e^{-j2k_{zm}(z-z_m)} \right\} \cdot \prod_{k=i+1}^{m-1} \frac{\left(1 + \overleftarrow{\Gamma}_k \right) e^{-j\psi_k}}{1 + \overleftarrow{\Gamma}_k e^{-j2\psi_k}}. \quad (3-55)$$

This completes the solution of (3-43). Equation (3-40) can be solved by a dual procedure. However, this is not necessary: we can obtain \tilde{G}_{mi}^I from \tilde{G}_{mi}^V by replacing in the latter all impedances Z_i by their reciprocals Y_i . As a result of this operation, all reflection coefficients change signs, as is evident from (3-49)–(3-50).

\tilde{G}_{mi}^I and \tilde{G}_{mi}^V will be referred to, respectively, as the current and voltage

transmission-line Green's functions.

3.3. Derivation of the Dyadic Green's Functions for the Magnetic Vector Potential in a Plane-Stratified Medium

The magnetic vector potential $\underline{\underline{A}}^{mi}$ in the m th layer of the stratified medium (Fig. 3.1a) due to a current distribution \underline{J} occupying a volume V_i in the i th layer can be obtained from

$$\underline{\underline{A}}^{mi}(\underline{r}) = \int_{V_i} \underline{\underline{G}}_A^{mi}(\underline{r} | \underline{r}') \cdot \underline{J}(\underline{r}') dV' \quad (3-56)$$

where $\underline{\underline{G}}_A^{mi}$ is the dyadic Green's function for the magnetic vector potential, which can be expressed either in the traditional form (2-7), or the alternative form (2-8). To determine the elements of the dyadic in (3-56), we appeal to the transmission-line analogy and make use of the transmission-line Green's functions developed in Sections 3.1 and 3.2. Hence, from (3-29) and (3-31) we determine that an x -directed dipole with $\tilde{\underline{J}} \equiv \tilde{\underline{J}}_t = \hat{x}\delta(z - z')$ gives rise to transmission-line sources i^e and i^h given, respectively, as

$$i^e(z) = -\frac{jk_x}{k_\rho^2} \delta(z - z') \quad (3-57)$$

and

$$i^h(z) = -\frac{jk_y}{k_\rho^2} \delta(z - z') \quad (3-58)$$

where we assume that the sources are in the i th layer, i.e., $z_i < z' < z_{i-1}$. Obviously, both the TM and TE transmission-line networks are excited in this case. The current generators given by (3-57) and (3-58) excite, respectively, the voltages V_{mi}^e

and V_{mi}^h in the m th sections of the transmission-line network. From Section 3.2, we find

$$V_{mi}^e(z) = \frac{jk_x}{k_p^2} \tilde{G}_{mi}^{V_e}(z, z') \quad (3-59)$$

and

$$V_{mi}^h(z) = \frac{jk_y}{k_p^2} \tilde{G}_{mi}^{V_h}(z, z'). \quad (3-60)$$

For a y -directed dipole with $\tilde{\underline{J}} \equiv \tilde{\underline{J}}_t = \hat{y}\delta(z - z')$, (3-29) and (3-31) yield

$$i^e(z) = -\frac{jk_y}{k_p^2} \delta(z - z') \quad (3-61)$$

$$i^h(z) = +\frac{jk_x}{k_p^2} \delta(z - z'). \quad (3-62)$$

These sources excite the voltages (Section 3.2)

$$V_{mi}^e(z) = \frac{jk_y}{k_p^2} \tilde{G}_{mi}^{V_e}(z, z') \quad (3-63)$$

and

$$V_{mi}^h(z) = -\frac{jk_x}{k_p^2} \tilde{G}_{mi}^{V_h}(z, z') \quad (3-64)$$

respectively.

Finally, for a vertical dipole with $\tilde{\underline{J}} \equiv \hat{z}\tilde{\underline{J}}_z = \hat{z}\delta(z - z')$, we obtain from (3-28)

$$v^e(z) = -\frac{1}{j\omega\epsilon_i} \delta(z - z'). \quad (3-65)$$

Hence, only the TM transmission-line network is excited in this case. The current

I_{mi}^e in the m th section due to the voltage source give in (3-65) is easily found as (cf. Section 3.2)

$$I_{mi}^e(z) = \frac{1}{j\omega\epsilon_i} \tilde{G}_{mi}^{I_e}(z, z'). \quad (3-66)$$

We now must relate these transmission-line voltages and currents to the components of the magnetic vector potential. First, we turn our attention to a vertical dipole source, which gives rise to only the z -component of the vector potential. Outside the source ($z \neq z'$), the z -component of the electric field can be expressed in terms of \tilde{A}_z^{mi} as

$$\tilde{E}_z^{mi} = -\frac{j\omega}{k_m^2} \left(\frac{d^2}{dz^2} + k_m^2 \right) \tilde{A}_z^{mi} = -\frac{j\omega}{k_m^2} k_\rho^2 \tilde{A}_z^{mi}. \quad (3-67)$$

On the other hand, from (3-46) we have

$$\tilde{E}_z^{mi} = \frac{1}{j\omega\epsilon_m} k_\rho^2 I_m^e. \quad (3-68)$$

Eliminating \tilde{E}_z^{mi} between (3-67) and (3-68), we obtain

$$\tilde{A}_z^{mi} = \mu_m I_{mi}^e. \quad (3-69)$$

It can be shown that this solution holds in the source region ($z = z'$), too. If the current I_{mi}^e in (3-69) is that generated by a z -directed dipole, then $\tilde{A}_z^{mi} = \tilde{G}_{zz}^{mi}$. Hence, substituting from (3-66) into (3-69), we obtain

$$\tilde{G}_{zz}^{mi} = \frac{1}{j\omega} \frac{\mu_m}{\epsilon_i} \tilde{G}_{mi}^{I_e}. \quad (3-70)$$

The horizontal (x - or y - directed) dipole source may give rise to all components of

$\tilde{\underline{A}}^{mi}$, i.e., $\tilde{\underline{A}}^{mi} = \hat{x}\tilde{A}_x^{mi} + \hat{y}\tilde{A}_y^{mi} + \hat{z}\tilde{A}_z^{mi}$. The transverse electric field components can be expressed as

$$\tilde{E}_x^{mi} = -\frac{j\omega}{k_m^2} \left[(k_m^2 - k_x^2)\tilde{A}_x^{mi} - k_x k_y \tilde{A}_y^{mi} - j k_x \frac{\partial}{\partial z} \tilde{A}_z^{mi} \right] \quad (3-71)$$

$$\tilde{E}_y^{mi} = -\frac{j\omega}{k_m^2} \left[-k_x k_y \tilde{A}_x^{mi} + (k_m^2 - k_y^2)\tilde{A}_y^{mi} - j k_y \frac{\partial}{\partial z} \tilde{A}_z^{mi} \right]. \quad (3-72)$$

On the other hand, from (3-43) we find

$$\tilde{E}_x^{mi} = j k_x V_{mi}^e + j k_y V_{mi}^h \quad (3-73)$$

$$\tilde{E}_y^{mi} = j k_y V_{mi}^e - j k_x V_{mi}^h. \quad (3-74)$$

Eliminating \tilde{E}_x^{mi} and \tilde{E}_y^{mi} from (3-71)–(3-74), we have two independent equations and three unknown components of $\tilde{\underline{A}}^{mi}$. Therefore, the solution of these equations is not unique, and one of the components of the vector potential can be set to zero.

3.3.1. Traditional Form of the Green's Function

In the traditional approach [16], it is postulated that an x -directed current dipole generates the x - and z - components of the vector potential. Hence, eliminating \tilde{E}_x^{mi} and \tilde{E}_y^{mi} from (3-71)–(3-74), and letting $\tilde{A}_y^{mi} = 0$, we obtain

$$\tilde{A}_x^{mi} = -\frac{k_\rho^2}{\omega k_y} V_{mi}^h \quad (3-75)$$

$$\frac{\partial}{\partial z} \tilde{A}_z^{mi} = \frac{1}{j\omega} \left[k_m^2 V_{mi}^e - \frac{k_x}{k_y} k_{zm}^2 V_{mi}^h \right]. \quad (3-76)$$

Substituting (3-59) and (3-60) into (3-75) and (3-76), we have

$$\tilde{G}_{xx}^{mi} = \frac{1}{j\omega} \tilde{G}_{mi}^{V_h} \quad (3-77)$$

and

$$\frac{\partial}{\partial z} \tilde{G}_{xx}^{mi} = \frac{k_x}{\omega k_p^2} \left[k_m^2 \tilde{G}_{mi}^{V_e} - k_{zm}^2 \tilde{G}_{mi}^{V_h} \right], \quad (3-78)$$

from which we obtain

$$\tilde{G}_{xx}^{mi} = -\frac{k_x}{\omega k_p^2} \left[\frac{k_m^2}{k_{zm}^2} \frac{\partial}{\partial z} \tilde{G}_{mi}^{V_e} - \frac{\partial}{\partial z} \tilde{G}_{mi}^{V_h} \right]. \quad (3-79)$$

Similarly, we assume that the y -directed current dipole generates the y - and z - components of the vector potential. Changing x to y and k_x to k_y in (3-77) and (3-79), we obtain

$$\tilde{G}_{yy}^{mi} = \tilde{G}_{xx}^{mi} = \frac{1}{j\omega} \tilde{G}_{mi}^{V_h} \quad (3-80)$$

$$\tilde{G}_{zy}^{mi} = -\frac{k_y}{\omega k_p^2} \left[\frac{k_m^2}{k_{zm}^2} \frac{\partial}{\partial z} \tilde{G}_{mi}^{V_e} - \frac{\partial}{\partial z} \tilde{G}_{mi}^{V_h} \right]. \quad (3-81)$$

Thus, the elements of the dyadic (2-7) have been obtained in the Fourier transform domain. By using the relationships given in (3-8)–(3-13), one can express the space domain counterparts of (3-70) and (3-77)–(3-81) as

$$G_{xx}^{mi} = G_{yy}^{mi} = \frac{1}{2\pi j\omega} S_0 \left[\tilde{G}_{mi}^{V_h} \right] \quad (3-82)$$

$$G_{zx}^{mi} = -\frac{1}{2\pi j\omega} \cos \zeta S_1 \left[\frac{1}{k_p^2} \left(\frac{k_m^2}{k_{zm}^2} \frac{\partial}{\partial z} \tilde{G}_{mi}^{V_e} - \frac{\partial}{\partial z} \tilde{G}_{mi}^{V_h} \right) \right] \quad (3-83)$$

$$G_{xy}^{mi} = \tan \zeta G_{zx}^{mi} \quad (3-84)$$

and

$$G_{zz}^{mi} = \frac{1}{2\pi j\omega} \frac{\mu_m}{\epsilon_i} S_0 [\tilde{G}_{mi}^{Ie}] . \quad (3-85)$$

3.3.2. Alternative Form of the Green's Function

Taking an alternative approach [15], we suppose that a horizontal (x - or y -directed) dipole source gives rise to x and y components of \tilde{A}^{mi} . Eliminating \tilde{E}_x^{mi} and \tilde{E}_y^{mi} from (3-71)–(3-74), and letting $\tilde{A}_z^{mi} \equiv 0$, we obtain

$$\tilde{A}_x^{mi} = -\frac{1}{j\omega} \left(\frac{k_m^2}{k_{zm}^2} j k_x V_{mi}^e - j k_y V_{mi}^h \right) \quad (3-86)$$

$$\tilde{A}_y^{mi} = -\frac{1}{j\omega} \left(\frac{k_m^2}{k_{zm}^2} j k_y V_{mi}^e - j k_x V_{mi}^h \right) . \quad (3-87)$$

If the voltages V_{mi}^e and V_{mi}^h in (3-73) and (3-74) are those generated by an x -directed dipole, then $\tilde{A}_x^{mi} \equiv \tilde{G}_{xx}^{mi}$ and $\tilde{A}_y^{mi} \equiv \tilde{G}_{yx}^{mi}$. Hence, substituting from (3-59) and (3-60) into (3-86) and (3-87), we obtain

$$\tilde{G}_{xx}^{mi} = \frac{1}{j\omega} \left(\frac{k_m^2 k_x^2}{k_{zm}^2 k_\rho^2} \tilde{G}_{mi}^{Ve} + \frac{k_y^2}{k_\rho^2} \tilde{G}_{mi}^{Vh} \right) \quad (3-88)$$

$$\tilde{G}_{yx}^{mi} = \frac{k_x k_y}{j\omega k_\rho^2} \left(\frac{k_m^2}{k_{zm}^2} \tilde{G}_{mi}^{Ve} - \tilde{G}_{mi}^{Vh} \right) . \quad (3-89)$$

Similarly, substituting from (3-63) and (3-64) into (3-86) and (3-87), we obtain

$$\tilde{G}_{xy}^{mi} \equiv \tilde{G}_{yx}^{mi} \quad (3-90)$$

and

$$\tilde{G}_{yy}^{mi} = \frac{1}{j\omega} \left(\frac{k_m^2 k_y^2}{k_{zm}^2 k_\rho^2} \tilde{G}_{mi}^{Ve} + \frac{k_x^2}{k_\rho^2} \tilde{G}_{mi}^{Vh} \right). \quad (3-91)$$

That $\tilde{G}_{xy}^{mi} = \tilde{G}_{yx}^{mi}$ was already anticipated in (2-8).

Thus, we have obtained the elements of (2-8) in the Fourier transform domain. They can be expressed in the space domain as

$$G_{xx}^{mi} = \frac{1}{4\pi j\omega} \left\{ S_0 \left[\frac{k_m^2}{k_{zm}^2} \tilde{G}_{mi}^{Ve} + \tilde{G}_{mi}^{Vh} \right] - \cos \zeta S_2 \left[\frac{1}{k_\rho^2} \left(\frac{k_m^2}{k_{zm}^2} \tilde{G}_{mi}^{Ve} - \tilde{G}_{mi}^{Vh} \right) \right] \right\} \quad (3-92)$$

$$G_{yy}^{mi} = \frac{1}{4\pi j\omega} \left\{ S_0 \left[\frac{k_m^2}{k_{zm}^2} \tilde{G}_{mi}^{Ve} + \tilde{G}_{mi}^{Vh} \right] + \cos \zeta S_2 \left[\frac{1}{k_\rho^2} \left(\frac{k_m^2}{k_{zm}^2} \tilde{G}_{mi}^{Ve} - \tilde{G}_{mi}^{Vh} \right) \right] \right\} \quad (3-93)$$

$$G_{xy}^{mi} = G_{yx}^{mi} = -\frac{1}{4\pi j\omega} \sin 2\zeta S_2 \left[\frac{1}{k_\rho^2} \left(\frac{k_m^2}{k_{zm}^2} \tilde{G}_{mi}^{Ve} - \tilde{G}_{mi}^{Vh} \right) \right] \quad (3-94)$$

with G_{zz}^{mi} given by (3-85).

3.4. Electric Field in the Layered Medium due to Plane Wave Incident in Region 1

Consider an incident plane wave in Region 1, given as

$$\underline{E}^i(r) = (E_\theta \hat{\theta}_1 + E_\phi \hat{\phi}_1) e^{j\underline{k}_1 \cdot \underline{r}} \quad (3-95)$$

where the propagation vector \underline{k}_1 is

$$\underline{k}_1 = k_1 (\sin \theta_1 \cos \phi_1 \hat{x} + \sin \theta_1 \sin \phi_1 \hat{y} + \cos \theta_1 \hat{z}) \quad (3-96)$$

and $(\hat{\theta}_1, \hat{\phi}_1)$ define the angle of arrival of the plane wave in terms of the usual spherical coordinate convention. We can utilize the analysis in Sections 3.1—3.3

to obtain the total “incident” electric field in the m th layer due to the plane wave given in (3-95). We easily find that the incident field in the top layer ($m = 1$) is given as

$$\begin{aligned} \underline{E}_1^{inc}(\underline{r}) = & \\ & \left\{ \hat{x} \left[-E_\phi \sin \phi_1 \left(1 + \overleftarrow{\Gamma}_1^h e^{-j2k_1 \cos \theta_1 (z-z_1)} \right) \right. \right. \\ & + E_\theta \cos \phi_1 \cos \theta_1 \left(1 + \overleftarrow{\Gamma}_1^e e^{-j2k_1 \cos \theta_1 (z-z_1)} \right) \left. \right] \\ & + \hat{y} \left[E_\phi \cos \phi_1 \left(1 + \overleftarrow{\Gamma}_1^h e^{-j2k_1 \cos \theta_1 (z-z_1)} \right) \right. \\ & + E_\theta \sin \phi_1 \cos \theta_1 \left(1 + \overleftarrow{\Gamma}_1^e e^{-j2k_1 \cos \theta_1 (z-z_1)} \right) \left. \right] \\ & \left. - \hat{z} E_\theta \sin \theta_1 \left(1 - \overleftarrow{\Gamma}_1^e e^{-j2k_1 \cos \theta_1 (z-z_1)} \right) \right\} e^{jk_1 [\sin \theta_1 (\cos \phi_1 z + \sin \phi_1 y) + \cos \theta_1 z]} \end{aligned} \quad (3-97)$$

and the field in other layers ($m \neq 1$) as

$$\begin{aligned} \underline{E}_m^{inc}(\underline{r}) = & \\ & \left\{ \hat{x} \left[-E_\phi \sin \phi \left(1 + \overleftarrow{\Gamma}_1^h \right) \overleftarrow{T}_{m1}^{V_h}(z) + E_\theta \cos \phi_1 \frac{1}{\eta_1} \overleftarrow{Z}_1^e \left(1 - \overleftarrow{\Gamma}_1^e \right) \overleftarrow{T}_{m1}^{V_e}(z) \right] \right. \\ & + \hat{y} \left[E_\phi \cos \phi_1 \left(1 + \overleftarrow{\Gamma}_1^h \right) \overleftarrow{T}_{m1}^{V_h}(z) + E_\theta \sin \phi_1 \frac{1}{\eta_1} \overleftarrow{Z}_1^e \left(1 - \overleftarrow{\Gamma}_1^e \right) \overleftarrow{T}_{m1}^{V_e}(z) \right] \\ & \left. - \hat{z} E_\theta \frac{\eta_m}{\eta_1} \sin \theta_m \left(1 - \overleftarrow{\Gamma}_1^e \right) \overleftarrow{T}_{m1}^{I_e}(z) \right\} e^{jk_m (\cos \phi_1 \sin \theta_m z + \sin \phi_1 \sin \theta_m y + \cos \theta_m z)}, \end{aligned} \quad (3-98)$$

where \overleftarrow{Z}_1^e , $\overleftarrow{\Gamma}_1$, and \overleftarrow{T}_{m1} are given in Section 3.2, with $k_{zm} = k_m \cos \theta_m$, where θ_m can be obtained from the Snell’s law, $k_1 \sin \theta_1 = k_m \sin \theta_m$. In (3-98), $\eta_m = \sqrt{\mu_m / \epsilon_m}$ is the intrinsic impedance of the dielectric of region m .

CHAPTER 4

FORMULATION OF THE MIXED-POTENTIAL ELECTRIC FIELD INTEGRAL EQUATION

In this chapter, three different mixed-potential EFIEs for the problem of Fig. 2.1 are formulated and their properties discussed. One of the formulations (called Formulation C), which is found to be particularly well suited for the application of the method of moments, is specialized to the important cases of a scatterer or antenna of arbitrary shape residing in contiguous half-spaces and in a grounded slab.

As mentioned in Chapter 2, the decomposition embodied in (2-13) is non-unique, which means that an infinite number of different MPIEs is possible. We observe, however, by referring to (2-16), that the presence of the “correction” function \underline{P}^{mi} has the undesirable effect of introducing new elements in the dyadic kernel $\underline{\underline{K}}_A^{mi}$, in addition to those already present in $\underline{\underline{G}}_A^{mi}$. Ideally, of course, \underline{P}^{mi} should be zero, which—unfortunately—is only possible in a few special cases [15]. Hence, the best one can do is to develop MPIEs for which one or two of the components of \underline{P}^{mi} are zero. It is shown below that for the vector potential Green’s functions (2-7) and (2-8) the x and y components of \underline{P}^{mi} are not independent, thus leaving us, for each $\underline{\underline{G}}_A^{mi}$, with only two degrees of freedom: either $P_x^{mi} = P_y^{mi} = 0$ and $P_z^{mi} \neq 0$, or $P_x^{mi} \neq 0$, $P_y^{mi} \neq 0$, and $P_z^{mi} = 0$. Of the four possible “minimal” formulations, only three lead to distinct MPIEs. These three are discussed in detail below, where they are referred to as Formulations A, B, and C. Most of our derivations are done

in the Fourier transform domain defined in (3-1) and (3-2), which greatly simplifies the algebra.

4.1. Formulation A

In this formulation, we employ the alternative form of $\underline{\underline{G}}_A^{mi}$ given in (2-8). In the Fourier transform domain, the x , y , and z components of (2-13) become

$$\frac{j\omega}{k_m^2} (-jk_x \tilde{G}_{xx}^{mi} - jk_y \tilde{G}_{xy}^{mi}) = \frac{1}{j\omega} jk_x \tilde{K}_\phi^{mi} + j\omega \tilde{P}_x^{mi} \quad (4-1)$$

$$\frac{j\omega}{k_m^2} (-jk_x \tilde{G}_{xy}^{mi} - jk_y \tilde{G}_{yy}^{mi}) = \frac{1}{j\omega} jk_y \tilde{K}_\phi^{mi} + j\omega \tilde{P}_y^{mi} \quad (4-2)$$

$$\frac{j\omega}{k_m^2} \frac{\partial}{\partial z} \tilde{G}_{zz}^{mi} = \frac{1}{j\omega} \frac{\partial}{\partial z'} \tilde{K}_\phi^{mi} + j\omega \tilde{P}_z^{mi}. \quad (4-3)$$

Using (3-88) through (3-91) in (4-1) and (4-2), one finds that \tilde{P}_x^{mi} and \tilde{P}_y^{mi} are related by

$$\tilde{P}_y^{mi} = \frac{k_y}{k_x} \tilde{P}_x^{mi}. \quad (4-4)$$

In Formulation A, we choose $\tilde{P}_x^{mi} = \tilde{P}_y^{mi} = 0$, in which case K_ϕ^{mi} can be interpreted as the scalar potential of a point charge associated with a horizontal dipole [15].

Solving (4-1) or (4-2) for \tilde{K}_ϕ^{mi} , one obtains

$$\tilde{K}_\phi^{mi} = -j\omega \frac{\tilde{G}_{mi}^{V_e}}{k_{zm}^2}, \quad (4-5)$$

which can be substituted into (4-3) to yield

$$\tilde{P}_z^{mi} = \frac{\mu_i \epsilon_i - \mu_m \epsilon_m}{\epsilon_i k_{zm}^2} \tilde{I}_{mi}^{V_e} \quad (4-6)$$

where we have introduced for later convenience

$$\tilde{I}_{mi}^{V_q} = \begin{cases} \overrightarrow{Z}_{i-1}^q \tilde{G}_{ii}^{I_q}(z_{i-1}, z') \overrightarrow{T}_{mi}^{V_q}(z), & i-1 \geq m \geq 1 \\ -\overleftarrow{Z}_i^q \tilde{G}_{ii}^{I_q}(z_i, z') \overleftarrow{T}_{mi}^{V_q}(z), & n+1 \geq m > i+1 \end{cases} \quad (4-7)$$

in which the superscript “ q ” stands for “ e ” or “ h .” Observe that $\tilde{P}_z^{mi} \equiv 0$ when $m = i$, i.e., when the source and observation points are within the same layer.

Substituting (3-70), (3-88)—(3-91) and (4-6) into the Fourier domain counterpart of (2-16), and using the relations given in (3-8)—(3-13), one obtains the dyadic kernel

$$\begin{aligned} \underline{\underline{K}}_A^{mi}(\underline{r} | \underline{r}') &= \hat{x} \hat{x} K_{xx}^{mi} + \hat{y} \hat{y} K_{yy}^{mi} + \hat{z} \hat{z} K_{zz}^{mi} \\ &\quad + (\hat{x} \hat{y} + \hat{y} \hat{x}) K_{xy}^{mi} + \hat{x} \hat{z} K_{xz}^{mi} + \hat{y} \hat{z} K_{yz}^{mi} \end{aligned} \quad (4-8)$$

with the elements given by

$$\begin{aligned} K_{xx}^{mi} = G_{xx}^{mi} &= \frac{1}{4\pi j\omega} \left\{ k_m^2 S_0 \left(\frac{1}{k_{zm}^2} \tilde{G}_{mi}^{V_e} \right) + S_0 \left(\tilde{G}_{mi}^{V_h} \right) \right. \\ &\quad \left. + \cos 2\zeta S_2 \left[\frac{1}{k_\rho^2} \left(\tilde{G}_{mi}^{V_h} - \frac{k_m^2}{k_{zm}^2} \tilde{G}_{mi}^{V_e} \right) \right] \right\} \end{aligned} \quad (4-9)$$

$$\begin{aligned} K_{yy}^{mi} = G_{yy}^{mi} &= \frac{1}{4\pi j\omega} \left\{ k_m^2 S_0 \left(\frac{1}{k_{zm}^2} \tilde{G}_{mi}^{V_e} \right) + S_0 \left(\tilde{G}_{mi}^{V_h} \right) \right. \\ &\quad \left. - \cos 2\zeta S_2 \left[\frac{1}{k_\rho^2} \left(\tilde{G}_{mi}^{V_h} - \frac{k_m^2}{k_{zm}^2} \tilde{G}_{mi}^{V_e} \right) \right] \right\} \end{aligned} \quad (4-10)$$

$$K_{xy}^{mi} = G_{xy}^{mi} = \frac{1}{4\pi j\omega} \sin 2\zeta S_2 \left[\frac{1}{k_\rho^2} \left(\tilde{G}_{mi}^{V_h} - \frac{k_m^2}{k_{zm}^2} \tilde{G}_{mi}^{V_e} \right) \right] \quad (4-11)$$

$$K_{xz}^{mi} = \frac{\partial}{\partial x} P_z^{mi} = -\frac{\cos \zeta}{2\pi} S_1 (\tilde{P}_z^{mi}) \quad (4-12)$$

$$K_{yz}^{mi} = \frac{\partial}{\partial y} P_z^{mi} = -\frac{\sin \zeta}{2\pi} S_1 (\tilde{P}_z^{mi}) \quad (4-13)$$

$$K_{zz}^{mi} = G_{zz}^{mi} + \frac{\partial}{\partial z} P_z^{mi} = \frac{\mu_i}{2\pi j\omega \epsilon_m} S_0 (\tilde{G}_{mi}^{I_e}). \quad (4-14)$$

Finally, the Fourier inversion of \tilde{K}_ϕ^{mi} in (4-5) yields the scalar potential kernel

$$K_\phi^{mi} = -\frac{j\omega}{2\pi} S_0 \left(\frac{\tilde{G}_{mi}^{V_e}}{k_{zm}^2} \right). \quad (4-15)$$

We observe from (4-9) through (4-15) that in this formulation, when $m \neq i$, the effect of $\nabla \underline{P}^{mi}$ in (2-16) is to introduce two new entries, K_{xz}^{mi} and K_{yz}^{mi} , and to modify G_{zz}^{mi} . However, when the object is confined to a single layer ($m = i$), we simply have $\underline{K}_A^{mi} = \underline{G}_A^{mi}$, so no modification of the Green's function is required.

A useful property of Formulation A is the cancellation of the contour integrals in (2-15), which is the result of the continuity with respect to the z' coordinate of the scalar potential kernel at the i th interface: $K_\phi^{mi}(z' = z_i + 0) = K_\phi^{m,i+1}(z' = z_i - 0)$. We note, however, that a continuity with respect to the z coordinate does not hold, i.e., $K_\phi^{mi}(z = z_m + 0) \neq K_\phi^{m+1,i}(z = z_m - 0)$.

4.2. Formulation B

In this formulation, as in Formulation A, we employ the alternative form (2-8)

of $\underline{\underline{G}}_A^{mi}$. However, rather than choosing $\tilde{P}_x^{mi} = \tilde{P}_y^{mi} = 0$, we select $\tilde{P}_z^{mi} = 0$ in (4-1) through (4-3). In this case K_ϕ^{mi} can be interpreted as the scalar potential of a point charge associated with a vertical dipole [15]. From (4-3) and (3-70), we find

$$\tilde{K}_\phi^{mi} = -j\omega \frac{\tilde{G}_{mi}^{V_e}}{k_{zi}^2} \quad (4-16)$$

which can be substituted into (4-1) to yield

$$\tilde{P}_x^{mi} = \omega k_x \frac{\mu_m \epsilon_m - \mu_i \epsilon_i}{k_{zi}^2 k_{zm}^2} \tilde{G}_{mi}^{V_e} \quad (4-17)$$

which, in view of (4-4), also specifies \tilde{P}_y^{mi} .

Referring to (2-16) and proceeding as in Formulation A, we obtain the dyadic kernel

$$\begin{aligned} \underline{\underline{K}}_A^{mi}(\underline{r} | \underline{r}') &= \hat{x} \hat{x} K_{xx}^{mi} + \hat{y} \hat{y} K_{yy}^{mi} + \hat{z} \hat{z} K_{zz}^{mi} \\ &\quad + (\hat{x} \hat{y} + \hat{y} \hat{x}) K_{xy}^{mi} + \hat{z} \hat{x} K_{xz}^{mi} + \hat{z} \hat{y} K_{zy}^{mi} \end{aligned} \quad (4-18)$$

with the elements given by

$$\begin{aligned} K_{xx}^{mi} &= G_{xx}^{mi} + \frac{\partial}{\partial x} P_x^{mi} = \frac{1}{4\pi j\omega} \left\{ k_i^2 S_0 \left(\frac{1}{k_{zi}^2} \tilde{G}_{mi}^{V_e} \right) + S_0 \left(\tilde{G}_{mi}^{V_h} \right) \right. \\ &\quad \left. + \cos 2\zeta S_2 \left[\frac{1}{k_\rho^2} \left(\tilde{G}_{mi}^{V_h} - \frac{k_i^2}{k_{zi}^2} \tilde{G}_{mi}^{V_e} \right) \right] \right\} \end{aligned} \quad (4-19)$$

$$\begin{aligned} K_{yy}^{mi} &= G_{yy}^{mi} + \frac{\partial}{\partial y} P_y^{mi} = \frac{1}{4\pi j\omega} \left\{ k_i^2 S_0 \left(\frac{1}{k_{zi}^2} \tilde{G}_{mi}^{V_e} \right) + S_0 \left(\tilde{G}_{mi}^{V_h} \right) \right. \\ &\quad \left. - \cos 2\zeta S_2 \left[\frac{1}{k_\rho^2} \left(\tilde{G}_{mi}^{V_h} - \frac{k_i^2}{k_{zi}^2} \tilde{G}_{mi}^{V_e} \right) \right] \right\} \end{aligned} \quad (4-20)$$

$$K_{xy}^{mi} = G_{xy}^{mi} + \frac{\partial}{\partial x} P_y^{mi} = \frac{1}{4\pi j\omega} \sin 2\zeta S_2 \left[\frac{1}{k_\rho^2} \left(\tilde{G}_{mi}^{V_h} - \frac{k_i^2}{k_{zi}^2} \tilde{G}_{mi}^{V_e} \right) \right] \quad (4-21)$$

$$K_{zx}^{mi} = \frac{\partial}{\partial z} P_x^{mi} = \frac{\cos \zeta}{2\pi} S_1 (\bar{R}^{mi}) \quad (4-22)$$

$$K_{zy}^{mi} = \frac{\partial}{\partial z} P_y^{mi} = \frac{\sin \zeta}{2\pi} S_1 (\bar{R}^{mi}) \quad (4-23)$$

$$K_{zz}^{mi} = G_{zz}^{mi} = \frac{\mu_m}{2\pi j\omega \epsilon_i} S_0 (\tilde{G}_{mi}^{I_e}) \quad (4-24)$$

where \bar{R}^{mi} is nonzero only for $m \neq i$ and is given by

$$\bar{R}^{mi} = \frac{\mu_i \epsilon_i - \mu_m \epsilon_m}{\epsilon_m k_{zi}^2} \tilde{I}_{mi}^{I_e} \quad (4-25)$$

in which $\tilde{I}_{mi}^{I_e}$ can be obtained from $\tilde{I}_{mi}^{V_e}$ given in (4-7) by replacing in the latter the characteristic impedances Z_i^e by their reciprocals.

Finally, the Fourier inversion of \tilde{K}_ϕ^{mi} in (4-16) gives the scalar potential kernel

$$K_\phi^{mi} = -\frac{j\omega}{2\pi} S_0 \left(\frac{\tilde{G}_{mi}^{V_e}}{k_{zi}^2} \right). \quad (4-26)$$

We note that in Formulation B two new entries (K_{zx}^{mi} and K_{zy}^{mi}), not present in $\underline{\underline{G}}_A^{mi}$, are introduced to the dyadic kernel $\underline{\underline{K}}_A^{mi}$. Also, extra terms are added to G_{zz}^{mi} , G_{yy}^{mi} , and G_{xy}^{mi} . In the case where the object is confined to a single layer ($m = i$), $\underline{\underline{K}}_A^{mi} = \underline{\underline{G}}_A^{mi}$, and Formulation B becomes identical to Formulation A.

The continuity properties of the scalar potential kernel in Formulation B are complementary to those in Formulation A; that is, in the present case $K_\phi^{mi}(z' = z_i + 0) \neq K_\phi^{m,i+1}(z' = z_i - 0)$ and $K_\phi^{mi}(z = z_m + 0) = K_\phi^{m+1,i}(z = z_m - 0)$. As a

result, the contour integrals in (2-15) do exist when the object penetrates one or more of the interfaces.

4.3. Formulation C

The point of departure in this formulation is the traditional form of $\underline{\underline{G}}_A^{mi}$ given in (2-7). Using it in (2-13), we obtain in the Fourier transform domain

$$\frac{j\omega}{k_m^2} \left(-jk_x \tilde{G}_{xx}^{mi} + \frac{\partial}{\partial z} \tilde{G}_{zx}^{mi} \right) = \frac{1}{j\omega} j k_x \tilde{K}_\phi^{mi} + j\omega \tilde{P}_x^{mi} \quad (4-27)$$

$$\frac{j\omega}{k_m^2} \left(-jk_y \tilde{G}_{xx}^{mi} + \frac{\partial}{\partial z} \tilde{G}_{zy}^{mi} \right) = \frac{1}{j\omega} j k_y \tilde{K}_\phi^{mi} + j\omega \tilde{P}_y^{mi} \quad (4-28)$$

$$\frac{j\omega}{k_m^2} \frac{\partial}{\partial z} \tilde{G}_{zz}^{mi} = \frac{1}{j\omega} \frac{\partial}{\partial z'} \tilde{K}_\phi^{mi} + j\omega \tilde{P}_z^{mi}. \quad (4-29)$$

From (4-27) and (4-29), and referring to (3-79) through (3-81), we find that (4-4) still holds. Since G_{zz}^{mi} in the present case is the same as that in the “alternative” Green’s function (2-8), specifying $\tilde{P}_z^{mi} = 0$ results in an MPIE identical to that in Formulation B. We therefore set $\tilde{P}_x^{mi} = \tilde{P}_y^{mi} = 0$ in (4-27) and (4-28), which yields the scalar potential kernel

$$\tilde{K}_\phi^{mi} = \frac{j\omega}{k_\rho^2} \left(\tilde{G}_{mi}^{V_\epsilon} - \tilde{G}_{mi}^{V_h} \right). \quad (4-30)$$

From the above and (4-29), there results

$$\tilde{P}_z^{mi} = \frac{1}{j\omega} \left[\frac{\mu_m}{k_m^2 \epsilon_i} \frac{\partial}{\partial z} \tilde{G}_{mi}^{I_\epsilon} + \frac{1}{k_\rho^2} \frac{\partial}{\partial z'} \left(\tilde{G}_{mi}^{V_h} - \tilde{G}_{mi}^{V_\epsilon} \right) \right]. \quad (4-31)$$

Substituting (3-70), (3-79) through (3-81) and (4-31) into the Fourier domain counterpart of (2-16), and using the relations given in (3-8)—(3-13), we obtain the dyadic kernel

$$\underline{\underline{K}}_A^{mi}(\underline{r} | \underline{r}') = (\hat{x}\hat{x} + \hat{y}\hat{y}) K_{xx}^{mi} + \hat{x}\hat{z} K_{xz}^{mi} + \hat{y}\hat{z} K_{yz}^{mi} + \hat{z}\hat{x} K_{zx}^{mi} + \hat{z}\hat{y} K_{zy}^{mi} + \hat{z}\hat{z} K_{zz}^{mi} \quad (4-32)$$

with the elements given by

$$K_{xx}^{mi} = G_{xx}^{mi} = \frac{1}{2\pi j\omega} S_0 (\tilde{G}_{mi}^{V_h}) \quad (4-33)$$

$$K_{xz}^{mi} = \frac{\partial}{\partial x} P_z^{mi} = -\frac{\mu_i}{2\pi j\omega \epsilon_m} \cos \zeta S_1 \left[\frac{1}{k_\rho^2} \left(\tilde{W}_{mi}^{V_e} - \frac{k_m^2}{k_{zm}^2} \tilde{W}_{mi}^{V_h} \right) \right] \quad (4-34)$$

$$K_{yz}^{mi} = \frac{\partial}{\partial y} P_z^{mi} = -\frac{\mu_i}{2\pi j\omega \epsilon_m} \sin \zeta S_1 \left[\frac{1}{k_\rho^2} \left(\tilde{W}_{mi}^{V_e} - \frac{k_m^2}{k_{zm}^2} \tilde{W}_{mi}^{V_h} \right) \right] \quad (4-35)$$

$$K_{zx}^{mi} = G_{zx}^{mi} = -\frac{1}{2\pi j\omega} \cos \zeta S_1 \left[\frac{1}{k_\rho^2} \left(\frac{k_m^2}{k_{zm}^2} \tilde{W}_{mi}^{I_e} - \tilde{W}_{mi}^{I_h} \right) \right] \quad (4-36)$$

$$K_{zy}^{mi} = G_{zy}^{mi} = -\frac{1}{2\pi j\omega} \sin \zeta S_1 \left[\frac{1}{k_\rho^2} \left(\frac{k_m^2}{k_{zm}^2} \tilde{W}_{mi}^{I_e} - \tilde{W}_{mi}^{I_h} \right) \right] \quad (4-37)$$

$$K_{zz}^{mi} = G_{zz}^{mi} + \frac{\partial}{\partial z} P_z^{mi} = \frac{\mu_m}{2\pi j\omega \epsilon_i} S_0 \left[\tilde{G}_{mi}^{I_e} - \frac{k_i^2}{k_\rho^2} \left(\frac{k_{zm}^2}{k_m^2} \tilde{G}_{mi}^{I_e} - \tilde{G}_{mi}^{I_h} \right) \right] \quad (4-38)$$

where we have introduced

$$\tilde{W}_{ii}^V = \frac{j k_{zi}}{2 Z_i D_i} \left\{ \overleftarrow{\Gamma}_i e^{-jk_{zi}[(z+z')-2z_i]} - \overrightarrow{\Gamma}_{i-1} e^{-jk_{zi}[2z_{i-1}-(z+z')]} \right\}$$

$$+ 2j \overleftarrow{\Gamma}_i \overrightarrow{\Gamma}_{i-1} e^{-j2\psi_i} \sin [k_{zi}(z - z')] \Big\}, \quad m = i \quad (4-39)$$

$$\tilde{W}_{mi}^V = -\frac{j k_{zm}}{Z_m} \tilde{I}_{mi}^V, \quad m \neq i \quad (4-40)$$

with \tilde{I}_{mi}^V given in (4-7). For notational simplicity, we have suppressed in (4-39) and (4-40) the superscripts "e" or "h". We note that one can obtain \tilde{W}_{mi}^I from \tilde{W}_{mi}^V by replacing in the latter the characteristic impedances Z_i by their reciprocals.

Finally, the Fourier inversion of (4-30) gives

$$K_\phi^{mi} = \frac{j\omega}{2\pi} S_0 \left[\frac{1}{k_\rho^2} (\tilde{G}_{mi}^{Ve} - \tilde{G}_{mi}^{Vh}) \right]. \quad (4-41)$$

As in Formulation A, this K_ϕ^{mi} may be interpreted as the scalar potential of a point charge associated with a horizontal dipole [15]. However, these two potentials are not identical, since each corresponds to a different form of the vector potential Green's function.

We observe from (4-33) through (4-38) that Formulation C introduces two new entries (K_{xz}^{mi} and K_{yz}^{mi}), not present in $\underline{\underline{G}}_A^{mi}$, to the dyadic kernel. Also, extra terms are added to G_{zz}^{mi} . In contrast to Formulations A and B, these modifications occur even if the object is confined to a single layer. As in Formulation A, the scalar potential kernel in the present case has the continuity property that $K_\phi^{mi}(z' = z_i + 0) = K_\phi^{m,i+1}(z' = z_i - 0)$, which causes the contour integrals in (2-15) to cancel. Formulation C also shares with Formulation B the useful property that $K_\phi^{mi}(z = z_m + 0) = K_\phi^{m+1,i}(z = z_m - 0)$.

4.4. Discussion

The properties of three MPIEs are summarized for easy reference in Table 4.1. Each of the three formulations, called A, B or C, can be derived from either the alternative or the traditional form of the dyadic Green's function for the vector potential. These two dyadics are shown in matrix form in the first column of Table 4.1. We note that Formulation A is derived from the alternative forms of $\underline{\underline{G}}_A^{mi}$, Formulation C from the traditional form, and Formulation B from either of the two (this is due to the fact that both forms of $\underline{\underline{G}}_A^{mi}$ share the same G_{zz}^{mi}). The distinguishing feature of each of the three formulations is the choice of the scalar potential kernel K_ϕ^{mi} , which also specifies the "correction" vector \underline{P}^{mi} according to (2-13). Although, as the second column of Table 4.1 indicates, the scalar potential kernels in Formulations A and C are both associated with a horizontal dipole, they are different, because they correspond to different vector potential Green's functions. In Formulation B, K_ϕ^{mi} is that associated with a vertical dipole. Actually, by properly choosing K_ϕ^{mi} , one can also derive Formulation A from the traditional form of $\underline{\underline{G}}_A^{mi}$, and Formulation C from the alternative form.

The forms of the dyadic vector potential kernel are shown for each of the three formulations in column three. Comparing this column with column one, we observe that in all three formulations two new entries, in addition to those already present in $\underline{\underline{G}}_A^{mi}$, appear in $\underline{\underline{K}}_A^{mi}$, which is of course undesirable. We note, however (column four), that in Formulations A and B the number of the entries in $\underline{\underline{K}}_A^{mi}$ is not increased over that in $\underline{\underline{G}}_A^{mi}$, when the object is confined to a single layer ($m = i$). We should also point out that the correspondence between the number of entries in $\underline{\underline{K}}_A^{mi}$ and the number of distinct Sommerfeld-type integrals that need be evaluated is not one-

TABLE 4.1.

SUMMARY OF THE PROPERTIES OF THE THREE MIXED-POTENTIAL FORMULATIONS

Form of $\underline{\underline{G}}_A^{mi}$	Choice of K_ϕ^{mi}	Form of $\underline{\underline{K}}_A^{mi}$	Properties of $\underline{\underline{K}}_A^{mi}$ for $m = i$	Continuity of K_ϕ^{mi} at the interfaces	Contour integrals	Formulation and authors
Alternative: $\begin{bmatrix} G_{zz}^{mi} & G_{xy}^{mi} & 0 \\ G_{xy}^{mi} & G_{yy}^{mi} & 0 \\ 0 & 0 & G_{zz}^{mi} \end{bmatrix}$	K_ϕ^{mi} associated with horizontal dipole: $P_x^{mi} = P_y^{mi} = 0$ $P_z^{mi} \neq 0$	$\begin{bmatrix} K_{zz}^{mi} & K_{xy}^{mi} & K_{xz}^{mi} \\ K_{xy}^{mi} & K_{yy}^{mi} & K_{yz}^{mi} \\ 0 & 0 & K_{zz}^{mi} \end{bmatrix}$	$\underline{\underline{K}}_A^{mi} = \underline{\underline{G}}_A^{mi}$	$K_\phi^{mi}(z' = z_i^+) = K_\phi^{m,i+1}(z' = z_i^-)$ $K_\phi^{mi}(z = z_m^+) \neq K_\phi^{m+1,i}(z = z_m^-)$	No	A Johnson [19] (vertical tube); Michalski & Smith [22] (horizontal wires)
	K_ϕ^{mi} associated with vertical dipole: $P_x^{mi} \neq 0, P_y^{mi} \neq 0$ $P_z^{mi} = 0$	$\begin{bmatrix} K_{zz}^{mi} & K_{xy}^{mi} & 0 \\ K_{xy}^{mi} & K_{yy}^{mi} & 0 \\ K_{xz}^{mi} & K_{yz}^{mi} & K_{zz}^{mi} \end{bmatrix}$	$\underline{\underline{K}}_A^{mi} = \underline{\underline{G}}_A^{mi}$ $K_{zz}^{mi} = K_{xy}^{mi} = 0$	$K_\phi^{mi}(z' = z_i^+) \neq K_\phi^{m,i+1}(z' = z_i^-)$ $K_\phi^{mi}(z = z_m^+) = K_\phi^{m+1,i}(z = z_m^-)$	Yes	B Michalski & Zheng [40] (thin wire)
Traditional: $\begin{bmatrix} G_{zz}^{mi} & 0 & 0 \\ 0 & G_{zz}^{mi} & 0 \\ G_{xz}^{mi} & G_{xy}^{mi} & G_{zz}^{mi} \end{bmatrix}$	K_ϕ^{mi} associated with horizontal dipole: $P_x^{mi} = P_y^{mi} = 0$ $P_z^{mi} \neq 0$	$\begin{bmatrix} K_{zz}^{mi} & 0 & K_{xz}^{mi} \\ 0 & K_{xz}^{mi} & K_{yz}^{mi} \\ K_{xz}^{mi} & K_{yz}^{mi} & K_{zz}^{mi} \end{bmatrix}$		$K_\phi^{mi}(z' = z_i^+) = K_\phi^{m,i+1}(z' = z_i^-)$ $K_\phi^{mi}(z = z_m^+) = K_\phi^{m+1,i}(z = z_m^-)$	No	C Mosig & Gardiol [17] (planar patch); Michalski [23,24] (single layer); Michalski, et al. [21] (horizontal wires); Wilton & Singh [20] (periodic planar slots)

to-one. In fact, we can show by referring to Sections 4.1—4.3 that in the general case only four distinct Sommerfeld integrals are required in all three formulations. When $m = i$, the number of distinct integrals in Formulations A and B reduces to three.

As mentioned at the end of Chapter 2, one may leave the \underline{P}^{mi} term as a part of the scalar potential (cf. (2-15)), thus avoiding the modification of the vector potential kernel as in (2-16). However, since this would constitute a departure from the standard form of the MPIE [4,5], we prefer to proceed according to (2-16). Although in our formulations some of the terms introduced to $\underline{\underline{K}}_A^{mi}$ by $\nabla \underline{P}^{mi}$ in (2-16) become singular when \underline{r} and \underline{r}' coincide on an interface, they are no more singular than the terms already present in $\underline{\underline{G}}_A^{mi}$, and can be handled in a similar way as the latter.

The continuity properties of the scalar potential kernels across the interfaces are summarized in column five of Table 4.1. In Formulations A and C, K_ϕ^{mi} is continuous with respect to z' , which results in the cancellation of the undesirable contour integrals in (2-15) (cf. column six). In Formulations B and C, K_ϕ^{mi} is continuous with respect to z , which results in considerable simplifications in the numerical procedure when the object penetrates one or more interfaces. This last point can be fully appreciated only after we have discussed the details of the MOM procedure in the next chapter.

We conclude from the above summary that when the object is confined to a single layer, Formulations A and B become identical and are preferable to Formulation C, because they have fewer terms in $\underline{\underline{K}}_A^{mi}$. In the general case, Formulation C enjoys a clear advantage over Formulations A and B, because it does not have

contour integrals and because its scalar potential kernel is continuous at the interfaces with respect to z , which results in the simplifications mentioned above. If we had to choose between Formulations A and B, we would prefer the latter, because the advantages of having the scalar potential kernel continuous with respect to z more than compensate for the complications caused by the presence of the contour integrals. This point is further elaborated upon in the next chapter.

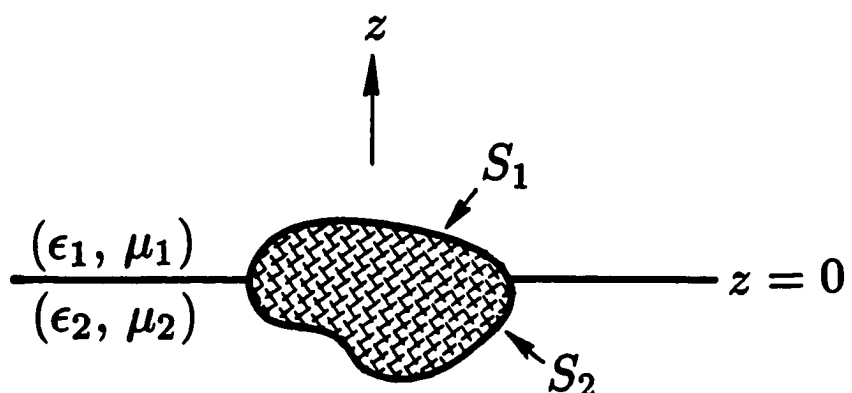
The previous works related to the mixed-potential EFIE and reviewed in Chapter 1 can be classified as shown in the last column of Table 4.1.

CHAPTER 5

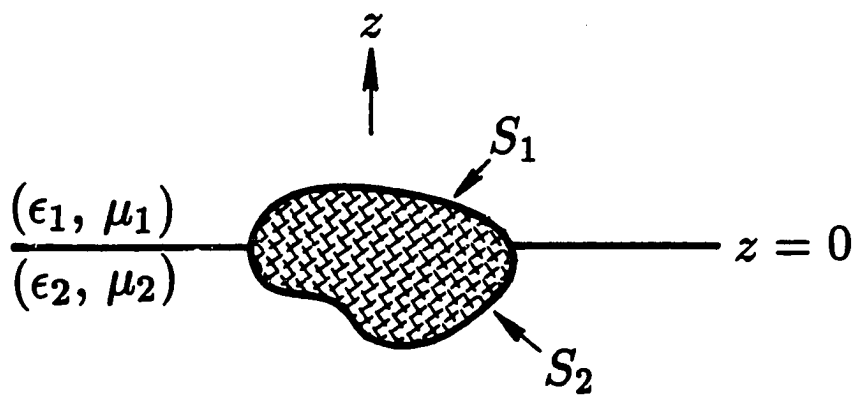
NUMERICAL METHOD

In the previous chapter, three different mixed-potential electric field integral equations (MPIEs)—called Formulations A, B and C—have been derived for perfectly electrically conducting (PEC) antennas or scatterers residing in plane-stratified dielectric media with an arbitrary number of layers. One of the alternative MPIEs—called Formulation C—has been found to be particularly well suited for the application of the method of moments (MOM) procedures originated by Wilton and his co-workers [4,5,7]. This formulation is adopted here in conjunction with those procedures to analyze the radiation and scattering by a PEC object of arbitrary shape residing in layered media. For simplicity, but without loss of generality, we describe this method in the context of the two-media problem illustrated in Fig. 5.1. Also, for simplicity, the interface between the two media is taken to be the xy plane of a Cartesian coordinate system. The upper ($z > 0$) half-space, which is characterized by ϵ_1 and μ_1 , will be referred to as region 1, and the lower ($z < 0$) half space in Fig. 5.1a, or the slab ($-d < z < 0$) in Fig. 5.1b, both characterized by ϵ_2 and μ_2 , as region 2. The parts of the surface S of the object which are in regions 1 and 2 are denoted as S_1 and S_2 , respectively.

As was already mentioned, based on the analysis of Section 4.4, Formulation C has been selected for the problems of Fig. 5.1. Hence, upon specializing the MPIE



(a)



(b)

Fig. 5.1. A PEC object of arbitrary shape embedded in (a) contiguous half-spaces, and (b) a grounded slab.

of (2-15) to the present cases, one obtains

$$\hat{\underline{n}}_m \times \sum_{i=1}^2 \left[j\omega \underline{A}^{mi}(\underline{r}) + \nabla \phi^{mi}(\underline{r}) \right] = \hat{\underline{n}}_m \times \underline{E}_m^{inc}(\underline{r}), \quad \underline{r} \text{ on } S_m, \quad m = 1, 2 \quad (5-1)$$

where, for notational simplicity, we have introduced

$$\underline{A}^{mi}(\underline{r}) = \int_{S_i} \underline{\underline{K}}_A^{mi}(\underline{r} | \underline{r}') \cdot \underline{J}(\underline{r}') dS' \quad (5-2)$$

$$\phi^{mi}(\underline{r}) = \int_{S_i} K_\phi^{mi}(\underline{r} | \underline{r}') q(\underline{r}') dS' \quad (5-3)$$

in which the kernel elements are given in the Appendix. The integrals (5-2) and (5-3) represent the modified potentials, and should not be confused with the original potentials given in (2-4) and (2-5).

We note that the contour integrals encountered in (2-15) are absent in (5-1), which is characteristic of Formulation C. The quantity of interest for the scattering and radiation problems is the surface current distribution on S , from which other characteristics, such as the far field pattern or radar cross-section, can be readily computed. For the transmission line problem, there is no excitation and (5-1) becomes a non-standard eigenvalue problem, with the propagation constants as eigenvalues and the modal current distributions as eigenfunctions.

In the numerical procedures, the MOM schemes developed in [3,4,5,7] are employed. These procedures are modified to account for the dyadic character of the vector potential kernel, to ensure the current continuity across the interface, and to allow for the charge discontinuity there [19]. In the MOM, basis functions are chosen to represent the unknown currents, testing functions are chosen to enforce the integral equation, and these are used to derive an impedance matrix approximant

to the integral equation.

5.1. Surface of Arbitrary Shape

Following the procedure described by Rao, Wilton, and Glisson [5], the surface S of the object is modeled in terms of triangular patches in a manner suggested in Fig. 5.2. The surface current density on S is approximated as

$$\underline{J}(\underline{r}) = \sum_{n=1}^N I_n \underline{f}_n(\underline{r}) \quad (5-4)$$

where N is the number of interior (nonboundary) edges and \underline{f}_n is the vector basis function defined on the adjacent triangles associated with the n th edge, and is given as

$$\underline{f}_n(\underline{r}) = \begin{cases} \underline{f}_n^+ = \frac{l_n}{2A_n^+} \underline{\rho}_n^+, & \underline{r} \text{ in } T_n^+ \\ \underline{f}_n^- = \frac{l_n}{2A_n^-} \underline{\rho}_n^-, & \underline{r} \text{ in } T_n^- \\ 0, & \text{otherwise} \end{cases} \quad (5-5)$$

in which l_n is the length of the edge, A_n^\pm is the area of triangle T_n^\pm , and $\underline{\rho}_n^\pm$ is the position vector, as shown in Fig. 5.3. The expansion for the surface charge density q , which is obtained by using (5-4) in the equation of continuity, calls for the surface divergence of \underline{f}_n , which is found as

$$\nabla_s \cdot \underline{f}_n = \begin{cases} \frac{l_n}{A_n^+}, & \underline{r} \text{ in } T_n^+ \\ -\frac{l_n}{A_n^-}, & \underline{r} \text{ in } T_n^- \\ 0, & \text{otherwise} \end{cases} \quad (5-6)$$

When the expansions for \underline{J} and q are used in (5-1) and the resulting equations

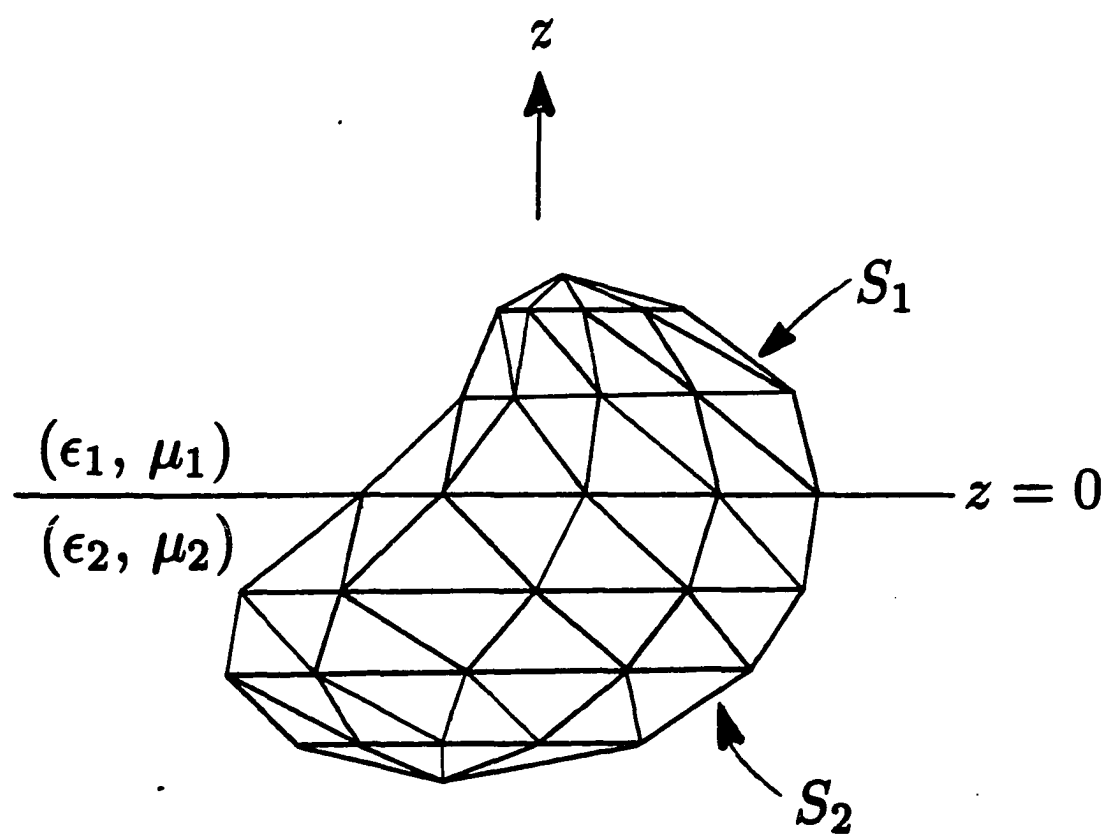


Fig. 5.2. Triangle-patch model of an arbitrary surface penetrating the interface between dissimilar media.

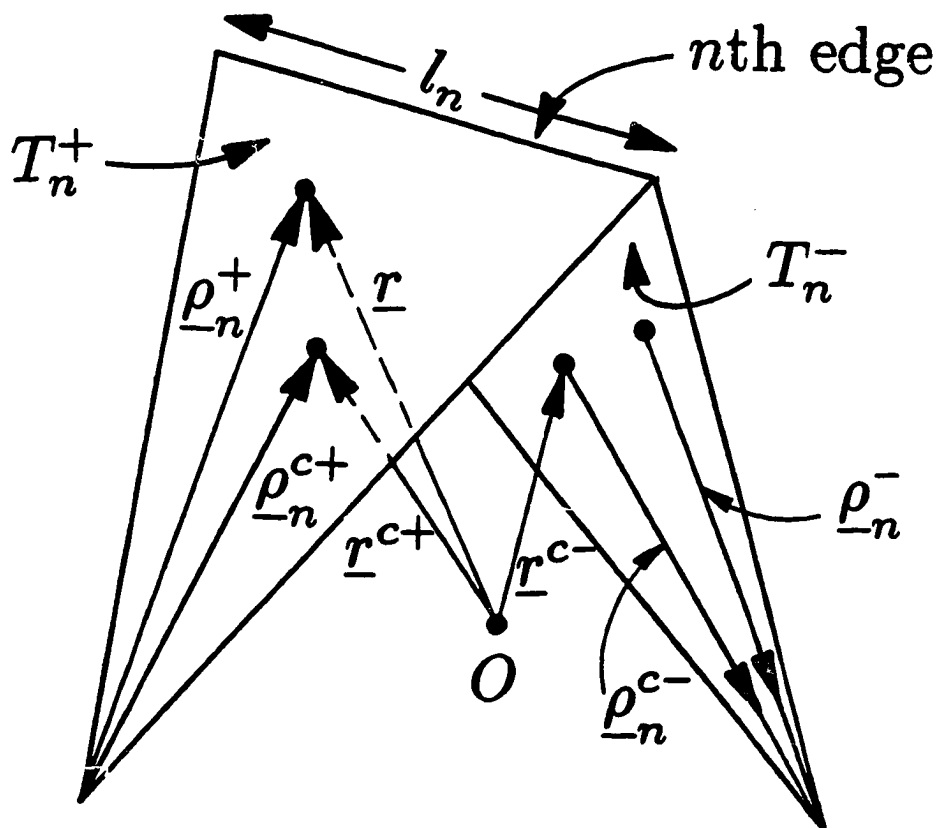


Fig. 5.3. Local coordinates associated with an edge.

tested with \underline{f}_n , an $N \times N$ system of linear equations is obtained, which may be written in matrix form as

$$[Z_{pn}][I_n] = [V_p] \quad (5-7)$$

where the elements of Z_{pn} and V_p are given as

$$Z_{pn} = l_p \left[\frac{j\omega}{2} (A_{pn}^- + A_{pn}^+) - \frac{1}{j\omega} (\Phi_{pn}^- - \Phi_{pn}^+) \right] \quad (5-8)$$

$$V_p = \frac{l_p}{2} (E_p^- + E_p^+) \quad (5-9)$$

where $p, n = 1, 2, \dots, N$, and

$$A_{pn}^\pm = \int_{S_i} \underline{\rho}_p^{c\pm} \cdot \underline{K}_A^{mi} (\underline{r}_p^{c\pm} | \underline{r}') \cdot \underline{f}_n (\underline{r}') dS' \quad (5-10)$$

$$\Phi_{pn}^\pm = \int_{S_i} K_\phi^{mi} (\underline{r}_p^{c\pm} | \underline{r}') \nabla'_s \cdot \underline{f}_n (\underline{r}') dS' \quad (5-11)$$

$$E_p^\pm = \underline{\rho}_p^{c\pm} \cdot \underline{E}_m^{inc} (\underline{r}_p^{c\pm}). \quad (5-12)$$

In the above, $\underline{\rho}_p^{c\pm}$ is the vector between the free vertex and the centroid of T_p^\pm , with $\underline{\rho}_p^{c-}$ directed toward and $\underline{\rho}_p^{c+}$ directed away from the vertex, and $\underline{r}_p^{c\pm}$ is the vector from the coordinate origin to the centroid of T_p^\pm (Fig. 5.3).

It is worthwhile to elaborate on one aspect of the above procedure, which is peculiar to the layered medium case. As suggested in Fig. 5.2, the triangle-patch model of S must take into account the position of the interface, since no triangular patch is allowed to cross it. This arrangement ensures the continuity of

the current on S across the interface and allows for the discontinuity of the charge there (cf. (5-5), (5-6)). A typical triangle pair associated with edge p on the interface is illustrated in Fig. 5.4. In testing (5-1) with \underline{f}_p , one should bear in mind that T_p^- and T_p^+ are in different layers. For example, testing $\nabla\phi^{mi}$ in (5-1) with \underline{f}_p yields

$$\begin{aligned} \int_{T_p^+} \nabla\phi^{2i} \cdot \underline{f}_p^+ dS + \int_{T_p^-} \nabla\phi^{1i} \cdot \underline{f}_p^- dS &= - \int_{T_p^+} \phi^{2i} \nabla \cdot \underline{f}_p^+ dS - \int_{T_p^-} \phi^{1i} \nabla \cdot \underline{f}_p^- dS \\ &\quad + \int_{l_p} (\phi^{2i} \underline{f}_p^+ \cdot \hat{\underline{u}}_p^+ + \phi^{1i} \underline{f}_p^- \cdot \hat{\underline{u}}_p^-) dl \end{aligned} \quad (5-13)$$

where use has been made of a Gauss' theorem (p. 503, [37]). We observe the undesirable line integral in (5-13), which does not occur for objects in homogeneous space. Even in the present case, however, this integral disappears for Formulations B and C (see Chapter 4) in view of the continuity of the scalar potential kernels as z crosses an interface and the fact that $\hat{\underline{u}}_p^+ \cdot \underline{f}_p^+ = -\hat{\underline{u}}_p^- \cdot \underline{f}_p^-$ on l_p , which follows from (5-5). In Formulation A, the line integrals contribute a contour integral at the intersection of S with the interface, quite similar to that in (2-14), which is present in Formulation B. However, due to the approximations made in the testing procedure [5], the latter is actually easier to handle than the former—hence our statement in Chapter 4 regarding the superiority of Formulation B over Formulation A. Formulation C is, of course, free of either of these contour integrals.

It is worth noting that, apart from the presence of the Sommerfeld integrals, the only difference between (5-8)–(5-12) and their free space counterparts [5] is the dyadic character of the vector potential kernel in (5-10). The surface integrals in (5-10)–(5-11) can be efficiently evaluated in normalized area coordinates and reused for different matrix elements, as described in [5].

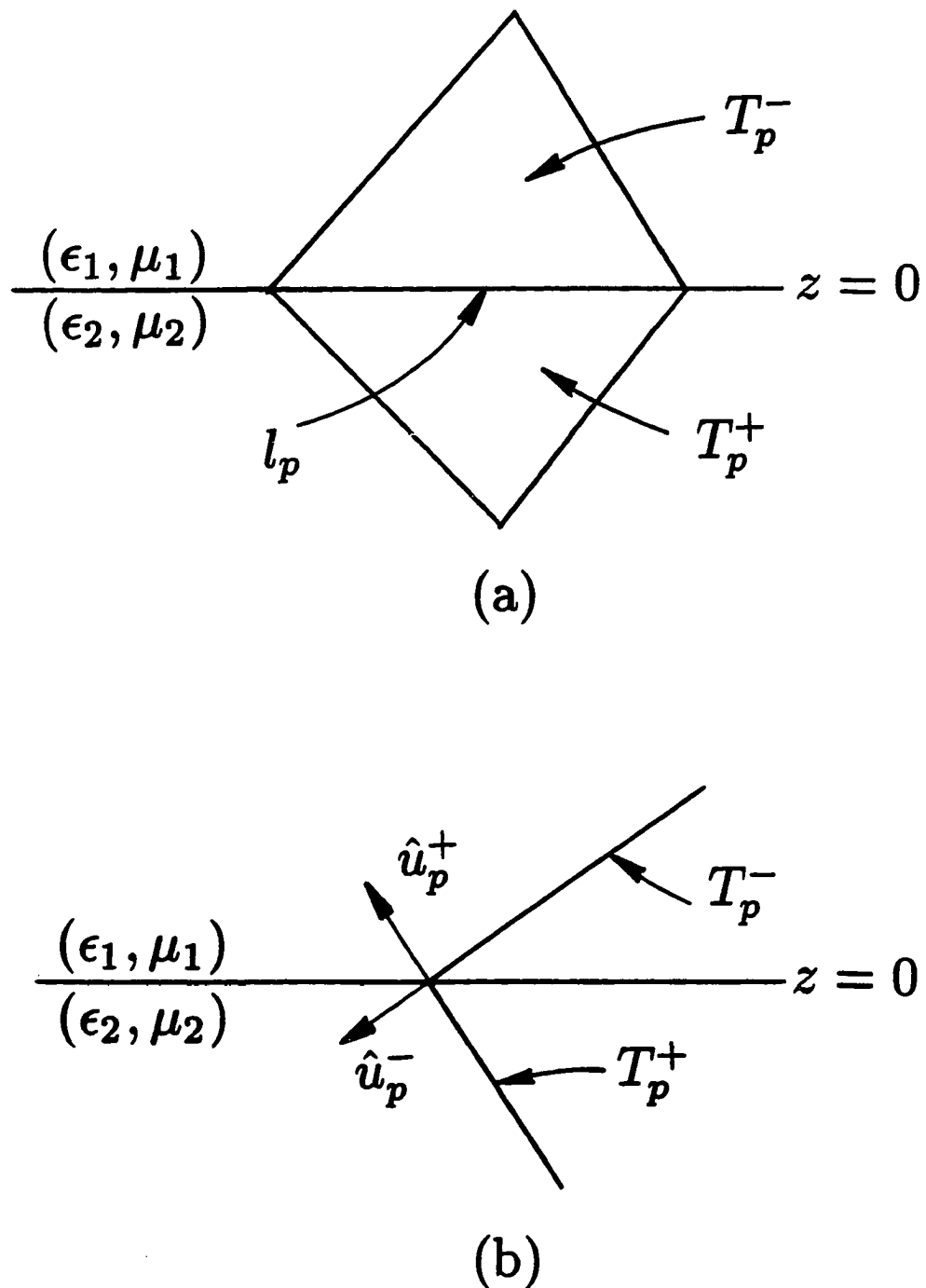


Fig. 5.4. (a) Side view and (b) cross-sectional view of a triangle pair straddling the interface between contiguous half-spaces.

As in the free space problem, the integrands of $\underline{A}^{mi}(\underline{r})$ and $\Phi^{mi}(\underline{r})$ are singular at $\underline{r} = \underline{r}'$, i.e., when the observation point coincides with the source point. As mentioned in the Appendix, this singularity arises from the closed form part of the Green's function. Thus, when the observation point is close to the source point, extraction of the $\frac{1}{|\underline{r} - \underline{r}'|}$ behavior is necessary before numerical integration is performed. The technique developed in [41] may be used for the treatment of such singularities.

5.2. Thin Wire of Arbitrary Shape

We next consider a thin-wire structure of arbitrary shape with radius a , which may penetrate the interface between two dissimilar dielectric layers, as shown in Fig. 5.5. The parts of the wire which are in regions 1 and 2 are denoted as L_1 and L_2 , respectively. The wire is modeled in terms of $N + 1$ straight tubular segments and the vectors \underline{r}_n , $n = 0, 1, \dots, N+1$, defined with respect to the global coordinate origin O , locate the end points of the linear segments, as illustrated in Fig. 5.5. The same points are designated by l_n with respect to the local arc length coordinate l along the axis of the wire. Unit vectors parallel to the axis of each segment are defined as

$$\hat{\underline{l}}_{n+\frac{1}{2}} = \frac{\underline{r}_{n+1} - \underline{r}_n}{|\underline{r}_{n+1} - \underline{r}_n|}. \quad (5-14)$$

By making use of the thin wire approximation [3], we may express the potentials in (5-1) as

$$\underline{A}^{mi}(\underline{r}) = \underline{A}^{mi}(l) = \int_{L_i} \underline{\underline{K}}_A^{mi}(l | l') \cdot \underline{I}(l') dl' \quad (5-15)$$

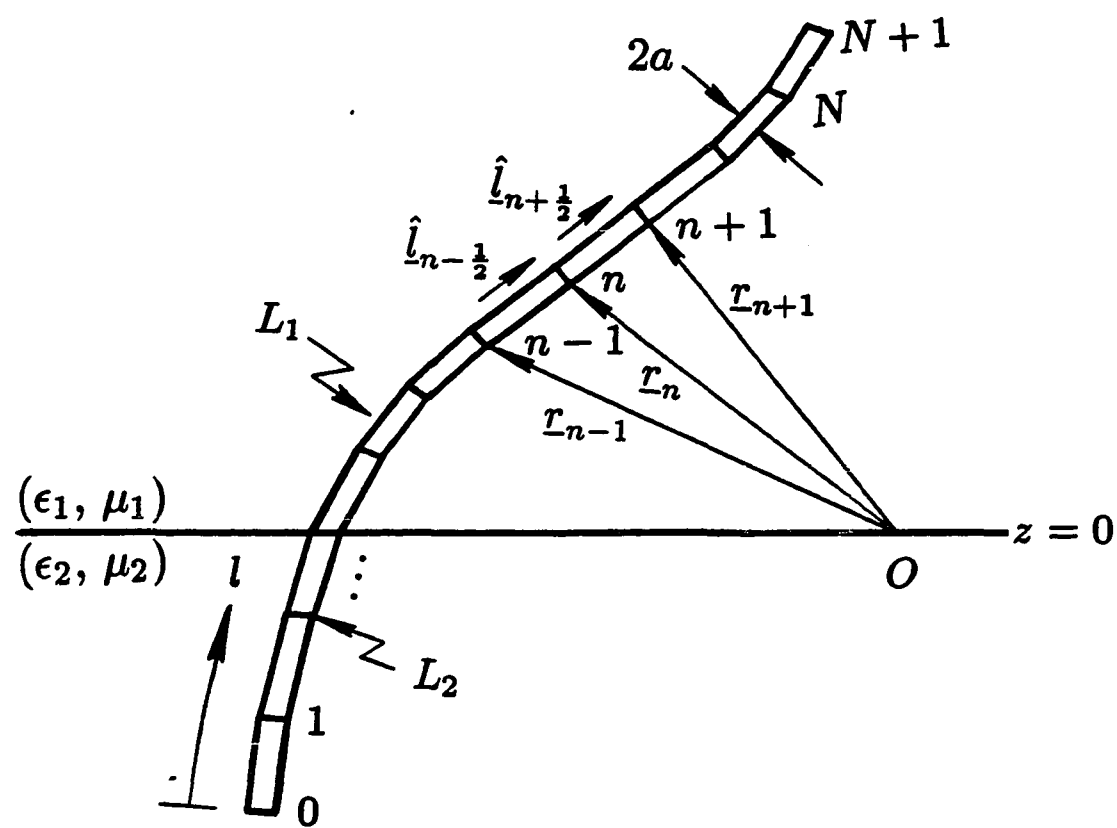


Fig. 5.5. Straight segment model of a thin-wire of arbitrary shape penetrating the interface between dissimilar media.

$$\Phi^{mi}(\underline{r}) = \Phi^{mi}(l) = \int_{L_i} K_\phi^{mi}(l | l') Q(l') dl' \quad (5-16)$$

where we have introduced the total current $\underline{I}(l) = 2\pi a \underline{J}(l)$ and the linear charge density $Q(l) = 2\pi a q(l)$. Since on the wire \underline{r} is determined by l , we have, for simplicity, replaced the former by the latter in (5-15) and (5-16). Similar remarks apply to \underline{r}' and l' . Following the MOM developed in [7], the current density along the wire is approximated as

$$\underline{I}(l) = \sum_{n=1}^N I_n \underline{\Lambda}_n(l) \quad (5-17)$$

where $\underline{\Lambda}_n(l)$ is the vector expansion function given by

$$\underline{\Lambda}_n(l) = \begin{cases} \hat{l}_{n-\frac{1}{2}} \frac{l - l_{n-1}}{l_n - l_{n-1}}, & l_{n-1} < l < l_n \\ \hat{l}_{n+\frac{1}{2}} \frac{l_{n+1} - l}{l_{n+1} - l_n}, & l_n < l < l_{n+1} \\ 0, & \text{otherwise} \end{cases} \quad (5-18)$$

The divergence of $\underline{\Lambda}_n(l)$, which is proportional to the linear charge density associated with this basis function, is

$$\nabla \cdot \underline{\Lambda}_n(l) = \begin{cases} \frac{1}{l_n - l_{n-1}}, & l_{n-1} < l < l_n \\ -\frac{1}{l_{n+1} - l_n}, & l_n < l < l_{n+1} \\ 0, & \text{otherwise} \end{cases} \quad (5-19)$$

When the expansions for \underline{I} and Q are used in (5-1) and the resulting equations tested with $\underline{\Lambda}_n(l)$, an $N \times N$ system of linear equations is obtained, which may be

written in matrix form as

$$[Z_{pn}][I_n] = [V_p] \quad (5-20)$$

where

$$Z_{pn} = j\omega \left(\frac{l_p - l_{p-1}}{2} A_{p-\frac{1}{2},n} + \frac{l_{p+1} - l_p}{2} A_{p+\frac{1}{2},n} \right) - \frac{1}{j\omega} (\Phi_{p+\frac{1}{2},n} - \Phi_{p-\frac{1}{2},n}) \quad (5-21)$$

$$V_p = \frac{l_p - l_{p-1}}{2} \hat{l}_{p-\frac{1}{2}} \cdot \underline{\underline{E}}_m^{inc}(l_{p-\frac{1}{2}}) + \frac{l_{p+1} - l_p}{2} \hat{l}_{p+\frac{1}{2}} \cdot \underline{\underline{E}}_m^{inc}(l_{p+\frac{1}{2}}) \quad (5-22)$$

in which

$$A_{p\pm\frac{1}{2},n} = \int_{L_i} \hat{l}_{p\pm\frac{1}{2}} \cdot \underline{\underline{K}}_A^{mi}(l_{p\pm\frac{1}{2}} | l') \cdot \underline{\Delta}_n(l') dl' \quad (5-23)$$

$$\Phi_{p\pm\frac{1}{2},n} = \int_{L_i} K_\phi^{mi}(l_{p\pm\frac{1}{2}} | l') \nabla \cdot \underline{\Delta}_n(l') dl' \quad (5-24)$$

and

$$l_{p\pm\frac{1}{2}} = \frac{l_p + l_{p\pm 1}}{2}. \quad (5-25)$$

In (5-23) and (5-24), we employ the exact kernel on the source segment and the reduced kernel otherwise.

It is observed that the integrand of (5-23) consists of seven terms contributed by the non-zero elements of the dyadic kernel $\underline{\underline{K}}_A^{mi}$. For example, the contribution of K_{zz}^{mi} to $A_{p-\frac{1}{2},n}$ is

$$\int_{L_i} \hat{l}_{p-\frac{1}{2}} \cdot \hat{\underline{x}} K_{zz}^{mi}(l_{p-\frac{1}{2}} | l') \hat{\underline{z}} \cdot \underline{\Delta}_n(l') dl'$$

$$\begin{aligned}
&= \hat{l}_{p-\frac{1}{2}} \cdot \hat{z} \left[\int_{l_{n-1}}^{l_n} K_{xz}^{mi}(l_{p-\frac{1}{2}} | l') \frac{l' - l_{n-1}}{l_n - l_{n-1}} dl' \hat{z} \cdot \hat{l}_{n-\frac{1}{2}} \right. \\
&\quad \left. + \int_{l_n}^{l_{n+1}} K_{xz}^{mi}(l_{p-\frac{1}{2}} | l') \frac{l_{n+1} - l'}{l_{n+1} - l_n} dl' \hat{z} \cdot \hat{l}_{n+\frac{1}{2}} \right]. \quad (5-26)
\end{aligned}$$

The integrals in (5-26) may be further transformed as

$$\begin{aligned}
&\int_{l_{n-1}}^{l_n} K_{xz}^{mi}(l_{p-\frac{1}{2}} | l') \frac{l' - l_{n-1}}{l_n - l_{n-1}} dl' \\
&= \frac{1}{2} \int_{-\Delta^-}^{\Delta^-} K_{xz}^{mi}(l_{p-\frac{1}{2}} | s' + l_{n-\frac{1}{2}}) ds' \\
&\quad + \frac{1}{l_n - l_{n-1}} \int_{-\Delta^-}^{\Delta^-} K_{xz}^{mi}(l_{p-\frac{1}{2}} | s' + l_{n-\frac{1}{2}}) s' ds' \quad (5-27)
\end{aligned}$$

and

$$\begin{aligned}
&\int_{l_n}^{l_{n+1}} K_{xz}^{mi}(l_{p-\frac{1}{2}} | l') \frac{l_{n+1} - l'}{l_{n+1} - l_n} dl' \\
&= \frac{1}{2} \int_{-\Delta^+}^{\Delta^+} K_{xz}^{mi}(l_{p-\frac{1}{2}} | s' + l_{n+\frac{1}{2}}) ds' \\
&\quad - \frac{1}{l_{n+1} - l_n} \int_{-\Delta^+}^{\Delta^+} K_{xz}^{mi}(l_{p-\frac{1}{2}} | s' + l_{n+\frac{1}{2}}) s' ds' \quad (5-28)
\end{aligned}$$

where $\Delta^\pm = |l_{n\pm 1} - l_n|/2$.

An examination of (5-21) and of the above expressions reveals that the right-hand integrals in (5-27) can be used in the matrix elements $Z_{p-1,n-1}$, $Z_{p,n-1}$, $Z_{p-1,n}$, and Z_{pn} , resulting in considerable savings in matrix fill time.

As suggested in Fig. 5.5, no straight segment is allowed to cross the interface, where the charge is discontinuous. Also, by using the same arguments as given in

Section 5.1, one can prove that no extra terms need to be added to (5-21) to account for the interface, if Formulation C is used.

5.3. Transmission Line of Arbitrary Cross-Section

The structure under consideration is shown in a cross-sectional view in Fig. 5.6. The ground plane at $z = -d$ is assumed to be perfectly conducting. The arbitrarily shaped PEC cylinder may be open (for example, infinitely thin strip) or closed (finite-thickness strip), and is of infinite extent and invariant along the y coordinate. As illustrated in Fig. 5.6, the contour of the cylinder cross-section is approximated in terms of straight line segments. The definitions for the ends of the segments, the local arc length coordinate, and the unit vectors parallel to the segments are the same as those in Section 5.2, except that in this case l and \hat{r}_n are functions of x and z only. As we want to determine the modes propagating along the conductor, we assume that all field components depend on y according to $e^{-jk_y y}$, where $k_y = \beta - j\alpha$ represents the propagation constant of the mode. For this two-dimensional problem, the surface current density on the cylinder can be decomposed as

$$\underline{J}(\underline{r}) = \underline{J}_t(\underline{r}) + \hat{y} J_y(\underline{r}) \quad (5-29)$$

where $\underline{J}_t(\underline{r})$ and $J_y(\underline{r})$ are the transverse and longitudinal surface current densities, respectively, and can be expressed as

$$\underline{J}_t(\underline{r}) = \underline{J}_t(l) e^{-jk_y y} \quad (5-30)$$

$$J_y(\underline{r}) = J_y(l) e^{-jk_y y} \quad (5-31)$$

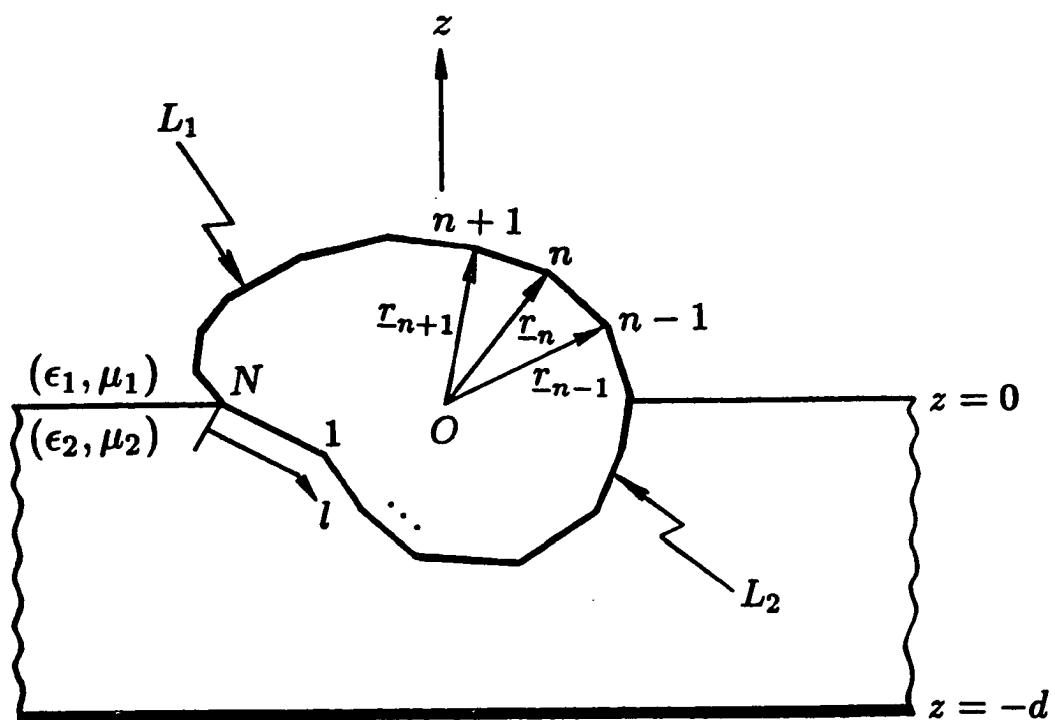


Fig. 5.6. Straight line segment model of a cylinder of arbitrary cross-section embedded in a grounded slab.

where l is the local arc length coordinate along the circumference of the conductor and is a function of the transverse position only (cf. Fig. 5.6). Thus, for the transmission line structure, (5-1) may be expressed as

$$\hat{n}_m \times \sum_{i=1}^2 [j\omega \underline{A}^{mi}(l) + (\nabla_t - \hat{y}jk_y) \Phi^{mi}(l)] = 0, \quad m = 1, 2 \quad (5-32)$$

where

$$\nabla_t = \hat{x} \frac{\partial}{\partial x} + \hat{z} \frac{\partial}{\partial z} \quad (5-33)$$

$$\underline{A}^{mi}(l) = \int_{L_i} \underline{\underline{K}}_A^{mi}(l | l') \cdot \underline{J}(l') dl' \quad (5-34)$$

$$\Phi^{mi}(l) = \int_{L_i} K_\phi^{mi}(l | l') q(l') dl'. \quad (5-35)$$

The charge density $q(l)$ in (5-35) can be obtained by using the equation of continuity,

$$q(l) = \frac{1}{-j\omega} (\nabla_t - \hat{y}jk_y) \cdot \underline{J}(l). \quad (5-36)$$

The elements of $\underline{\underline{K}}_A^{mi}$ and K_ϕ^{mi} can be obtained from (A-16)–(A-35) by making the following changes:

$$S_n[\tilde{g}(k_\rho)] \longrightarrow S_n[\tilde{g}(k_x)] = \int_{-\infty}^{\infty} \tilde{g}(k_x) e^{-j k_x (x - x')} dk_x \quad (5-37)$$

$$\cos \zeta S_1[\tilde{g}(k_\rho)] \longrightarrow S_0[j k_x \tilde{g}(k_x)] \quad (5-38)$$

$$\sin \zeta S_1[\tilde{g}(k_\rho)] \longrightarrow j k_y S_0[\tilde{g}(k_x)] \quad (5-39)$$

$$g_i(r) = \frac{e^{-jk_ir}}{r} \rightarrow \frac{\pi}{j} H_0^{(2)}(\rho\sqrt{k_i^2 - k_y^2}) \quad (5-40)$$

where $\rho = \sqrt{(x-x')^2 + (z-z')^2}$. Following the MOM procedure developed in [4] for objects in free space, the surface current densities may be approximated as

$$\underline{J}_t = \sum_{n=1}^{N^t} I_n^t \underline{\Lambda}_n(l) \quad (5-41)$$

$$J_y = \sum_{n=1}^{N^y} I_n^y \Pi_n(l) \quad (5-42)$$

where

$$\underline{\Lambda}_n(l) = \begin{cases} \hat{l}_{n-\frac{1}{2}} \frac{l - l_{n-1}}{l_n - l_{n-1}}, & l_{n-1} < l < l_n \\ \hat{l}_{n+\frac{1}{2}} \frac{l_{n+1} - l}{l_{n+1} - l_n}, & l_n < l < l_{n+1} \\ 0, & \text{otherwise} \end{cases} \quad (5-43)$$

and

$$\Pi_n(l) = \begin{cases} 1, & l_{n-1} < l < l_n \\ 0, & \text{otherwise} \end{cases} \quad (5-44)$$

Substituting (5-34) and (5-35), and using (5-41) and (5-42) in (5-32), and testing the resulting equation with $\underline{\Lambda}_n$ and with $\underline{y} \Pi_n$, one obtains the matrix equation

$$\begin{bmatrix} [Z_{pn}^{tt}] & [Z_{pn}^{ty}] \\ [Z_{pn}^{yt}] & [Z_{pn}^{yy}] \end{bmatrix} \begin{bmatrix} [I_n^t] \\ [I_n^y] \end{bmatrix} = \begin{bmatrix} 0 \\ 0 \end{bmatrix} \quad (5-45)$$

where the elements of Z_{pn} are given as

$$Z_{pn}^{tt} = j\omega \left[\frac{l_p - l_{p-1}}{4} (A_{p-\frac{1}{2}, n-\frac{1}{2}}^{tt} + A_{p-\frac{1}{2}, n+\frac{1}{2}}^{tt}) + \frac{l_{p+1} - l_p}{4} (A_{p+\frac{1}{2}, n-\frac{1}{2}}^{tt} + A_{p+\frac{1}{2}, n+\frac{1}{2}}^{tt}) \right]$$

$$-\frac{1}{j\omega} \left[\frac{1}{l_n - l_{n-1}} (\Phi_{p+\frac{1}{2}, n-\frac{1}{2}} - \Phi_{p-\frac{1}{2}, n-\frac{1}{2}}) - \frac{1}{l_{n+1} - l_n} (\Phi_{p+\frac{1}{2}, n+\frac{1}{2}} - \Phi_{p-\frac{1}{2}, n+\frac{1}{2}}) \right] \quad (5-46)$$

$$Z_{pn}^{ty} = j\omega \left(\frac{l_p - l_{p-1}}{2} A_{p-\frac{1}{2}, n-\frac{1}{2}}^{ty} + \frac{l_{p+1} - l_p}{2} A_{p+\frac{1}{2}, n-\frac{1}{2}}^{ty} \right) + \frac{k_y}{\omega} (\Phi_{p+\frac{1}{2}, n-\frac{1}{2}} - \Phi_{p-\frac{1}{2}, n-\frac{1}{2}}) \quad (5-47)$$

$$\begin{aligned} Z_{pn}^{yt} = j\omega & \frac{l_p - l_{p-1}}{2} \left(A_{p-\frac{1}{2}, n-\frac{1}{2}}^{yt} + A_{p-\frac{1}{2}, n+\frac{1}{2}}^{yt} \right) \\ & + \frac{k_y}{\omega} (l_p - l_{p-1}) \left(\frac{1}{l_n - l_{n-1}} \Phi_{p-\frac{1}{2}, n-\frac{1}{2}} - \frac{1}{l_{n+1} - l_n} \Phi_{p-\frac{1}{2}, n+\frac{1}{2}} \right) \end{aligned} \quad (5-48)$$

$$Z_{pn}^{yy} = j\omega (l_p - l_{p-1}) A_{p-\frac{1}{2}, n-\frac{1}{2}}^{yy} - j \frac{k_y^2}{\omega} (l_p - l_{p-1}) \Phi_{p-\frac{1}{2}, n-\frac{1}{2}} \quad (5-49)$$

in which

$$A_{p\pm\frac{1}{2}, n\pm\frac{1}{2}}^{\tau\eta} = \mp \int_{l_{n\pm 1}}^{l_n} \hat{\tau}_{p\pm\frac{1}{2}} \cdot \underline{K}_A^{mi}(l_{p\pm\frac{1}{2}} | l') \cdot \hat{\eta}_{n\pm\frac{1}{2}} dl', \quad \tau, \eta = t, y \quad (5-50)$$

$$\Phi_{p\pm\frac{1}{2}, n\pm\frac{1}{2}} = \mp \int_{l_{n\pm 1}}^{l_n} K_\phi^{mi}(l_{p\pm\frac{1}{2}} | l') dl'. \quad (5-51)$$

The \mp signs in front of the integrals (5-50) and (5-51) correspond to $n \pm \frac{1}{2}$.

The evaluation of the matrix elements (cf. (5-50)–(5-51)) involves double integrations in the space and spectrum domains. One notes that the order of the integrations may be changed and the integration in space domain can be done in closed form. Here, we only give the expressions for the matrix elements for the

practically most important case of a strip confined to the cover medium (region 1):

$$\int_{l_{n\pm 1}}^{l_n} K_{xz}^{11}(l_{p\pm \frac{1}{2}} | l') dl' = \frac{\mu_1}{4\pi} \left\{ I_{p\pm \frac{1}{2}, n\pm \frac{1}{2}} - S_{p\pm \frac{1}{2}, n\pm \frac{1}{2}} \left[\frac{\mu_1 k_{z2} \cot(k_{z2}d) - j\mu_2 k_{z1}}{D^h j k_{z1}} \right] \right\} \quad (5-52)$$

$$\int_{l_{n\pm 1}}^{l_n} K_{xz}^{11}(l_{p\pm \frac{1}{2}} | l') dl' = -\frac{\mu_1}{2\pi} (\mu_1 \epsilon_1 - \mu_2 \epsilon_2) S_{p\pm \frac{1}{2}, n\pm \frac{1}{2}} \left[\frac{j k_x}{D^e D^h} \right] \quad (5-53)$$

$$\int_{l_{n\pm 1}}^{l_n} K_{yz}^{11}(l_{p\pm \frac{1}{2}} | l') dl' = -\frac{\mu_1}{2\pi} (\mu_1 \epsilon_1 - \mu_2 \epsilon_2) S_{p\pm \frac{1}{2}, n\pm \frac{1}{2}} \left[\frac{j k_y}{D^e D^h} \right] \quad (5-54)$$

$$\int_{l_{n\pm 1}}^{l_n} K_{zz}^{11}(l_{p\pm \frac{1}{2}} | l') dl' = - \int_{l_{n\pm 1}}^{l_n} K_{xz}^{11}(l_{p\pm \frac{1}{2}} | l') dl' \quad (5-55)$$

$$\int_{l_{n\pm 1}}^{l_n} K_{zy}^{11}(l_{p\pm \frac{1}{2}} | l') dl' = - \int_{l_{n\pm 1}}^{l_n} K_{yz}^{11}(l_{p\pm \frac{1}{2}} | l') dl' \quad (5-56)$$

$$\begin{aligned} \int_{l_{n\pm 1}}^{l_n} K_{zz}^{11}(l_{p\pm \frac{1}{2}} | l') dl' &= \frac{\mu_1}{4\pi} \left\{ I_{p\pm \frac{1}{2}, n\pm \frac{1}{2}} + S_{p\pm \frac{1}{2}, n\pm \frac{1}{2}} \left[\frac{\epsilon_1 k_{z2} \tan(k_{z2}d) + j\epsilon_2 k_{z1}}{D^e j k_{z1}} \right] \right. \\ &\quad \left. + 2(\mu_2 \epsilon_2 - \mu_1 \epsilon_1) S_{p\pm \frac{1}{2}, n\pm \frac{1}{2}} \left[\frac{j k_{z1}}{D^e D^h} \right] \right\} \end{aligned} \quad (5-57)$$

$$\begin{aligned} \int_{l_{n\pm 1}}^{l_n} K_\phi^{11}(l_{p\pm \frac{1}{2}} | l') dl' &= \frac{1}{4\pi \epsilon_1} \left\{ I_{p\pm \frac{1}{2}, n\pm \frac{1}{2}} - S_{p\pm \frac{1}{2}, n\pm \frac{1}{2}} \left[\frac{\mu_1 k_{z2} \cot(k_{z2}d) - j\mu_2 k_{z1}}{D^h j k_{z1}} \right] \right. \\ &\quad \left. + 2(\mu_2 \epsilon_2 - \mu_1 \epsilon_1) S_{p\pm \frac{1}{2}, n\pm \frac{1}{2}} \left[\frac{j k_{z1}}{D^e D^h} \right] \right\} \end{aligned} \quad (5-58)$$

where we have introduced the notations

$$I_{p\pm\frac{1}{2},n\pm\frac{1}{2}} = \mp \frac{\pi}{j} \int_{-\Delta^\pm}^{\Delta^\pm} H_0^{(2)}(\rho \sqrt{k_1^2 - k_y^2}) dl', \quad (5-59)$$

$$S_{p\pm\frac{1}{2},n\pm\frac{1}{2}}[\tilde{f}(k_x)] = \mp 2 \int_{-\infty}^{\infty} \tilde{f}(k_x) e^{-jk_{z1}(z_{p\pm\frac{1}{2}}+z_{n\pm\frac{1}{2}})} e^{-jk_x(x_{p\pm\frac{1}{2}}-x_{n\pm\frac{1}{2}})} \cdot \frac{\sin[(k_{z1}D_{n\pm\frac{1}{2}}^z - k_x D_{n\pm\frac{1}{2}}^x)\Delta^\pm]}{k_{z1}D_{n\pm\frac{1}{2}}^z - k_x D_{n\pm\frac{1}{2}}^x} dk_x \quad (5-60)$$

in which

$$\rho = [(x_{p\pm\frac{1}{2}} - x_{n\pm\frac{1}{2}} - D_{n\pm\frac{1}{2}}^x l')^2 + (z_{p\pm\frac{1}{2}} - z_{n\pm\frac{1}{2}} - D_{n\pm\frac{1}{2}}^z l')^2]^{\frac{1}{2}} \quad (5-61)$$

$$D_{n\pm\frac{1}{2}}^x = \hat{l}_{n\pm\frac{1}{2}} \cdot \hat{x}, \quad D_{n\pm\frac{1}{2}}^z = \hat{l}_{n\pm\frac{1}{2}} \cdot \hat{z} \quad (5-62)$$

and

$$\Delta^\pm = \frac{|l_n - l_{n\pm 1}|}{2}. \quad (5-63)$$

The \mp signs in front of integrals (5-59) and (5-60) correspond to $n \pm \frac{1}{2}$. Substituting (5-52) through (5-57) into (5-50), and (5-58) into (5-51), one obtains the matrix elements for the case of a strip confined to the cover region. In a manner similar to that mentioned in Section 5.2, the integrals in (5-50) and (5-51) may be reused for different matrix elements.

The homogeneous system (5-45) has non-trivial solutions for those values of k_y , which render its determinant vanish. Hence, to obtain the propagation constants of the various modes of the microstrip, a search is performed for the zeroes of the der-

inant in the complex k_y -plane. For each propagation constant, the homogeneous system (5-45) is solved for the corresponding modal current distribution.

CHAPTER 6

NUMERICAL EVALUATION OF SOMMERFELD INTEGRALS

The dyadic and scalar kernels in the mixed-potential EFIE comprise Sommerfeld integrals $S_n(\tilde{f})$ defined in (3-3). When solving the integral equation by the method of moments as discussed in the previous chapter, these integrals must be numerically evaluated for wide ranges of variation in media parameters, frequency, and spatial variables. Several numerical algorithms are developed in this chapter. They are based on deformation of the integration path off the real axis into the complex k_ρ plane. We first discuss the integrals which arise in the contiguous half-space problem and then the integrals pertaining to the transmission line problem.

6.1. Sommerfeld Integrals for the Half-Space Problem

The Sommerfeld integrals encountered in this work can be expressed as (cf. (3-3))

$$S_n[\tilde{f}(k_\rho)] = \int_0^\infty \tilde{f}(k_\rho) J_n(\xi k_\rho) k_\rho^{n+1} dk_\rho. \quad (6-1)$$

For the half-space problem, the integrand in (6-1) is given as

$$\tilde{f}(k_\rho) = \frac{N(k_1, k_2; k_\rho)}{D(k_1, k_2; k_\rho)} \begin{cases} e^{-jk_{z1}|z+z'|}, & m = i \\ e^{-j(k_{zm}|z| + k_{zi}|z'|)}, & m \neq i \end{cases} \quad (6-2)$$

where the functions N and D can assume different forms (cf. Appendix A.1), and

where

$$k_{zi} = \sqrt{k_i^2 - k_\rho^2}, \quad i = 1, 2. \quad (6-3)$$

The function k_{zi} has branch points at $k_\rho = \pm k_i$. For analytic convenience, we will assume that the media are lossy; that is, $k_i = k'_i - jk''_i$, where both k'_i and k''_i are positive numbers. We can consider a lossless medium to be the limit of a lossy medium as the dissipation goes to zero ($k''_i \rightarrow 0$). We also assume, for convenience and without loss of generality, that $k'_2 > k'_1$ and $k''_2 > k''_1$. To specify k_{zi} uniquely, we may view the complex $k_\rho = \zeta' + j\zeta''$ plane as a two-sheeted Riemann surface with the sheets connected along the branch cuts. On this surface, k_{zi} is a single-valued analytic function of k_ρ . The choice of the branch cuts in the complex k_ρ -plane is rather arbitrary, although a particular choice may be convenient for a specific problem. In this work, we exclusively use the branch cuts specified by the requirement that $\text{Im}(k_{zi}) < 0$ everywhere on one sheet, referred to as the top or proper sheet. The other sheet, on which $\text{Im}(k_{zi}) > 0$, is then referred to as the bottom, or improper sheet. This definition implies that the two sheets are joined together by the curve defined by $\text{Im}(k_{zi}) = 0$, which therefore locates the desired branch cut. Let us first write [42]

$$k_{zi}^2 = |k_{zi}|^2 e^{j\theta} = k_i^2 - k_\rho^2, \quad -2\pi < \theta < 2\pi \quad (6-4)$$

whence

$$k_{zi} = |k_{zi}| e^{j\theta/2}. \quad (6-5)$$

It is clear that if $\text{Im}(k_{zi}) < 0$, $-\pi < \theta/2 < 0$, and if $\text{Im}(k_{zi}) > 0$, $0 < \theta/2 < \pi$.

This suggests that we define a two-sheeted k_{zi}^2 -plane, where $-2\pi < \theta < 0$ on the top sheet and $0 < \theta < 2\pi$ on the bottom sheet, as shown in Fig. 6.1. These sheets are joined along the positive real axis, where

$$\operatorname{Im}(k_{zi}^2) = 0 \quad \text{and} \quad \operatorname{Re}(k_{zi}^2) \geq 0. \quad (6-6)$$

For later convenience, we also show the regions where $\operatorname{Re}(k_{zi}) > 0$ and $\operatorname{Re}(k_{zi}) < 0$ in the entire two-sheeted k_{zi}^2 -plane in Fig. 6.1. We now map the two-sheeted k_{zi}^2 -plane into a two-sheeted k_ρ^2 -plane by means of (6-5). The result is shown in Fig. 6.2, where we have introduced the notation

$$k_i^2 = (k_i'^2 - k_i''^2) - j2k_i'k_i'' \equiv \tau + j\Omega \quad (6-7)$$

It follows from (6-4) and (6-7) that the branch cuts in the k_ρ^2 -plane are defined by

$$\operatorname{Re}(k_\rho^2) \leq \tau \quad \text{and} \quad \operatorname{Im}(k_\rho^2) = \Omega. \quad (6-8)$$

Finally, the two-sheeted complex k_ρ^2 -plane is mapped into a two-sheeted k_ρ -plane. Noting that $k_\rho^2 = \zeta'^2 - \zeta''^2 + j2\zeta'\zeta''$, we conclude from (6-8) that the branch cuts in the k_ρ -plane are specified by

$$\zeta'^2 - \zeta''^2 < \tau, \quad \text{and} \quad 2\zeta'\zeta'' = \Omega. \quad (6-9)$$

This mapping is illustrated in Fig. 6.3.

So far, we have only considered a single square root function k_{zi} . However, the integrand of (6-1) depends on both k_{z1} and k_{z2} . Therefore, to make it single-valued, we must introduce two pairs of branch cuts in the k_ρ -plane, defined by $\operatorname{Im}(k_{z1}) = 0$ and $\operatorname{Im}(k_{z2}) = 0$, respectively (Fig. 6.4a). We may now view the k_ρ -plane as a four-

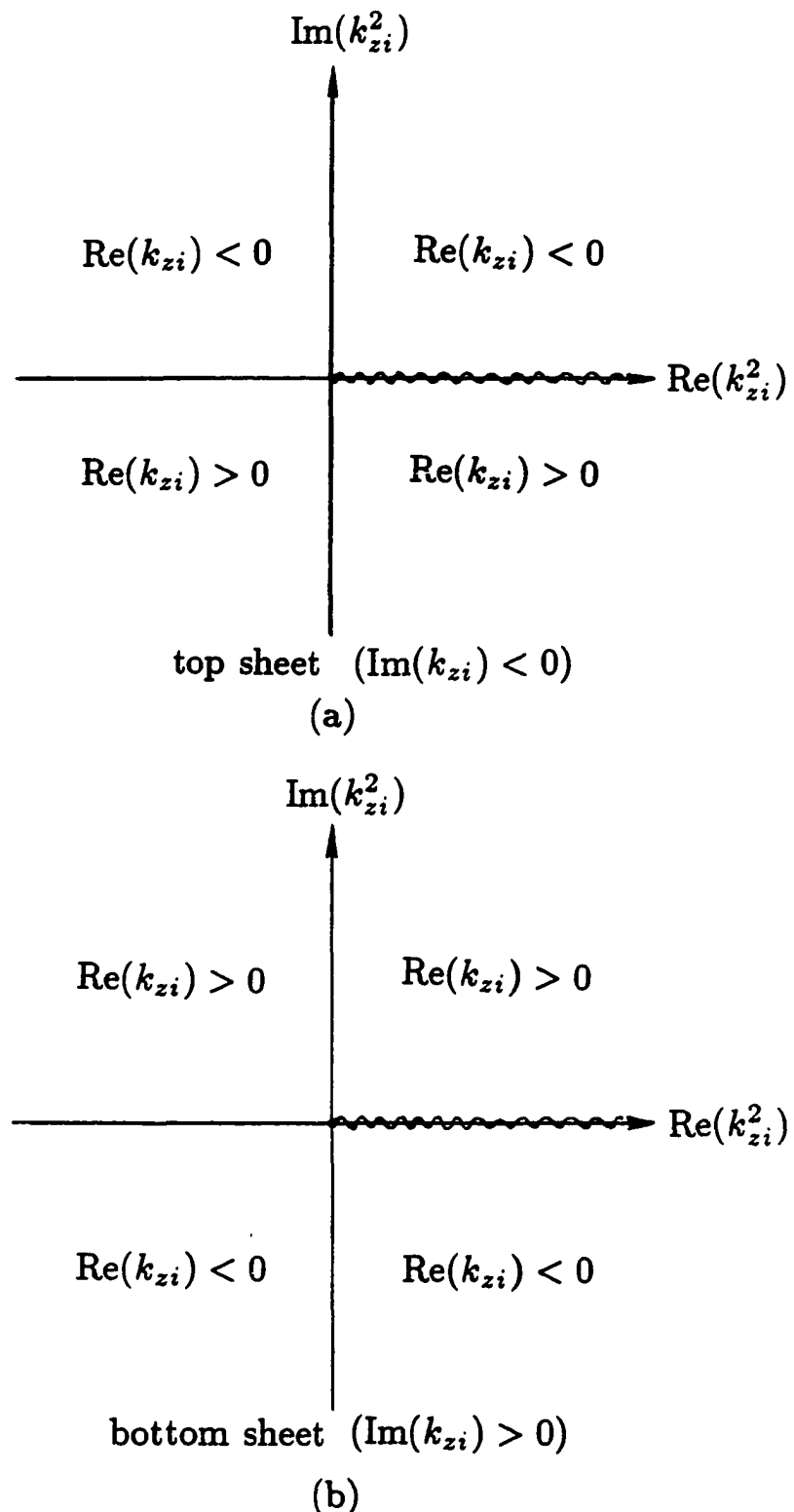


Fig. 6.1. Two sheets of the k_{zi}^2 -plane. (a) Top sheet ($\text{Im}(k_{zi}) < 0$) and (b) bottom sheet ($\text{Im}(k_{zi}) > 0$).

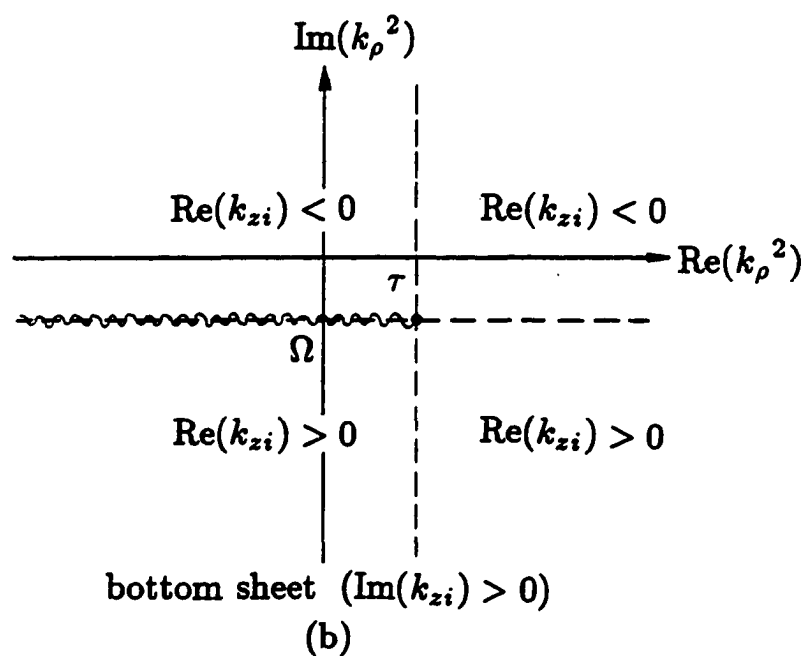
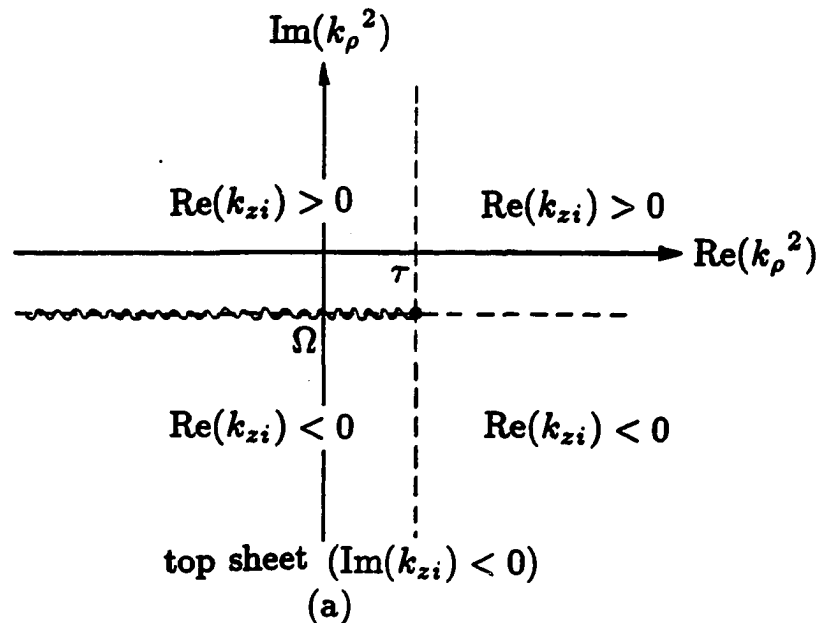


Fig. 6.2. Two sheets of k_ρ^2 -plane. (a) Top sheet ($\text{Im}(k_{zi}) < 0$) and (b) bottom sheet ($\text{Im}(k_{zi}) > 0$).

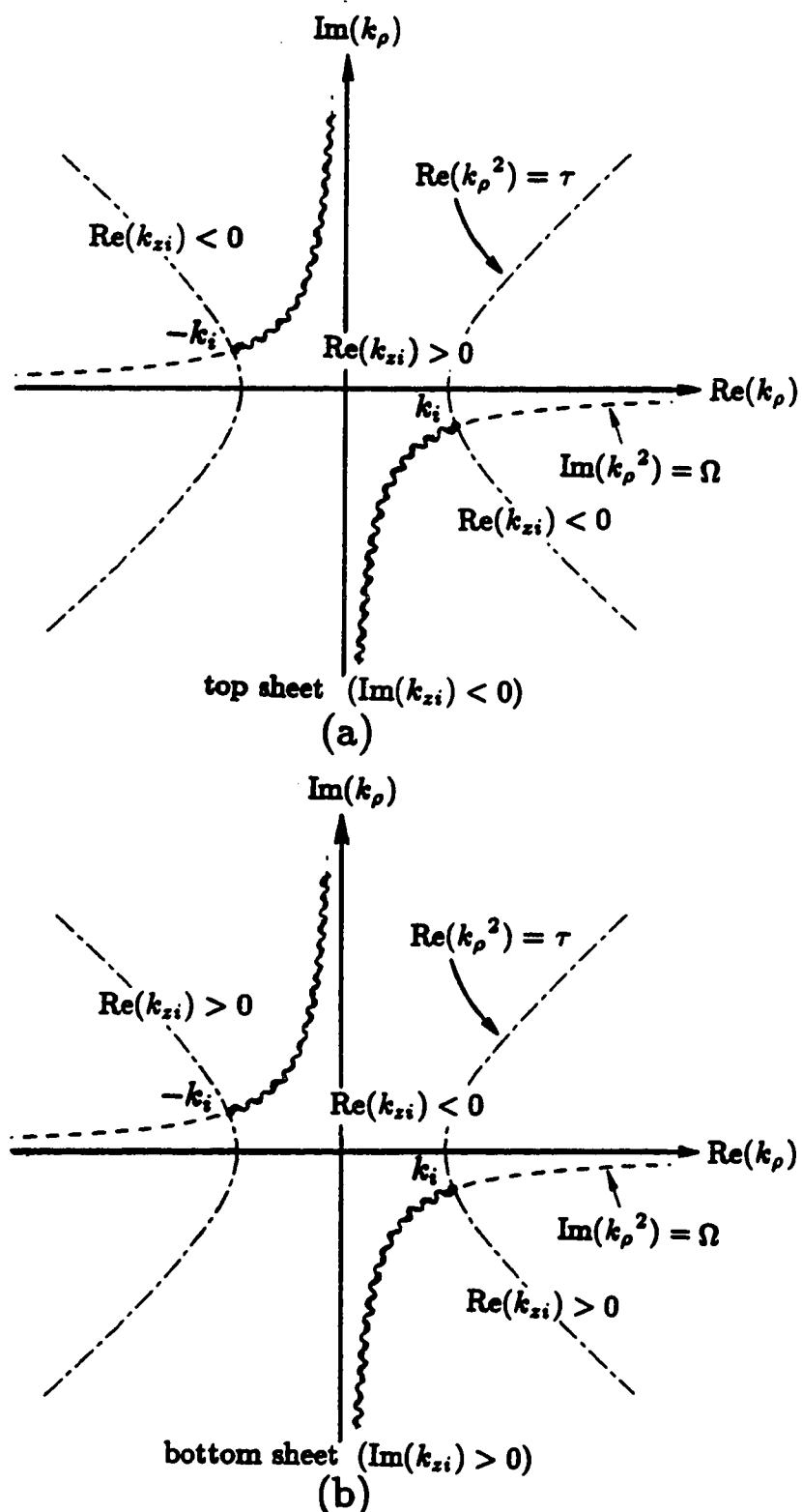


Fig. 6.3. The two-sheeted k_ρ -plane. (a) Top sheet ($\text{Im}(k_{zi}) < 0$) and (b) bottom sheet ($\text{Im}(k_{zi}) > 0$).

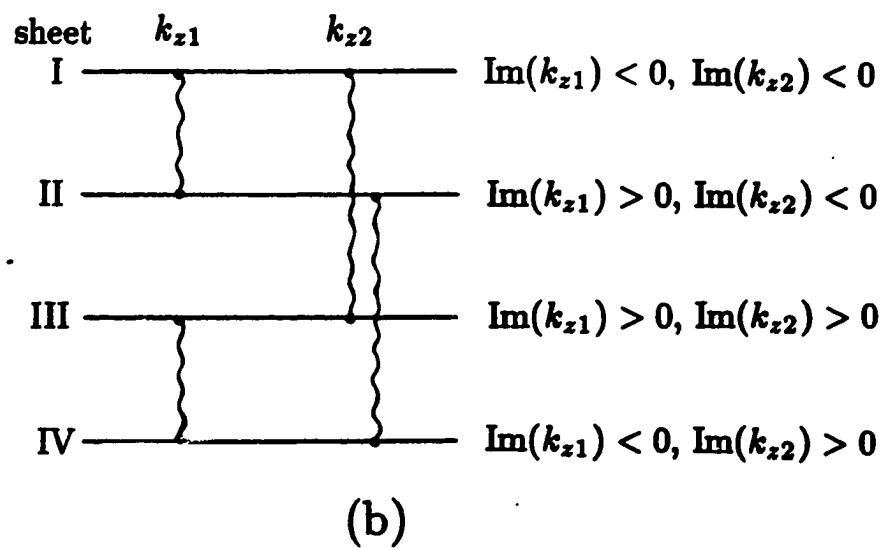
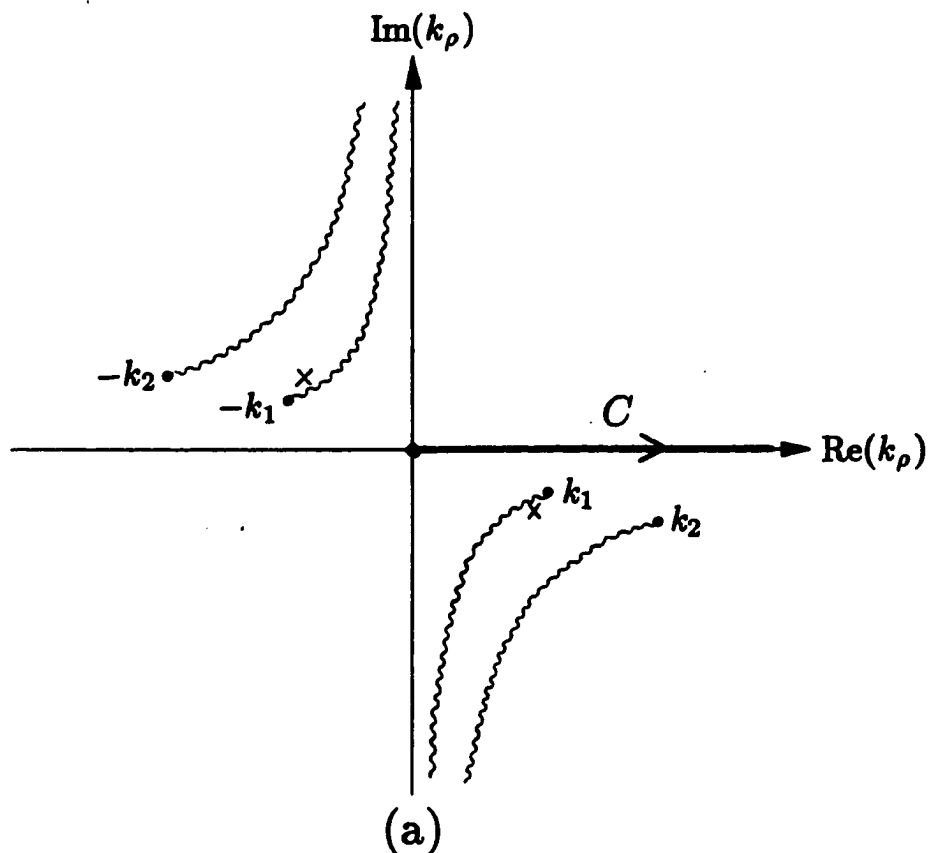


Fig. 6.4. (a) The k_ρ -plane showing the branch cuts for k_{z1} and k_{z2} . (b) The Riemann surface of four sheets in the k_ρ -plane.

sheeted Riemann surface, as illustrated schematically in Fig. 6.4b [32]. Observe that everywhere on Sheet I, $\text{Im}(k_{z1}) < 0$ and $\text{Im}(k_{z2}) < 0$.

In addition to the branch point discussed above, the integrand of (6-1) may exhibit a pair of first order poles at the zeroes of the denominator function

$$D(k_1, k_2; k_\rho) = \epsilon_1 k_{z2} + \epsilon_2 k_{z1} \quad (6-10)$$

which are given by

$$k_{\rho p} = \pm \sqrt{\frac{k_1^2 k_2^2}{k_1^2 + k_2^2}}. \quad (6-11)$$

These poles only exist on Sheets I and IV. Their location is indicated in Fig. 6.4a, which represents Sheet I of the Riemann surface.

In view of the above discussion it should be clear that to ensure the convergence of the integral (6-1), the integration path should be selected on Sheet I, as illustrated in Fig. 6.4a.

Numerical evaluation of the Sommerfeld integrals (6-1) is difficult because of the oscillatory behavior of the integrand and its rapid variation near the singularities (branch points and poles). Various numerical integration techniques have been developed to carry out these integrals. The real-axis path has been used in related problems by Siegel and King [43], Kuo and Mei [44], Lin and Mei [45], Katehi and Alexopoulos [46], Johnson and Dudley [47], and Mosig and Gardiol [17,48]. The techniques of deforming the integration path to a contour off the real axis to avoid the singularities and to accelerate convergence of the integrals have been developed by Miller *et al.* [49], Sarkar [50], Burke *et al.* [51], Michalski [24] and Michalski and Butler [52]. The method of deforming the integration path from the real axis to

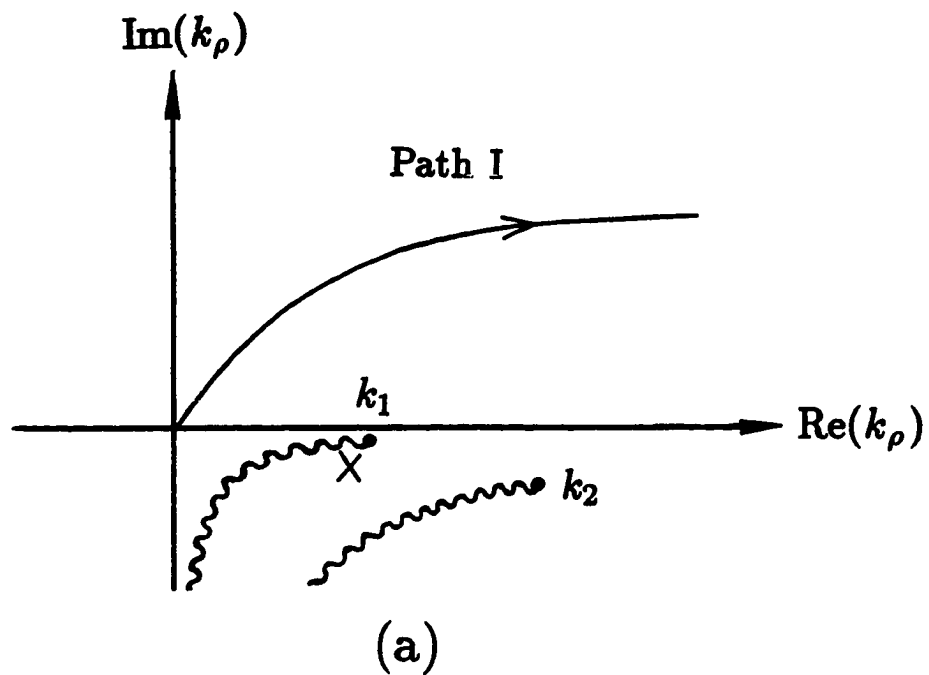
vertical branch cuts has been used by Fuller and Wait [53], and Kong *et al.* [54]. Also, several approximate approaches have been used by Hansen [55], and by Mosig and Gardiol [48]. The steepest descent path (SDP) is, of course, the most efficient one to use [24]. However, since a closed form expression for the SDP is not available when \underline{r} and \underline{r}' are in different layers, we employ in this work, as a compromise, four suboptimal paths, which are chosen depending on the relative values of $\xi = |\rho - \rho'|$ and $h = |z| + |z'|$, and on the parameters of the media. The necessity to evaluate the Bessel function of complex arguments on these paths does not significantly affect the efficiency of our approach, since it has been demonstrated by Grun and Rahmat-Samii [56] that the polynomial approximations of Bessel functions given in [57] can be analytically continued into the complex plane. Since the paths employed, or similar, have been previously described in the literature, we only summarize them below.

Path I

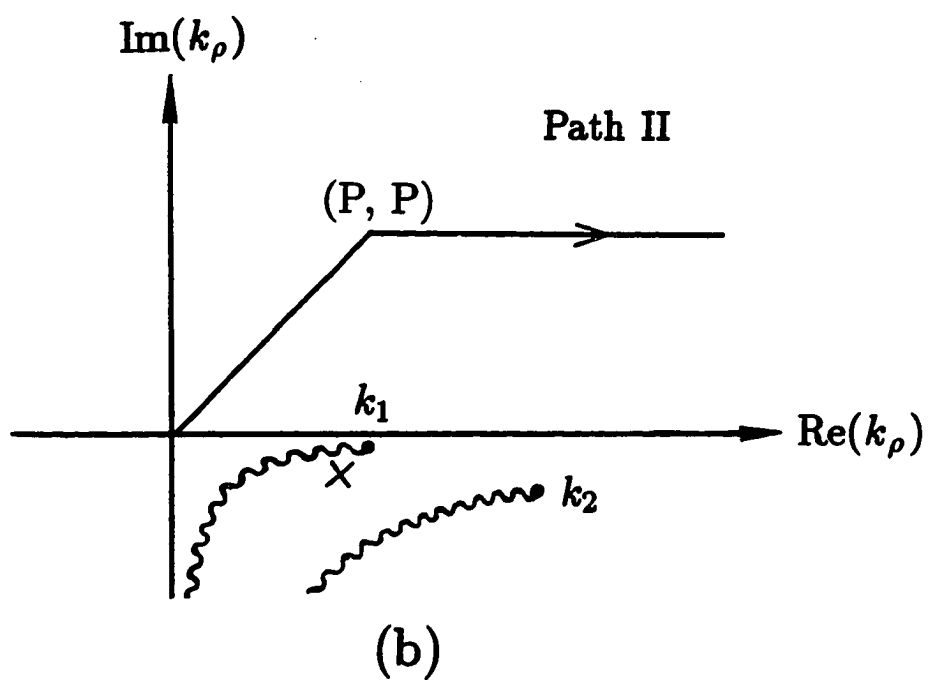
The integration path developed by Michalski and Butler [52] is illustrated in Fig. 6.5a. This path avoids the real-axis singularities and is the SDP for the exponential function part of the integrand (but not for the whole integrand). Hence, on this path the exponential function decreases monotonically, because the imaginary part of the exponent is by definition constant on the SDP. When the source and observation points are in the same layer i for $i = 1, 2$, one can use

$$k_\rho = sk_0\sqrt{2jn_i + s^2}, \quad 0 \leq s < \infty \quad (6-12)$$

where s is a real variable, $n_i = \sqrt{\epsilon_i}$ and $\text{Re}\sqrt{\cdot} > 0$. If $i \neq m$, i.e., the source and



(a)



(b)

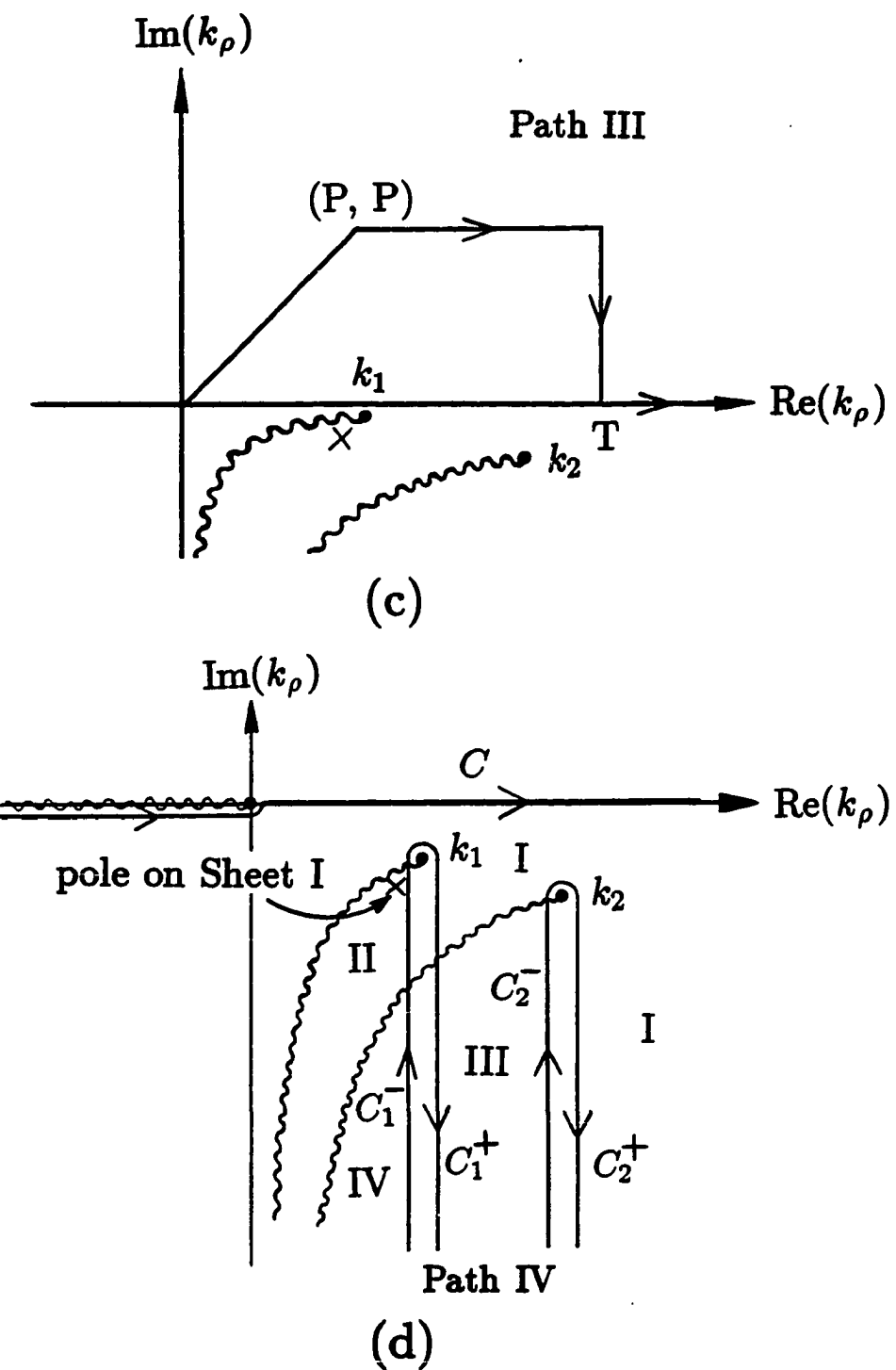


Fig. 6.5. Various integration paths of (a) Path I, (b) Path II, (c) Path III and (d) Path IV in the complex k_ρ -plane.

field points are in different layers, we choose

$$k_\rho = k_0 \sqrt{\frac{-2C}{B + \sqrt{B^2 - 4AC}}}, \quad 0 \leq s < \infty \quad (6-13)$$

where s is the real variable, $\text{Re}\sqrt{\cdot} > 0$ branch of the external root and $\text{Im}\sqrt{\cdot} < 0$ branch of the internal root should be selected. The parameters in (6-13) are

$$A = (z'^2 - z^2)^2 \quad (6-14)$$

$$B = 4|z'z|de - 2s(z'^2 + z^2) \quad (6-15)$$

$$C = s^2 - 4sn_i n_m |z'z| \quad (6-16)$$

with

$$d = n_i |z'| + n_m |z| \quad (6-17)$$

$$e = n_i |z| + n_m |z'|. \quad (6-18)$$

Since the oscillations due to the Bessel function are still present, this path selection is most efficient when $h = |z'| + |z| > \xi$. Also, the exponential growth of the Bessel function away from the real axis limits how far the path can veer off into the complex plane, which restricts the applicability of this method. In the case $m = i$, this method is applicable provided ξ is electrically small in the medium

$$k_0 \xi < \frac{1}{n'_i} \quad (6-19)$$

when $m \neq i$, one must restrict that

$$k_0 \xi < \frac{|z'| + |z|}{n'_i |z'| + n'_m |z|}. \quad (6-20)$$

When we numerically evaluate the integral (6-1) along the path, the Gauss-Legendre quadrature integration technique is employed to carry out the integrations between the two zeroes of the Bessel function which are approximated for the contour away from the real axis. When each of three consecutive intervals contributes less than 10^{-4} of the accumulated sum, the semi-infinite integration is terminated and is said to converge.

Path II

An alternate path [51], which initially strays from the real axis to avoid the branch points at k_1 and k_2 , then continues parallel to the real axis, as shown in Fig. 6.5b, has been used to overcome the limitations (6-19) and (6-20) in using Path I. The parameter P is chosen according to

$$P = \begin{cases} \frac{1}{\xi}, & h < \xi \\ \frac{1}{h}, & h > \xi \end{cases} . \quad (6-21)$$

On this path, the dominant factor for convergence is still the exponential function. The choice of parameter P restricts the contour to small $\xi \operatorname{Im}(k_p)$. Therefore, this path accelerates the convergence of the exponential function (even though it is not the SDP) and limits the divergence of the Bessel function. On this path we employ the same numerical integration technique as that used on Path I.

Path III

When $\xi \gg h$, especially when $h = 0$, Paths I and II are not efficient, since there

may be many oscillations of the Bessel function before convergence. Therefore, we introduce Path III, which initially strays from the real axis to avoid the singularities, then returns at $k_\rho = T$ to the real axis. The point T is chosen as $T = k_0(n_2 + 1)$ (recall that we assume $k'_2 > k'_1$). On the first part we employ the same numerical integration technique as that used on Path I. On the real axis ($k_\rho > T$) we employ the method of averages [17,48,58], which is summarized below.

Let us consider the integral

$$I = \int_T^\infty f(k_\rho) J_n(\xi k_\rho) k_\rho^{n+1} dk_\rho \quad (6-22)$$

where $f(k_\rho)$ is a continuous function, and $J_n(\xi k_\rho)$ has successive zeroes, k_{ρ_m} , superior to the integration boundary T . From the method of averages [17,48], one can obtain

$$I \approx I_1^M = 2^{1-M} \sum_{m=1}^M \binom{M-1}{m-1} I_m^1 \quad (6-23)$$

where

$$I_m^1 = \int_T^{k_{\rho_m}} f(k_\rho) J_n(\xi k_\rho) k_\rho^{n+1} dk_\rho, \quad m = 1, 2, \dots, M. \quad (6-24)$$

The choice of M in (6-23) depends on the requirement of the accuracy in the problem. In this work, we choose $M = 5$. The method of averages is especially suitable when the observation and source points are on the interface. We find that one still can obtain the accurate result of Sommerfeld integrals by using this method when the observation and source points are off the interface provided $\xi \gg h$.

Path IV

Integration along Path III becomes inefficient when ξ becomes large, since there may be many oscillations of the Bessel function between 0 and T . In this case, it is

useful to deform the integration path to two vertical paths, as shown in Fig. 6.5d. For this purpose, by using the relation

$$2J_n(x) = H_n^{(2)}(x) + (-1)^{n+1}H_n^{(2)}(-x) \quad (6-25)$$

where $H_n^{(2)}$ is the Hankel function of the second type of order n , one can express (6-1) in an alternate form as

$$S_n(\tilde{f}) = \frac{1}{2} \int_{-\infty}^{\infty} \tilde{f}(k_{z1}, k_{z2}; k_\rho) Q_n(\xi k_\rho) k_\rho^{n+1} e^{-j\xi k_\rho} dk_\rho \quad (6-26)$$

where we have introduced

$$Q_n(\xi k_\rho) = H_n^{(2)}(\xi k_\rho) e^{j\xi k_\rho} \quad (6-27)$$

which has the asymptotic form for large argument as [57]

$$Q_n(\xi k_\rho) \sim \sqrt{2/(\pi \xi k_\rho)} e^{j(\frac{1}{2}n + \frac{1}{4})\pi}. \quad (6-28)$$

It is noted the transformation (6-25) has introduced a branch point singularity at $k_\rho = 0$ and the associated branch cut on the negative real axis (Fig. 6.5d). Hence, the integral (6-26) should be taken in the Cauchy Principal Value (CPV) sense for $n \geq 1$. As a result, (6-26) becomes

$$S_n(\tilde{f}) = \int_C g(k_\rho) dk_\rho - j\pi \text{Res}\{g(0)\} \quad (6-29)$$

where the integration path C is illustrated in Fig. 6.5d. In (6-29),

$$g(k_\rho) = \frac{1}{2} \tilde{f}(k_\rho) Q_n(\xi k_\rho) k_\rho^{n+1} e^{-j\xi k_\rho} \quad (6-30)$$

and $\text{Res}\{g(0)\}$ is the residue of the integrand at $k_\rho = 0$. In the following analysis,

for notational simplicity, we will refer to the integral along Path C in Fig. 6.5d as the original path of integration.

We observe that when $\text{Im}(k_\rho)$ becomes negative, the integrand in (6-26) decays exponentially. It is clear that, for large values of ξ , one should deform the integration path into the vertical paths [53,54] as illustrated in Fig. 6.5d. The integral (6-26), in this case, can be written as

$$S_n = S_n^{(1)} + S_n^{(2)} \quad (6-31)$$

where $S_n^{(1)}$ and $S_n^{(2)}$ are the integrals along the two vertical paths emanating from k_1 and k_2 , respectively, as shown in Fig. 6.5d. By examining Figs. 6.3 and 6.4b, that the integration path C_1 starts on Sheet IV where $\text{Re}(k_{z1}, k_{z2}) \geq 0$ and proceeds upward along the vertical; it leaves Sheet IV when it crosses the k_{z2} branch cut, and enters a region of Sheet II where $\text{Re}(k_{z1}, k_{z2}) \geq 0$; it then reaches Sheet I when it crosses the k_{z1} branch cut, where $\text{Re}(k_{z1}) \leq 0$ and $\text{Re}(k_{z2}) \geq 0$; it turns around the branch point at k_1 and goes down along the vertical; finally it leaves Sheet I when it crosses the k_{z2} branch cut, and enters a region of Sheet III where $\text{Re}(k_{z1}) \leq 0$ and $\text{Re}(k_{z2}) \geq 0$. In a similar manner, integration path C_2 starts on Sheet III, proceeds upward along the vertical from Sheet III to Sheet I and reaches the branch point at k_2 . On this part of C_2 , $\text{Re}(k_{z1}) \leq 0$ and $\text{Re}(k_{z2}) \geq 0$. The integration path C_2 finally emanates from k_2 and proceeds down along the vertical on Sheet I where $\text{Re}(k_{z1}, k_{z2}) \leq 0$. From the above analysis, one can determine the branches of the square root functions k_{z1} and k_{z2} along the vertical paths as follows:

$$\begin{aligned}
 \operatorname{Re}(k_{z1}, k_{z2}) &> 0, & \text{on } C_1^- \\
 \operatorname{Re}(k_{z1}) &< 0, \operatorname{Re}(k_{z2}) > 0, & \text{on } C_1^+ \text{ and } C_2^- \\
 \operatorname{Re}(k_{z1}, k_{z2}) &< 0, & \text{on } C_2^+.
 \end{aligned} \tag{6-32}$$

If we use the variable transformations

$$k_\rho = k_1 - jk_0 s^2, \quad 0 \leq s < \infty, \quad \text{on } C_1 \tag{6-33}$$

$$k_\rho = k_2 - jk_0 s^2, \quad 0 \leq s < \infty, \quad \text{on } C_2 \tag{6-34}$$

we obtain the following forms by invoking (6-32)

$$\begin{aligned}
 S_n^{(1)} &= \frac{e^{-jk_1\xi}}{2} \int_0^\infty [\tilde{f}(-k_{z1}, k_{z2}; k_\rho) - \tilde{f}(-k_{z1}, k_{z2}; k_\rho)] \\
 &\quad \cdot Q_n(\xi k_\rho) k_\rho^{n+1} \Big| (-2jk_0 s) e^{-k_0 \xi s^2} ds \\
 k_\rho &= k_1 - jk_0 s^2
 \end{aligned} \tag{6-35}$$

and

$$\begin{aligned}
 S_n^{(2)} &= \frac{e^{-jk_2\xi}}{2} \int_0^\infty [\tilde{f}(-k_{z1}, -k_{z2}; k_\rho) - \tilde{f}(-k_{z1}, k_{z2}; k_\rho)] \\
 &\quad \cdot Q_n(\xi k_\rho) k_\rho^{n+1} \Big| (-2jk_0 s) e^{-k_0 \xi s^2} ds \\
 k_\rho &= k_2 - jk_0 s^2
 \end{aligned} \tag{6-36}$$

where it is assumed that $\operatorname{Re}(k_{z1}, k_{z2}) \geq 0$. The proximity of the pole at $k_{\rho\rho}$ on Sheet I to the integration path C_1 makes the integrand vary rapidly near $s = 0$. To remedy this difficulty, a pole subtraction technique is employed [59]. Thus, the

integral (6-35) is expressed as

$$S_n^{(1)} = \frac{e^{-jk_1\xi}}{2} \left\{ \left(\int_0^\infty [\tilde{f}(-k_{z1}, k_{z2}; k_\rho) - f(k_{z1}, k_{z2}; k_\rho)] Q_n(\xi k_\rho) k_\rho^{n+1} \Big| (-2jk_0 s) \right. \right. \\ \left. \left. k_\rho = k_0(n_1 - js^2) \right. \right. \\ \left. \left. - \frac{2R_p s_p}{s^2 - s_p^2} \right) e^{-k_0 \xi s^2} ds + j\pi R_p W\left(\sqrt{k_0 \xi} s_p\right) \right\} \quad (6-37)$$

where R_p is the Residue of $\tilde{f}(k_{z1}, k_{z2}; k_\rho) Q_n(\xi k_\rho) k_\rho^{n+1}$ at $k_\rho = k_{pp}$, s_p is the pole position in the s -plane, and $W(z) = e^{-z^2} \operatorname{erfc}(-jz)$ is the Error function [57].

A “rule-of-thumb” has been developed for determining the best path of integration. The guide chart is given in Fig. 6.6. These guidelines have been established from the various reasons given previously and from our computational experience.

6.2. Sommerfeld Integrals for the Transmission Line Problem

In this section, to simplify the discussion, we only consider the case where the infinite conductor is confined to the cover medium (region 1). A typical integral that arises in this context is given in (5-60). This integral can be expressed in terms of the integrals of the form

$$I = \int_0^\infty \frac{N(k_{z1}, k_{z2}, k_x)}{D^e D^h} e^{-jk_{z1}(z-z')} \begin{Bmatrix} \cos[k_x(x-x')] \\ \sin[k_x(x-x')] \end{Bmatrix} dk_x \quad (6-38)$$

where the cosine or sine functions arise depending on whether the numerator functions N are even or odd in k_x . The denominator functions D^e and D^h are given in (A-36) and (A-37), respectively, and

$$k_{zi} = \sqrt{k_i^2 - k_x^2 - k_y^2}, \quad i = 1, 2. \quad (6-39)$$

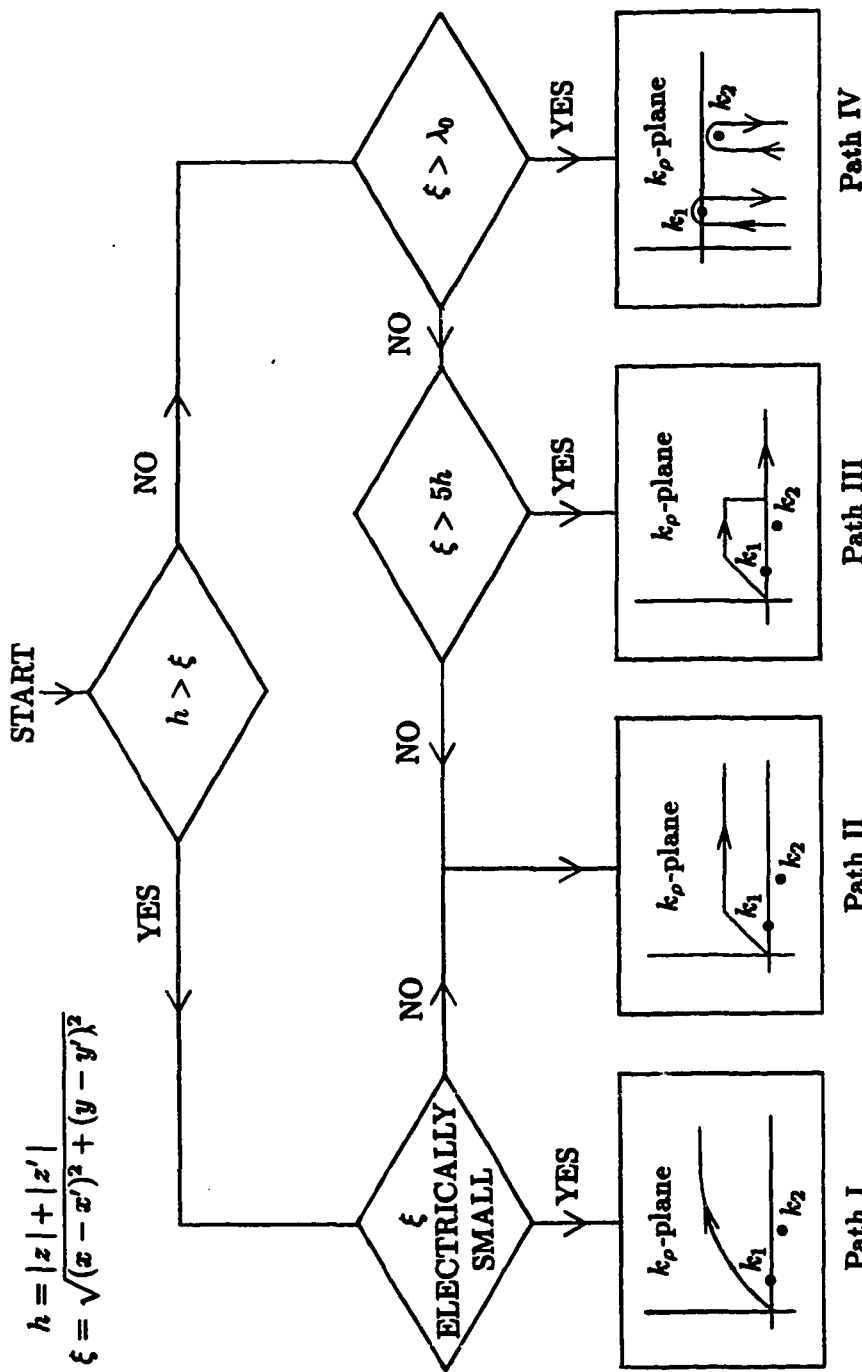


Fig. 6.6. Schematic view of the selection of integration paths.

The propagation constant will be expressed as

$$k_y = \beta - j\alpha \quad (6-40)$$

where β is the phase constant and α is the attenuation constant. It will be assumed that $\alpha \geq 0$ and $\beta > 0$.

It can be shown that the integrand of (6-38) is an even function of k_{z2} . Therefore, unlike in the half-space problem, only one pair of branch points, associated with k_{z1} , arise in the present case. These branch points and the associated branch cuts, selected by the criteria given in Section 6.1, define a k_x -plane as a two-sheeted Riemann surface. As before, $\text{Im}(k_{z1}) < 0$ on the top sheet and the opposite holds on the bottom sheet. Since the value of k_y will be specified on each iteration of the search procedure, we express k_{z1} as

$$k_{z1} = \sqrt{\kappa^2 - k_x^2} \quad (6-41)$$

where we have defined

$$\begin{aligned} \kappa^2 &= k_1^2 - k_y^2 = (k_1^2 - \beta^2 + \alpha^2) + j2\alpha\beta \\ &= \tau + j\Omega. \end{aligned} \quad (6-42)$$

We assume, for simplicity, that the media are lossless. Consequently, k_1 in (6-42) is real.

With the notation introduced above, we can directly use the analysis which led to Fig. 6.2, provided that k_ρ^2 -plane is replaced by k_x^2 -plane. Therefore, referring to Fig. 6.2, we define the branch cut in the k_x^2 -plane by

$$\text{Re}(k_x^2) < \tau \quad \text{and} \quad \text{Im}(k_x^2) = \Omega. \quad (6-43)$$

These relations define a pair of branch cuts in the k_x -plane, whose shape depends on the values of k_1 (and thus frequency) and k_y (or α and β). In addition to the branch points, there will also be a finite number of poles in the top sheet of the k_x -plane, contributed by the zeroes of the denominator functions D^e and D^h . These poles are easily determined in the k_ρ -plane (recall that $k_\rho^2 = k_x^2 + k_y^2$), where they are located on the real axis between k_1 and k_2 , and also between $-k_2$ and $-k_1$ [31]. Their locations in the k_x -plane will depend on the value of k_y . In the following analysis, we assume for simplicity that only one pair of poles, $\pm k_s$, associated with the TM_0 mode of the slab, occurs. This is the case most frequently encountered in practice.

As mentioned above, the shape and location of the branch-cuts in the k_x -plane depends on the value of k_y . Following the analyses of [60,61,62], we divide the range of k_y into three subregions, according to

$$\begin{aligned} (i) \quad & k_s^2 < \beta^2 < k_2^2, \quad \alpha = 0 \\ (ii) \quad & k_1^2 < \beta^2 - \alpha^2 < k_s^2 \\ (iii) \quad & 0 < \beta^2 - \alpha^2 < k_1^2 \end{aligned} \tag{6-44}$$

where $\beta^2 - \alpha^2 = \text{Re}(k_y^2)$. In region (i), k_y is real and the stripline mode is bound, i.e., it propagates unattenuated. The fields of bound modes are concentrated in the region of the strip and decay exponentially in transverse directions away from it. In regions (ii) and (iii), k_y is complex ($\alpha > 0$), and the mode is said to be leaky [60,61,62]. In this regime, the mode is attenuated as it propagates, due to the leakage of energy into the environment. In region (ii), there is only leakage into a surface wave of the slab, which propagates away from the strip. It can be shown [60] that the field of such mode decays exponentially in the z direction, but increases

exponentially away from the strip in $\pm z$ directions. For k_y in region (iii), the leakage is both into the surface wave and into the space wave. The field amplitude increases exponentially in the directions perpendicular to the strip [60,63].

Let us first consider the bound modes, for which k_y is in region (i) (cf. (6-44)). With $\tau < 0$ and $\Omega = 0$ in (6-42), the two-sheeted complex k_x^2 -plane is mapped into a two-sheeted k_x -plane as illustrated in Fig. 6.7a. The poles are in this case located in the $(-j\sqrt{k_y^2 - k_1^2}, j\sqrt{k_y^2 - k_1^2})$ interval of the imaginary k_x -axis, as shown in Fig. 6.7a. The integration path in (6-38) is chosen along the real axis on the top sheet (Fig. 6.7a).

When k_y passes from region (i) to region (ii), k_y acquires the imaginary part, so that $\tau < 0$ and $\Omega > 0$. In this process the pole on the negative imaginary axis in the k_x -plane moves to the origin, then enters the first quadrant, as illustrated in Fig. 6.7b. In a like manner, the pole on the positive imaginary axis moves to the third quadrant. The integration path must be deformed so that the pole in the first quadrant lies below the path, as illustrated in Fig. 6.7b. The first quadrant pole contributes an exponentially increasing surface wave, in agreement with the discussion above.

When k_y moves from region (ii) to region (iii), the value of τ changes sign, hence in region (iii) $\tau > 0$ and $\Omega > 0$ (cf. (6-42) and (6-44)). At the transition point $\tau = 0$, the branch points in the first and third quadrants switch positions along the diagonal line in the k_x -plane. Therefore, the integration path must go above the branch point κ in the first quadrant, as illustrated in Fig. 6.7c. One can prove that this, in turn, leads to a modal field which grows exponentially in the z direction [63]. The dashed line on the integration path in Fig. 6.7c means that the

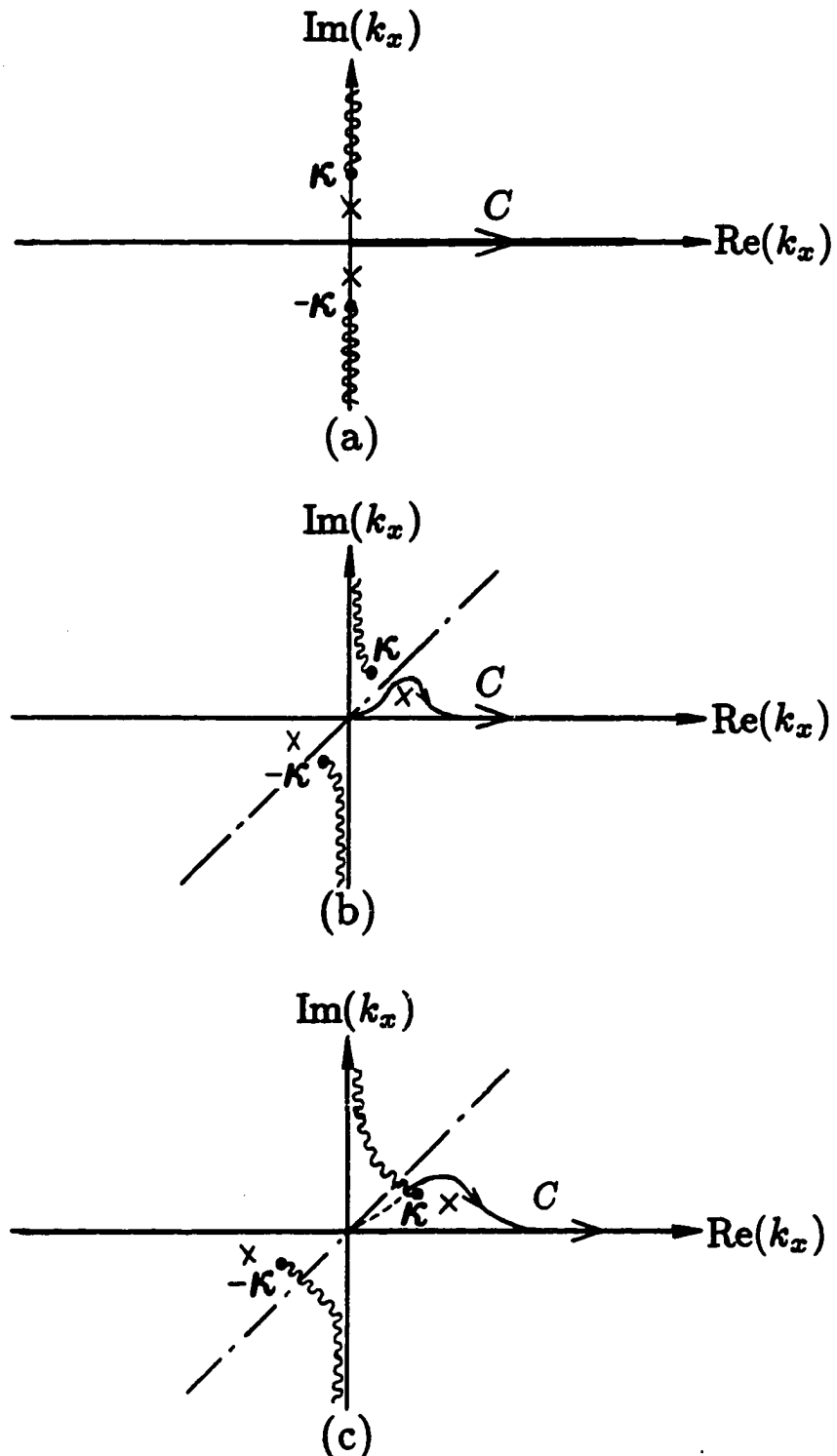


Fig. 6.7. The k_x -plane showing the branch cuts, the poles and the integration paths for (a) bound modes, region (i), (b) leaky modes, region (ii) and (c) leaky modes, region (iii).

path is on the bottom sheet.

As the above analysis indicates, different integration paths must be employed depending on which mode is being computed. The various paths are suggested in Fig. 6.7. In the computer implementation, to accelerate the convergence of the integral and to avoid the singularities, slightly modified paths, shown in Fig. 6.8 have been employed. For bound modes, we use the paths shown in Fig. 6.8a, where the value of P is arbitrarily chosen as $P = k_1$. For the k_y in region (ii), the paths in Fig. 6.8b are employed, where P is the same as that in Fig. 6.8a and the value of T is chosen as $T = |\operatorname{Re}(k_2^2 - k_y^2)^{\frac{1}{2}}| + k_1$ to ensure that the pole is located to the left of this point. The integration around the pole is carried out by the method of residues. For k_y in region (iii), we employ the paths shown in Fig. 6.8c, where T is the same as that in Fig. 6.8b and the value of P is chosen as $P = |\operatorname{Im}(k_1^2 - k_y^2)^{\frac{1}{2}}| + k_1$ to ensure that the branch point in the first quadrant lies below the paths. In all three cases, when $z = z' = 0$ (this is always the case for an infinitely thin strip), we use path C_1 in Fig. 6.8. When the path is on the real axis, the method of averages [17] discussed in the previous section is employed to accelerate the rate of convergence. When $h = |z| + |z'| > 0$, path C_2 is used to benefit the convergence from the exponential function associated with h .

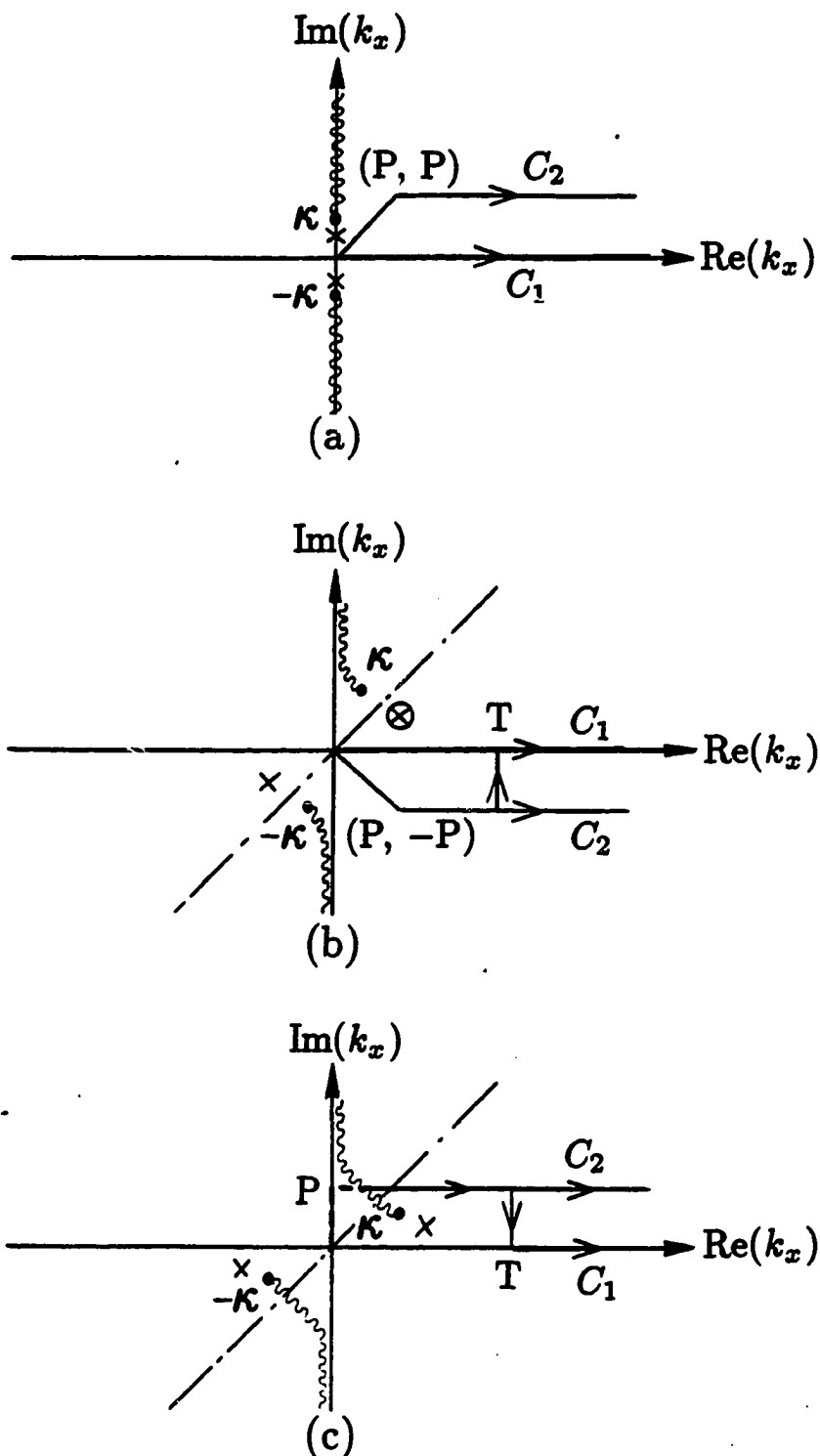


Fig. 6.8. Various integration paths in the computer implementation for (a) bound modes, region (i), (b) leaky modes, region (ii) and (c) leaky modes, region (iii).

CHAPTER 7

NUMERICAL RESULTS

In this chapter, we present sample numerical results for several partially buried antennas and scatterers, and for open microstrip lines. In all cases, the medium of Region 1 is free space with parameters $\epsilon_1 = \epsilon_0$ and $\mu_1 = \mu_0$. The medium of Region 2 is characterized by ϵ_2 and $\mu_2 = \mu_0$, and it may be lossy or lossless. In the former case, its permittivity is complex and is given as $\epsilon_2 = \epsilon_0\epsilon_r - j\sigma/\omega$, where ϵ_r and σ are the relative dielectric constant and the conductivity of the medium, respectively, and $\omega = 2\pi f$. For the radiation and scattering problems, to facilitate the interpretation of the results, we take in all cases $f = 300$ MHz, which corresponds to free space wavelength $\lambda_0 = 1$ m. The results for antennas assume unit-strength δ -gap generators, and the results for scatterers assume illumination by plane waves incident normally on the interface. For the open microstrip line problem, the current distributions are normalized to have a maximum value of one for the longitudinal current density.

7.1. Surfaces

We first consider a straight, inclined, thin-wire antenna with radius a , partially buried in dry earth, as illustrated in Fig. 7.1a. In the numerical procedure, the wire was approximated by a flat, narrow strip of width $2\pi a$, which was modeled by 60 triangular patches, as shown in Fig. 7.1b. In Fig. 7.2, the computed current distributions on the wire are compared with the data from the NEC [26]. A

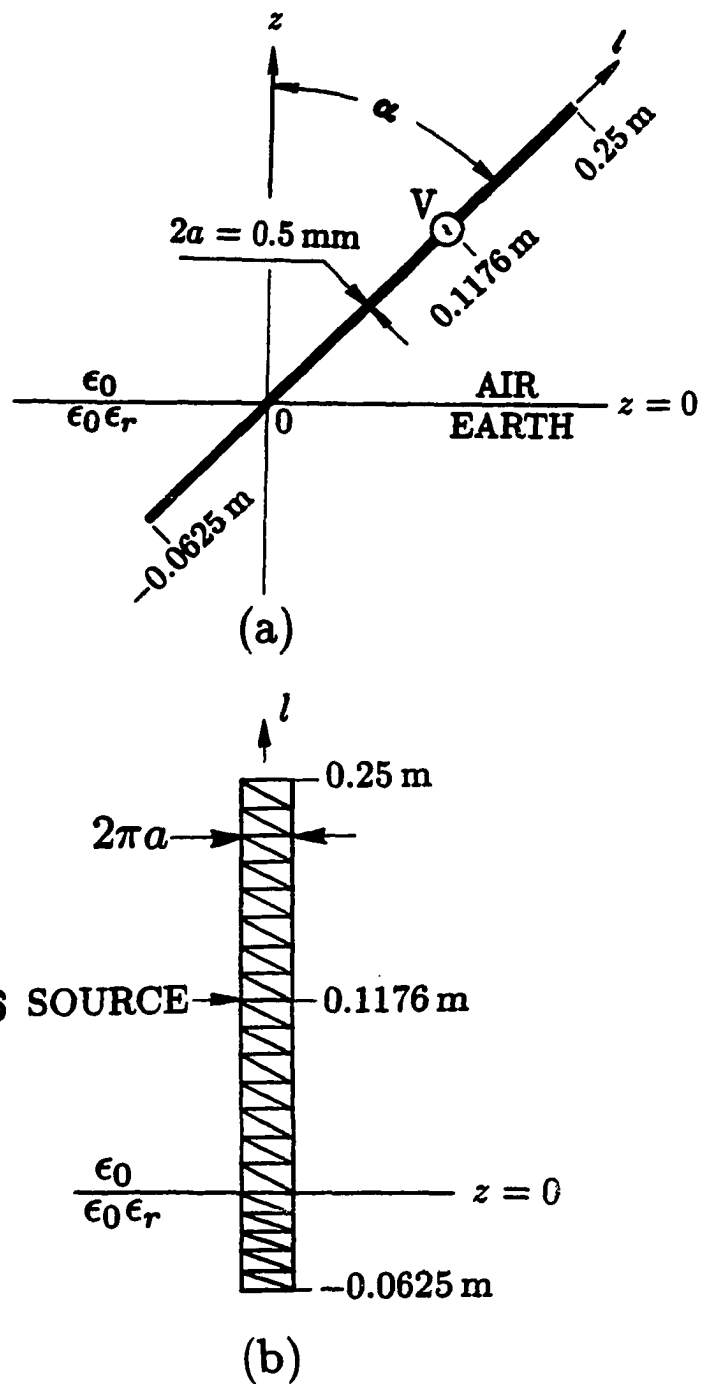


Fig. 7.1. (a) Inclined thin-wire antenna partially buried in earth and (b) its strip model.

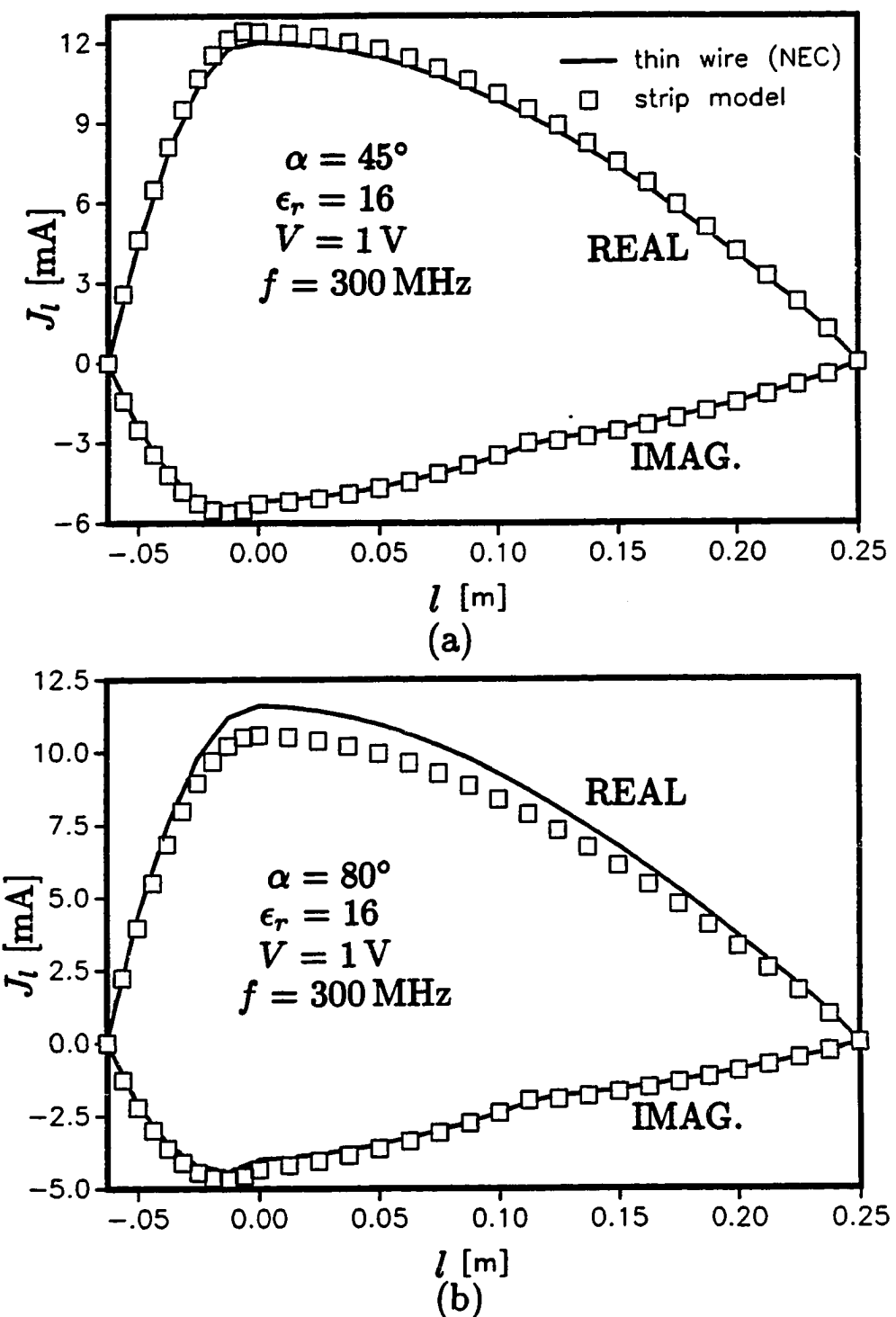


Fig. 7.2. Current distribution on the strip model of Fig. 7.1 for (a) $\alpha = 45^\circ$ and (b) $\alpha = 80^\circ$.

good agreement is observed for the inclination angle $\alpha = 45^\circ$ (Fig. 7.2a), while for $\alpha = 80^\circ$ (Fig. 7.2b) the agreement is less favorable. A possible explanation of this slight disagreement is the fact that in the NEC formulation a charge discontinuity condition at the interface is enforced, which is strictly valid only for the vertical antenna [26]. Obviously, this condition would affect the solution more for $\alpha = 80^\circ$ than for $\alpha = 45^\circ$.

In Fig. 7.3 is shown a relatively thick, vertical, cylindrical antenna, which penetrates the interface between two media. This so-called ground stake antenna was previously analyzed by Butler and Michalski [63]. In the numerical procedure, the circular cylinder was approximated by a square cylinder with the same circumference, and was modeled by 112 triangular patches. We show the axial current distribution on the antenna for the cases where the lower medium is dry earth (Fig. 7.4a) and salt water (Fig. 7.4b). Our results are seen to perfectly agree with the data obtained in [63]. Since our code can handle surfaces of arbitrary shape, it was a simple matter to examine the effect of putting the end caps on the hollow cylinder. The resulting current distributions are also displayed in Fig. 7.4. One observes that, as expected, the caps only affect the current near the ends of the cylindrical surface.

The results in Fig. 7.5 are for a finite, hollow, horizontal cylinder, which is partially buried in a dielectric medium (see the inset). The corresponding two-dimensional problem has been solved by Xu [25], who employed the magnetic field integral equation formulation. One observes that both the magnitude (Fig. 7.5a) and phase (Fig. 7.5b) of the normalized current distribution along the circumference and in the middle of the finite tube agree favorably with the corresponding results

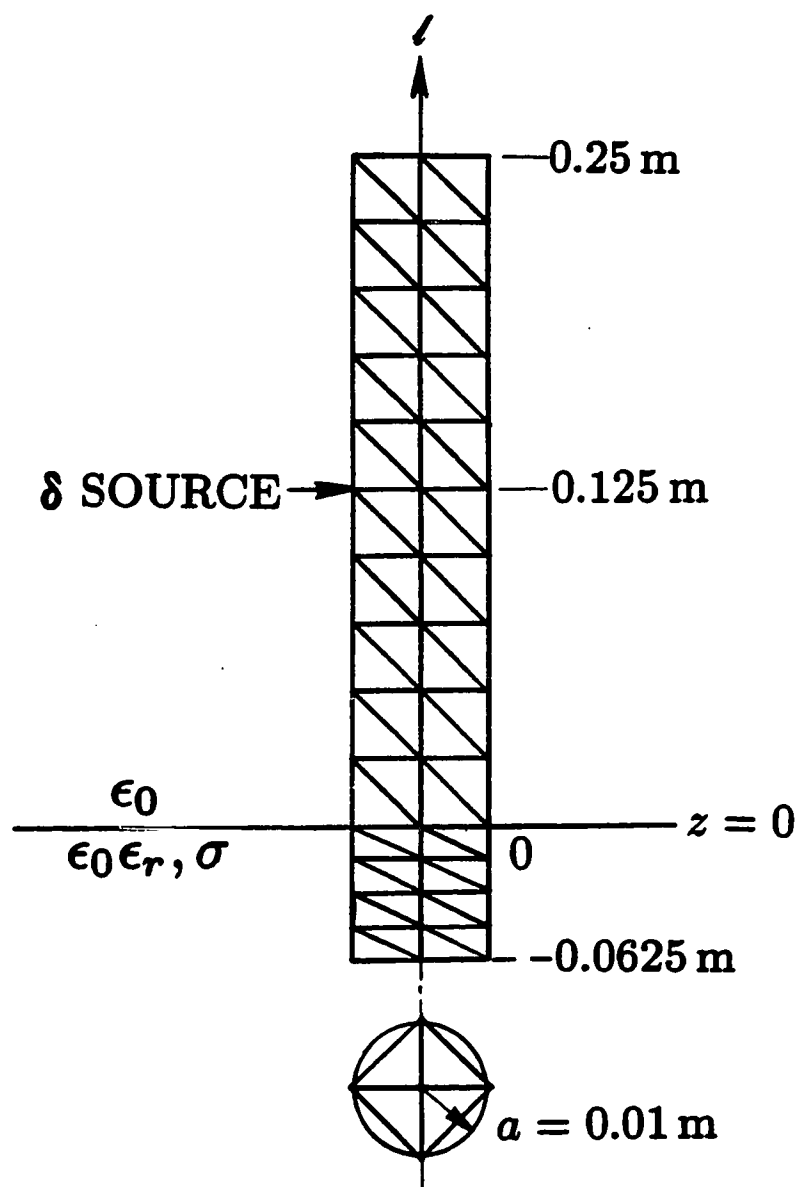


Fig. 7.3. Vertical, cylindrical antenna penetrating the interface between two media. The antenna is approximated by triangular patches.

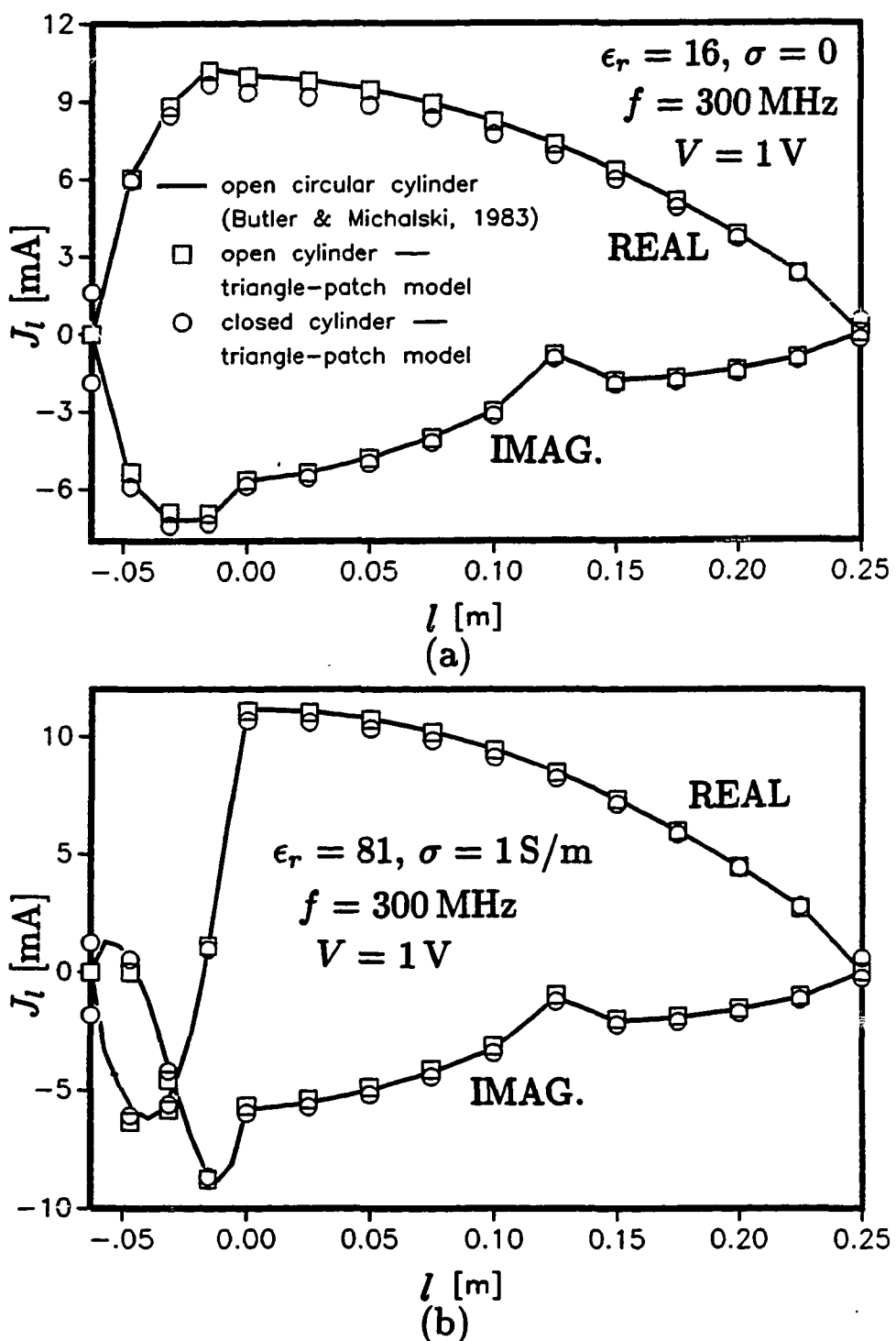


Fig. 7.4. Current distribution on an open-ended and closed cylindrical antenna of Fig. 7.3 partially buried in (a) dry earth and (b) salt water.

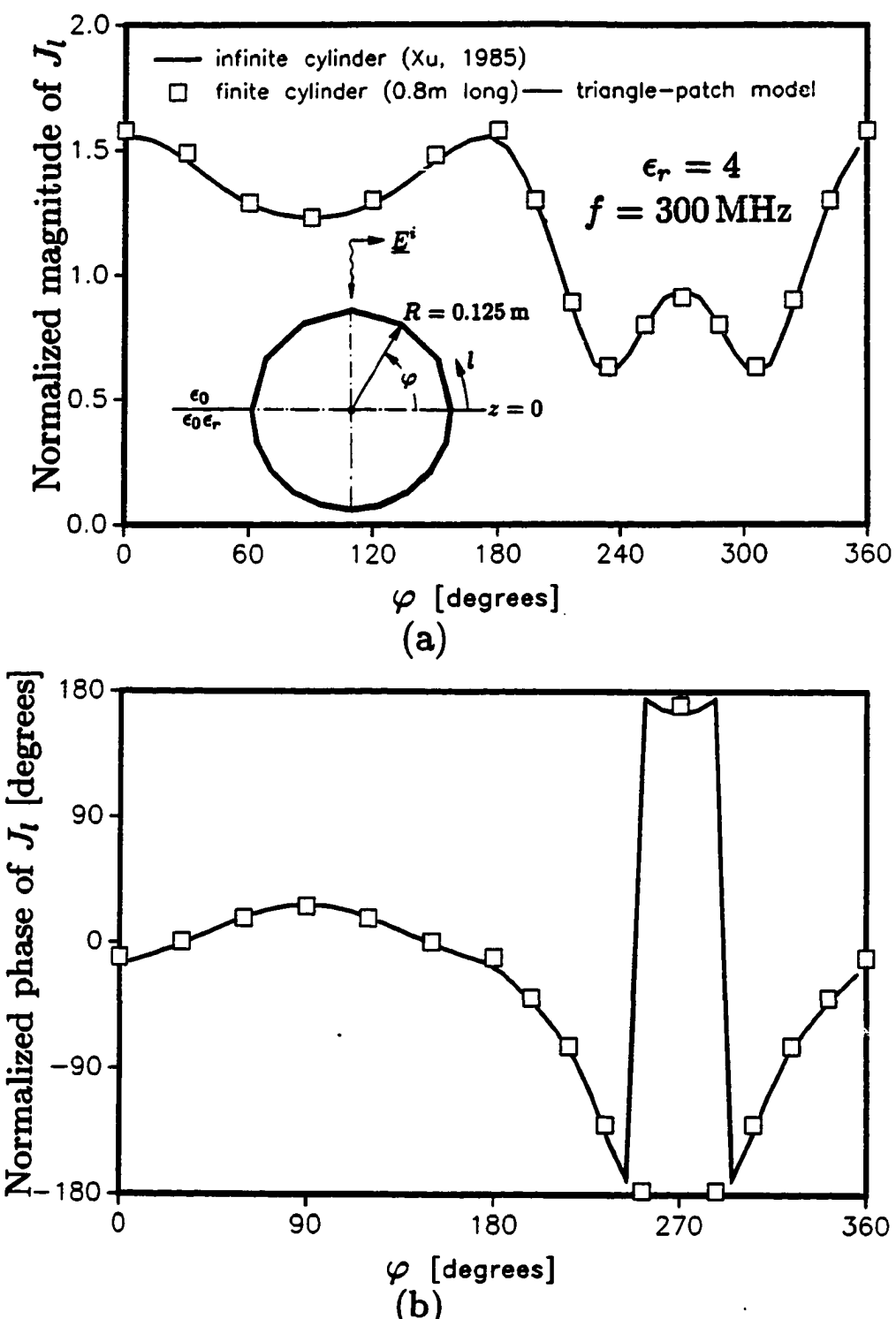


Fig. 7.5. (a) Magnitude and (b) phase of the current J_l on a horizontal tube partially buried in a dielectric medium. The current is normalized to the incident magnetic field at $\varphi = 90^\circ$ on the surface of the tube.

for the infinite cylinder. In the triangle-patch model of the cylinder, 288 patches were employed.

In Fig. 7.6—7.9, we present results for a flat, rectangular plate partially buried in dry earth (see the inset in Fig. 7.6a). The magnitudes of the dominant and transverse components of the current distribution on the plate are shown in Fig. 7.7a and Fig. 7.7b for the inclination angle $\alpha = 30^\circ$, and in Fig. 7.9a and Fig. 7.9b for $\alpha = 60^\circ$. In the triangle-patch model of the plate, 252 patches were employed.

The slight nonsymmetry with respect to the center line of the plate observed in the transverse component of the current is due to the fact that the symmetry of the plate was not preserved in its triangle-patch model. In Figs. 7.6 ($\alpha = 30^\circ$) and 7.8 ($\alpha = 60^\circ$) we compare the dominant component of the current distribution along the center line of the plate with the corresponding result for an infinite strip [25]. One observes a reasonably good agreement between the two results, both in magnitude (Fig. 7.6a) and phase (Fig. 7.6b) for $\alpha = 30^\circ$, and a less favorable agreement for $\alpha = 60^\circ$. This discrepancy can perhaps be attributed to the fact that an infinite strip is not a very good model for the relatively short plate.

7.2. Thin Wires

The next problem considered is that of a straight, inclined, thin-wire antenna which is partially buried in moist earth, as shown in Fig. 7.10. The computed current distributions on the antenna for $\alpha = 45^\circ$ and $\alpha = 80^\circ$ are compared in Figs. 7.11a and 7.11b, respectively, with the NEC [26]. The agreement is seen to be excellent in the first case, but it is poor in the last case. A possible explanation of this discrepancy of the results for $\alpha = 80^\circ$ has been given in the previous section.

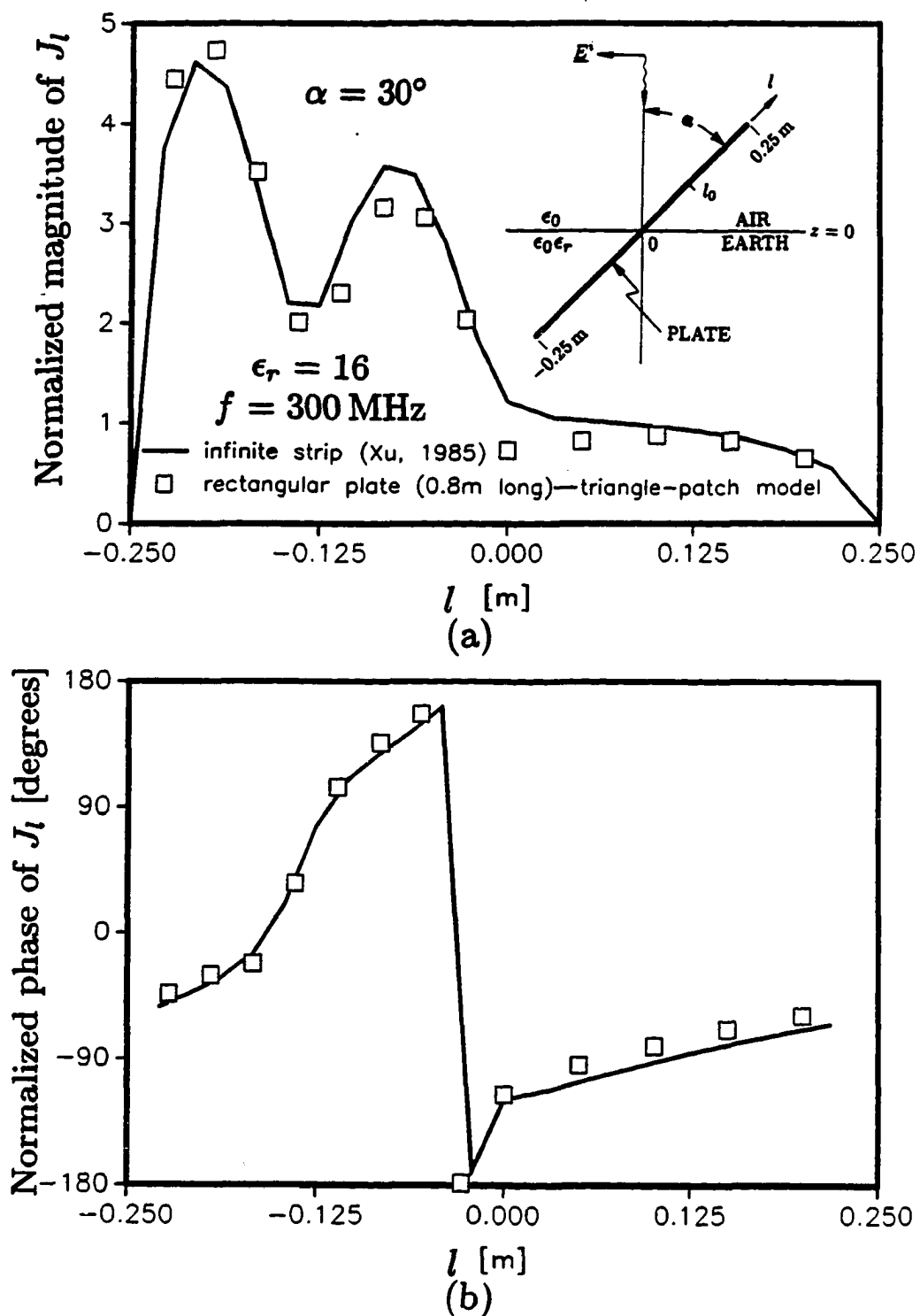


Fig. 7.6. (a) Magnitude and (b) phase of the current J_l along the center line of a rectangular plate partially buried in dry earth for the inclination angle $\alpha = 30^\circ$. The current is normalized to the incident magnetic field at $l_0 = 0.125 \text{ m}$.

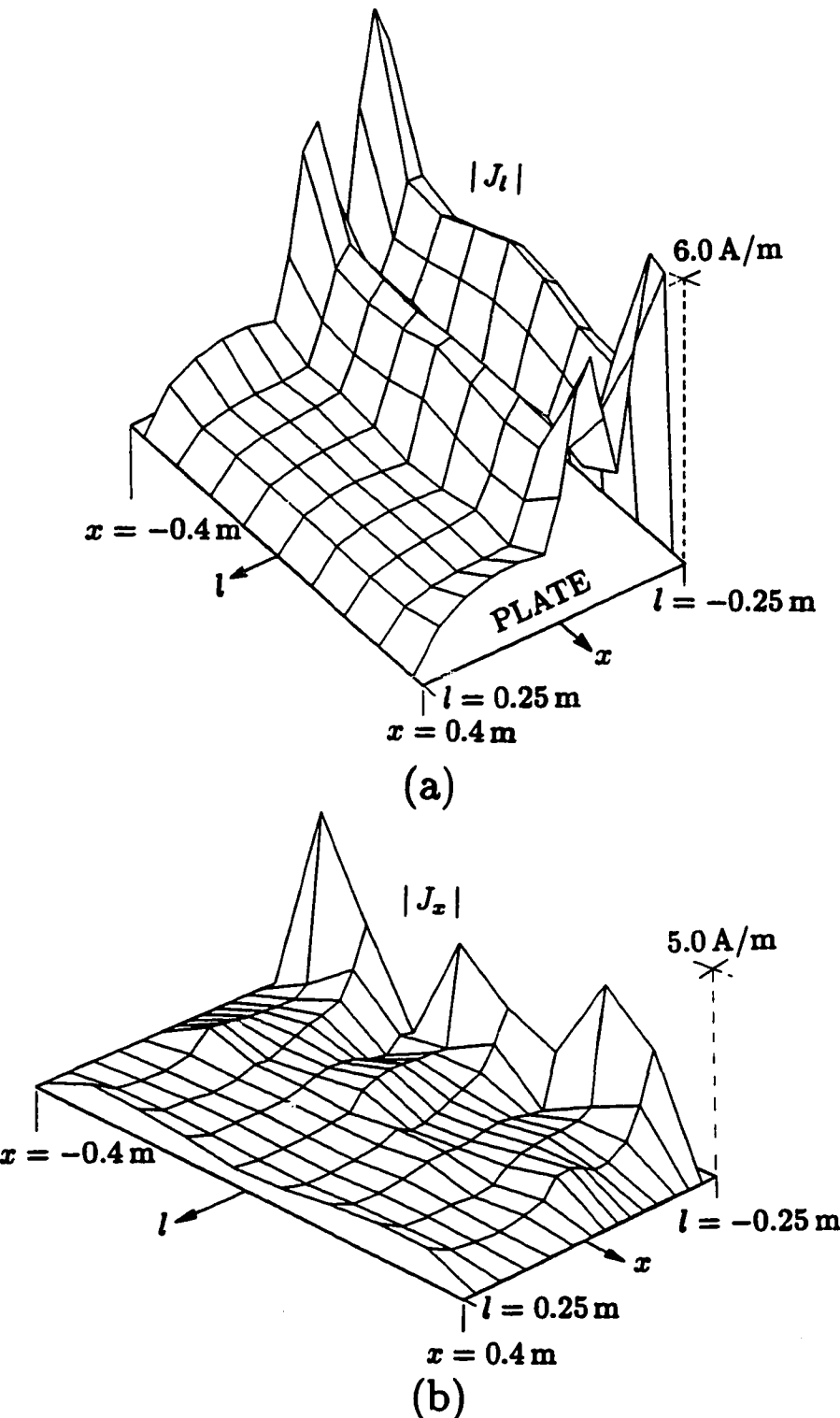


Fig. 7.7. Magnitude of (a) the longitudinal and (b) the transverse component of the current induced on the rectangular plate of Fig. 7.6 for $\alpha = 30^\circ$ by a normally-incident plane wave with $H_x^i = 1 \text{ A/m}$.

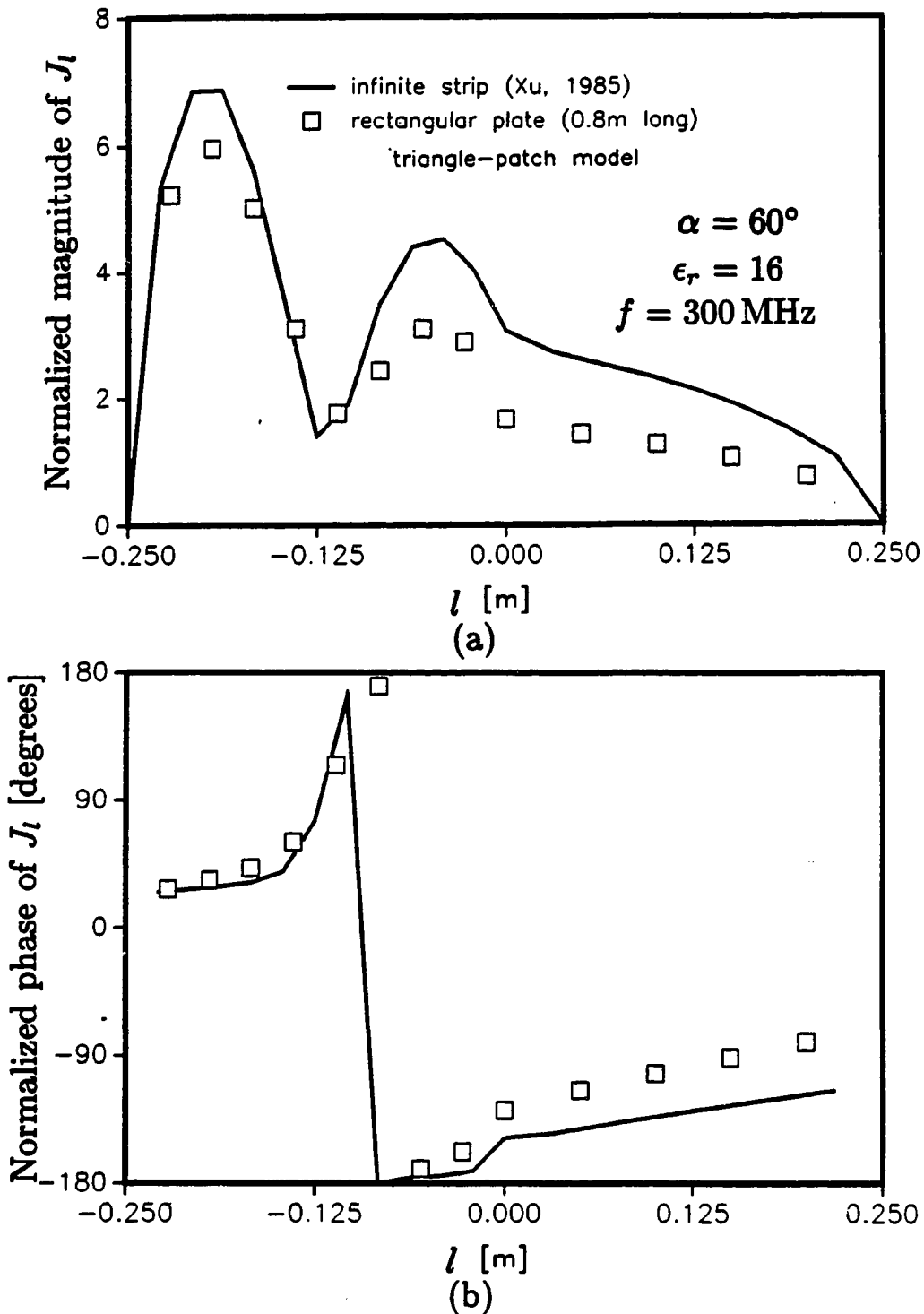


Fig. 7.8. (a) Magnitude and (b) phase of the current J_l along the center line of a rectangular plate of Fig. 7.6 for $\alpha = 60^\circ$. The current is normalized to the incident magnetic field at $l_0 = 0.125$.

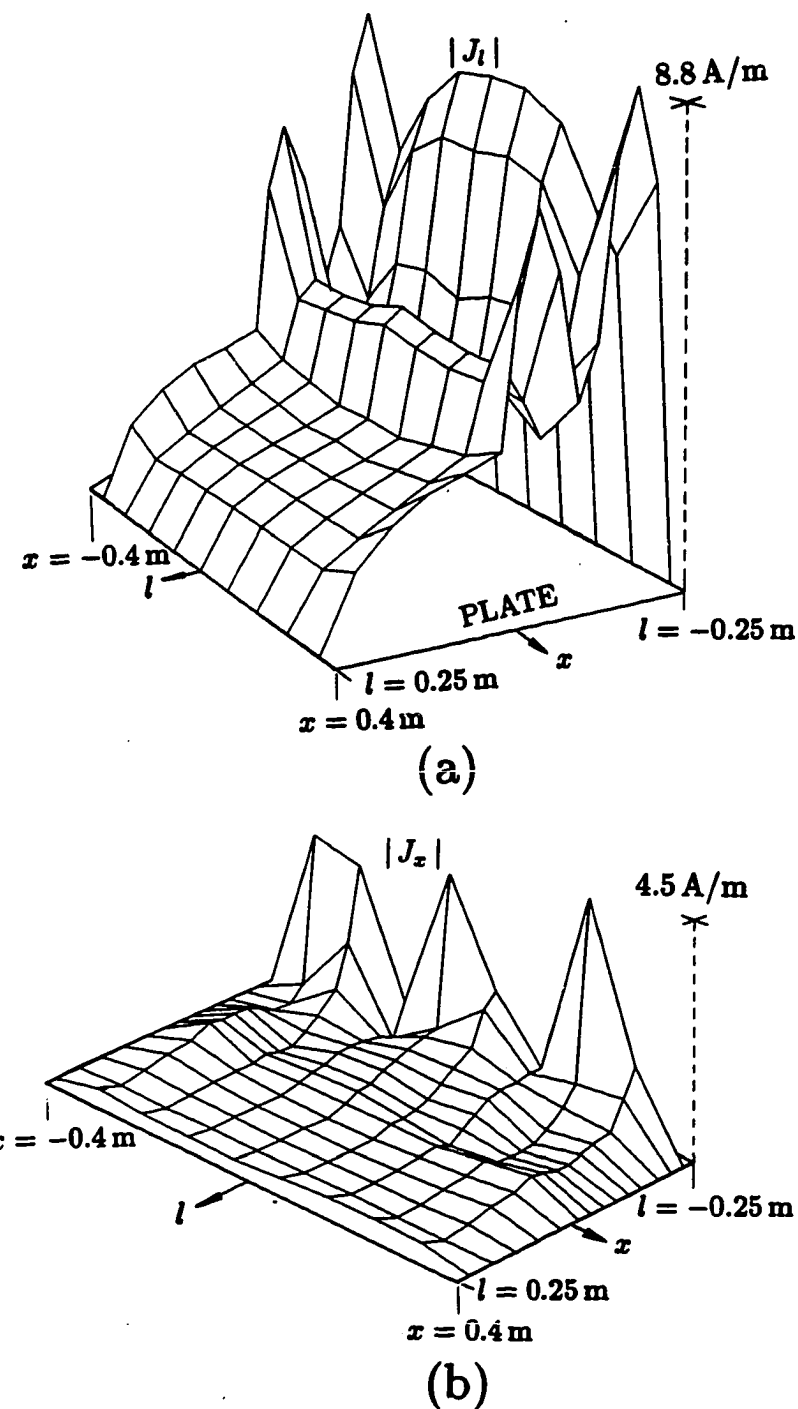


Fig. 7.9. Magnitude of (a) the longitudinal and (b) the transverse component of the current induced on the rectangular plate of Fig. 7.6 for $\alpha = 60^\circ$ by a normally-incident plane wave with $H_x^i = 1 \text{ A/m}$.

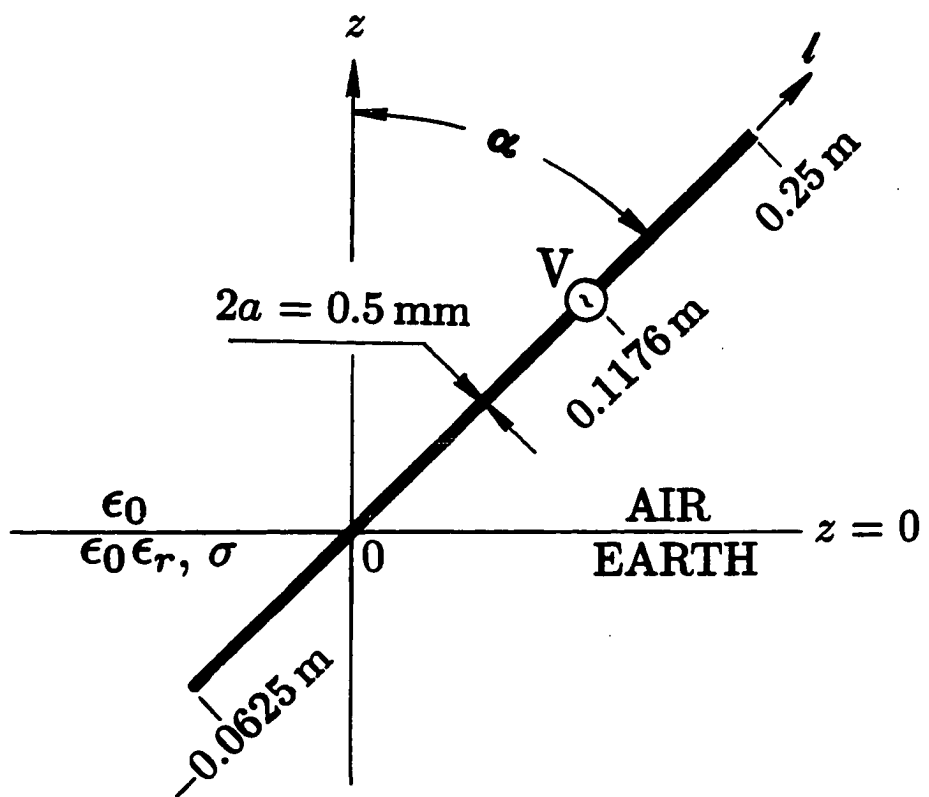


Fig. 7.10. Inclined thin-wire antenna partially buried in moist earth.

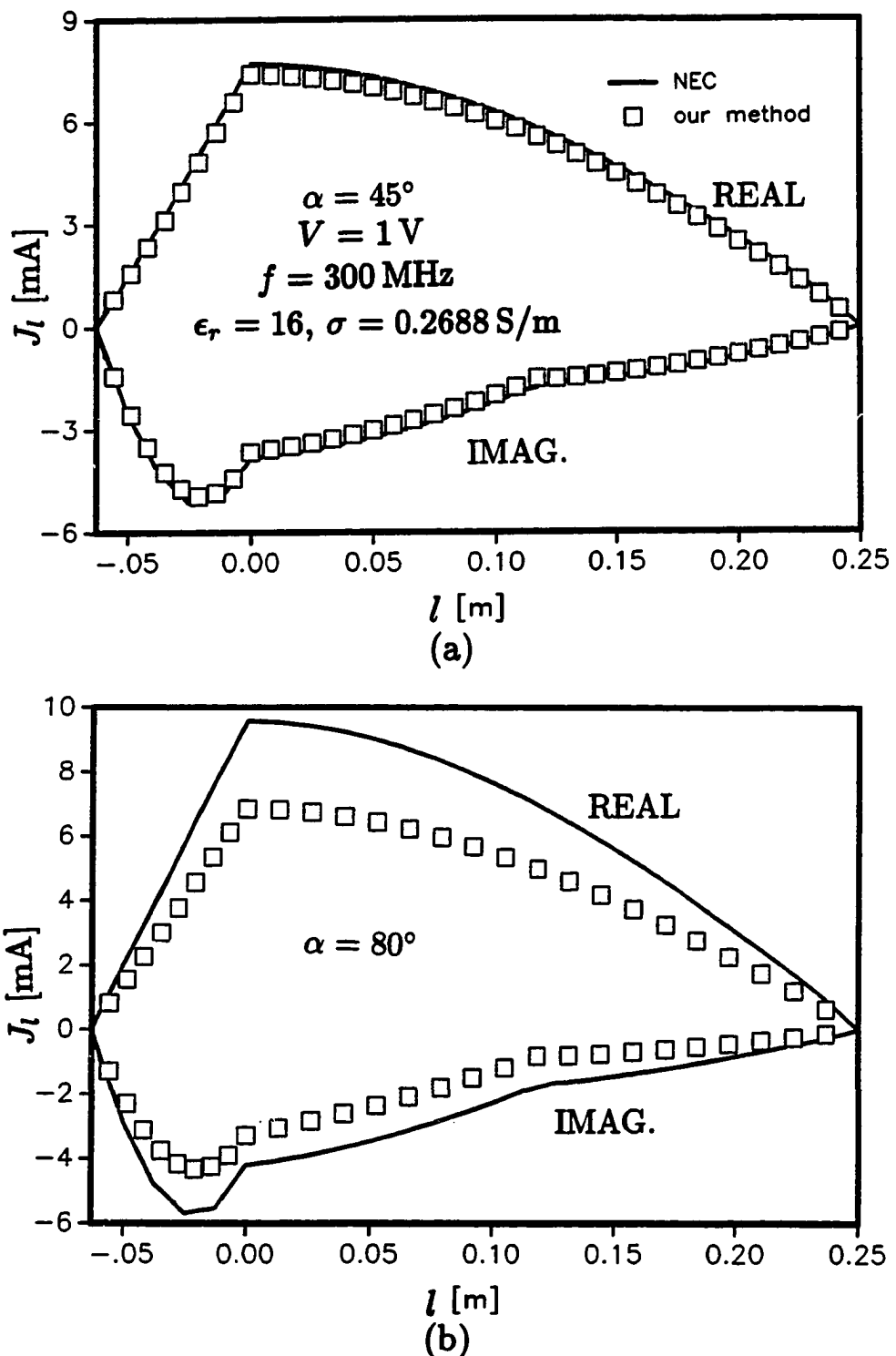


Fig. 7.11. Current distribution on the antenna of Fig. 7.10 for (a) $\alpha = 45^\circ$ and (b) $\alpha = 80^\circ$.

Next, we consider the case of a vertical, rectangular, loop antenna partially immersed in water, as illustrated in Fig. 7.12, for which measured data are available [65]. The current distributions on the lower arm of the loop are presented in Fig. 7.13 ($\epsilon_r = 81$, $\sigma = 0$) for tap water, and in Figs. 7.14 ($\epsilon_r = 79$, $\sigma = 1 \text{ S/m}$) and 7.15 ($\epsilon_r = 76$, $\sigma = 1.75 \text{ S/m}$) for salt water. One observes a good agreement of the computed and measured results, both in magnitude and phase.

7.3. Open Microstrip Line

In this section we consider an open microstrip line, illustrated in Fig. 7.16. The strip is of width w and it may be infinitely thin, or it may have finite thickness t . In Fig. 7.17, we present the dispersion curves for the lowest mode (EH_0) and the first higher mode (EH_1) for an infinitely thin microstrip line and for a line with finite thickness ($t/w = 0.1$). The dimensions are $w = 15 \text{ mm}$, $d = 0.794 \text{ mm}$, $\epsilon_r = 2.32$. In this figure, Oliner and Lee's results [61,66] for $t = 0$ are also plotted for comparison. Oliner and Lee's analysis is based on the transverse-resonance method in conjunction with the Wiener-Hopf approach developed in [67]. Our result for the phase constant of the EH_1 mode, shown in Fig. 7.17a, is seen to agree completely with Oliner and Lee's work (within the error in reading from their curves) both in the bound and leaky regimes, except at the low end of the frequency range. The agreement of the attenuation constants, plotted in Fig. 7.17b, appears to be slightly less favorable. Note that in [61] and in [66], data for α are only given for, respectively, $f > 5 \text{ GHz}$ and $f > 6 \text{ GHz}$. In Figs. 7.18 and 7.19 we show the current distributions of the EH_0 and EH_1 modes on an infinitely thin strip at $f = 5 \text{ GHz}$ and $f = 10 \text{ GHz}$, respectively. The longitudinal currents (J_y) are

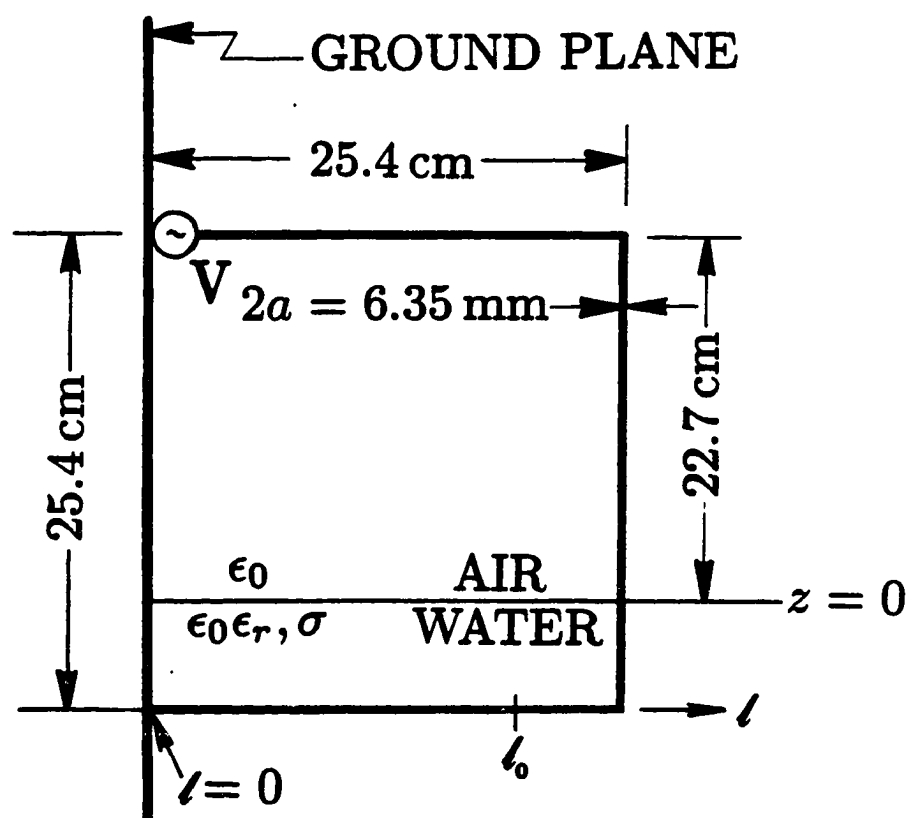


Fig. 7.12. Vertical, rectangular, loop antenna partially immersed in water.

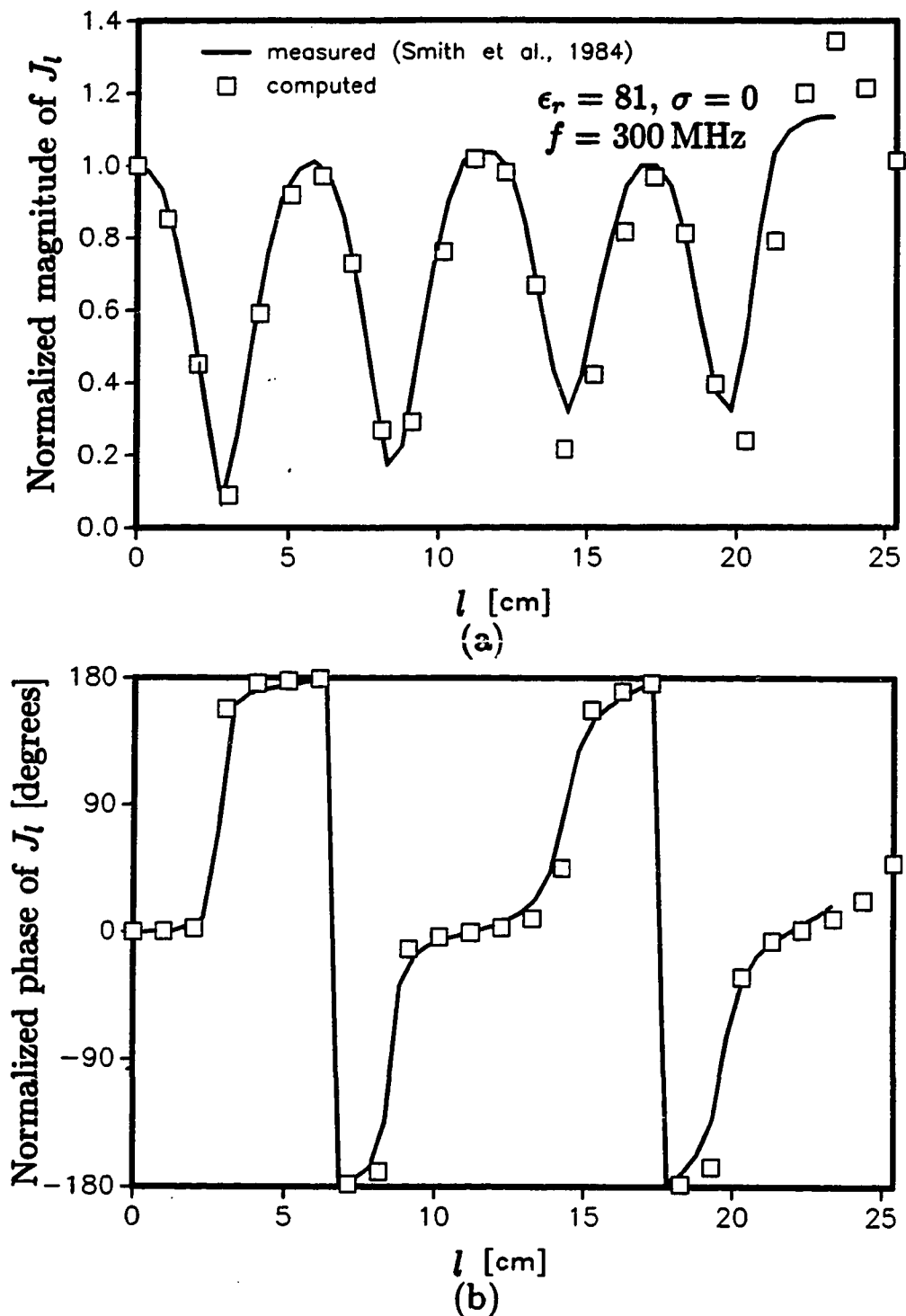


Fig. 7.13. (a) Magnitude and (b) phase of the current J_l on the lower arm of the antenna of Fig. 7.12 ($\epsilon_r = 81, \sigma = 0$). The current is normalized to its value at the point $l_0 = 0$.

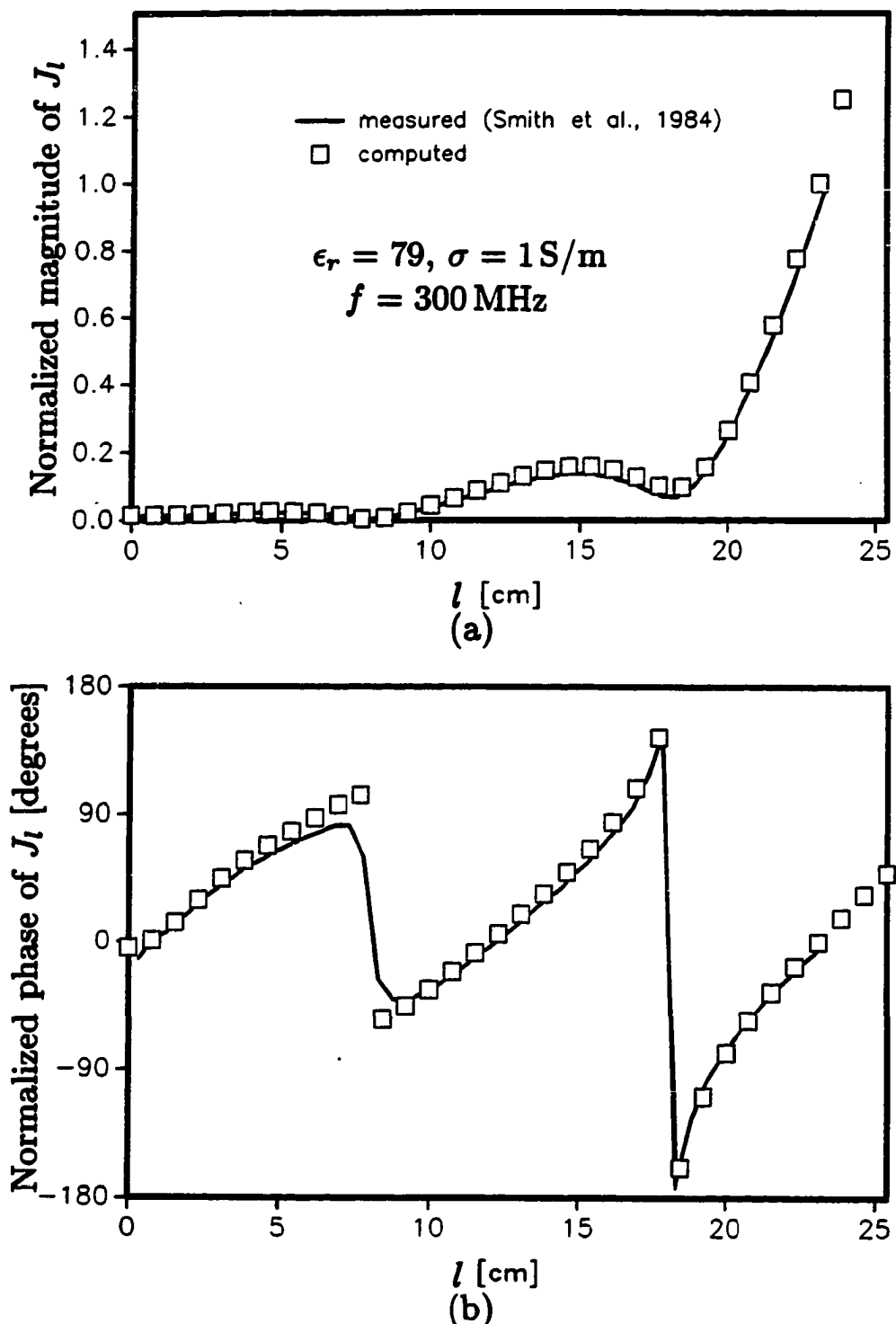


Fig. 7.14. (a) Magnitude and (b) phase of the current J_l on the lower arm of the antenna of Fig. 7.12 ($\epsilon_r = 79$, $\sigma = 1 \text{ S/m}$). The current is normalized to its value at the point $l_0 = 23.3 \text{ cm}$.

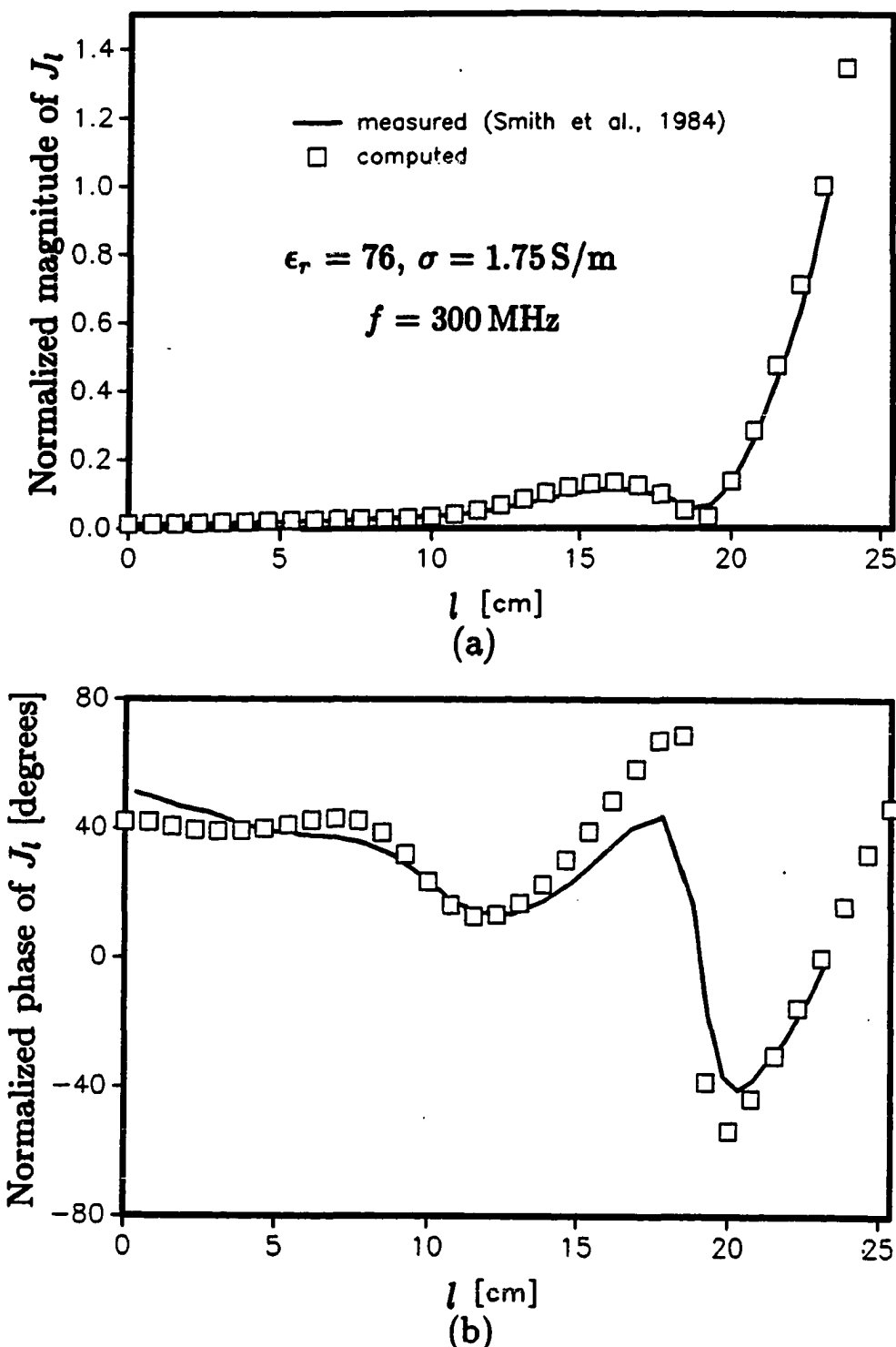


Fig. 7.15. (a) Magnitude and (b) phase of the current J_l on the lower arm of the antenna of Fig. 7.12 ($\epsilon_r = 76$, $\sigma = 1.75 \text{ S/m}$). The current is normalized to its value at the point $l_0 = 23.3 \text{ cm}$.

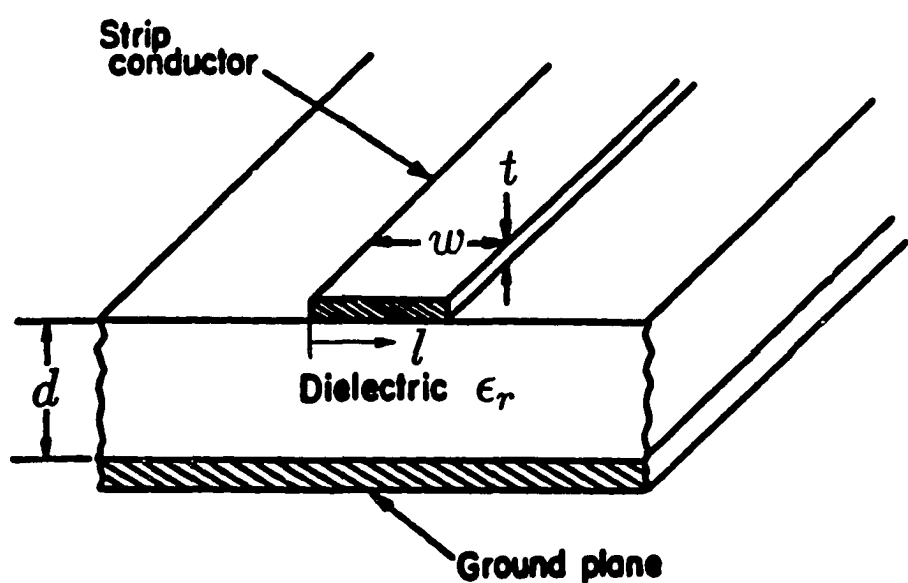


Fig. 7.16. Open microstrip line.

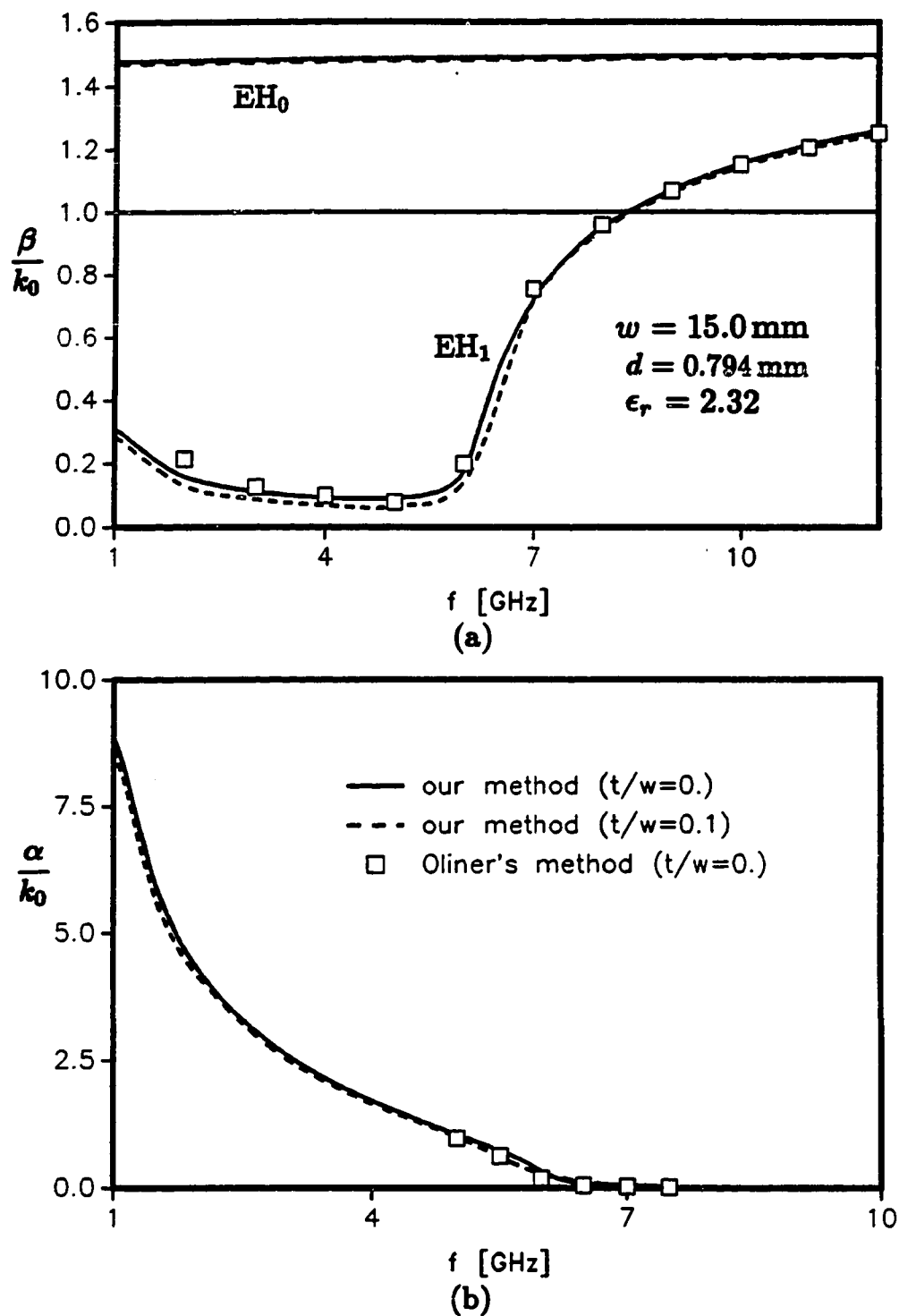
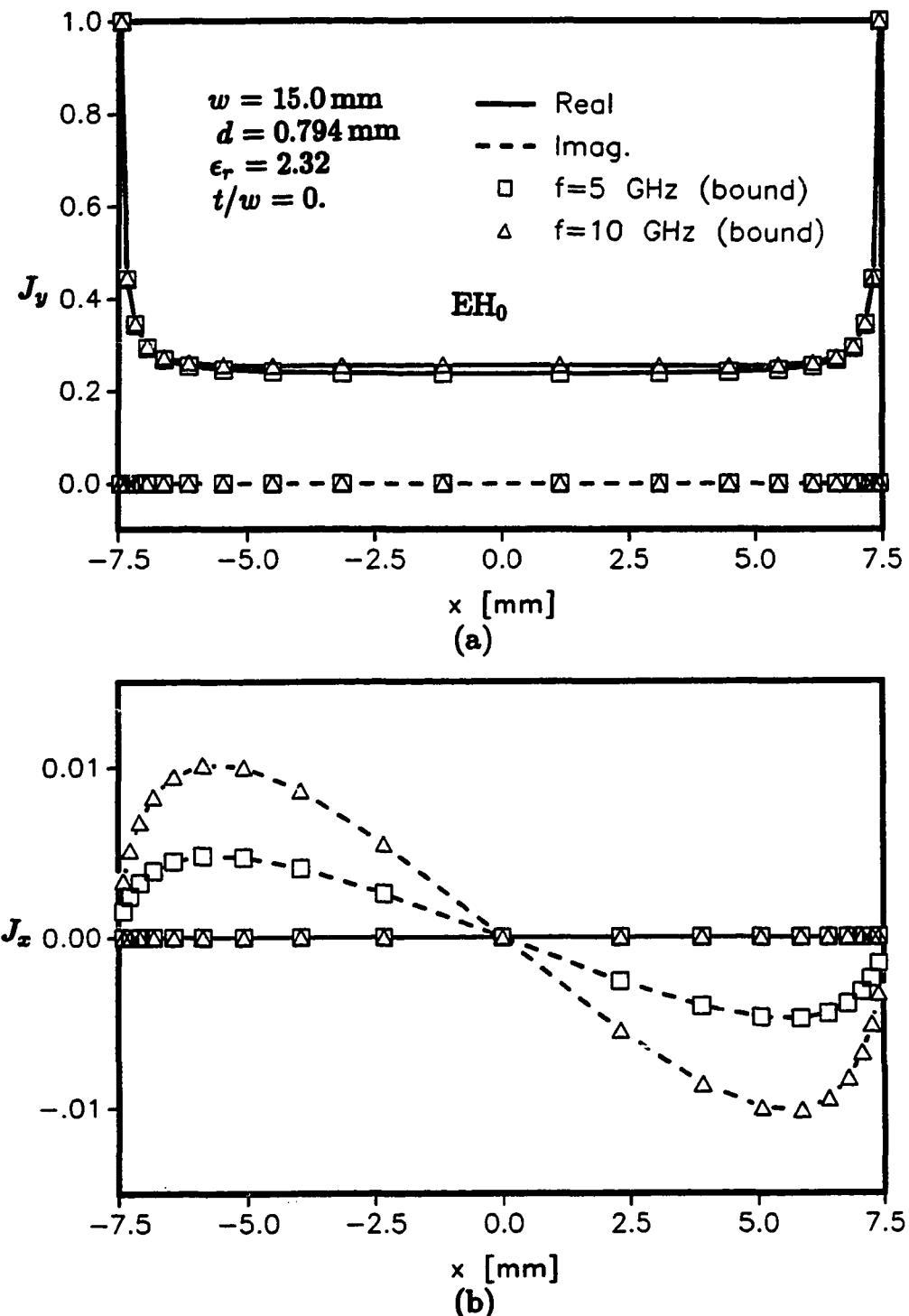


Fig. 7.17. Variation with frequency (a) of the normalized phase constant for the lowest mode (EH_0) and the first higher mode (EH_1), and (b) of the normalized attenuation constant for the EH_1 modes. The microstrip line dimensions are: $w = 1.5 \text{ cm}$, $d = 0.794 \text{ mm}$, $\epsilon_r = 2.32$.



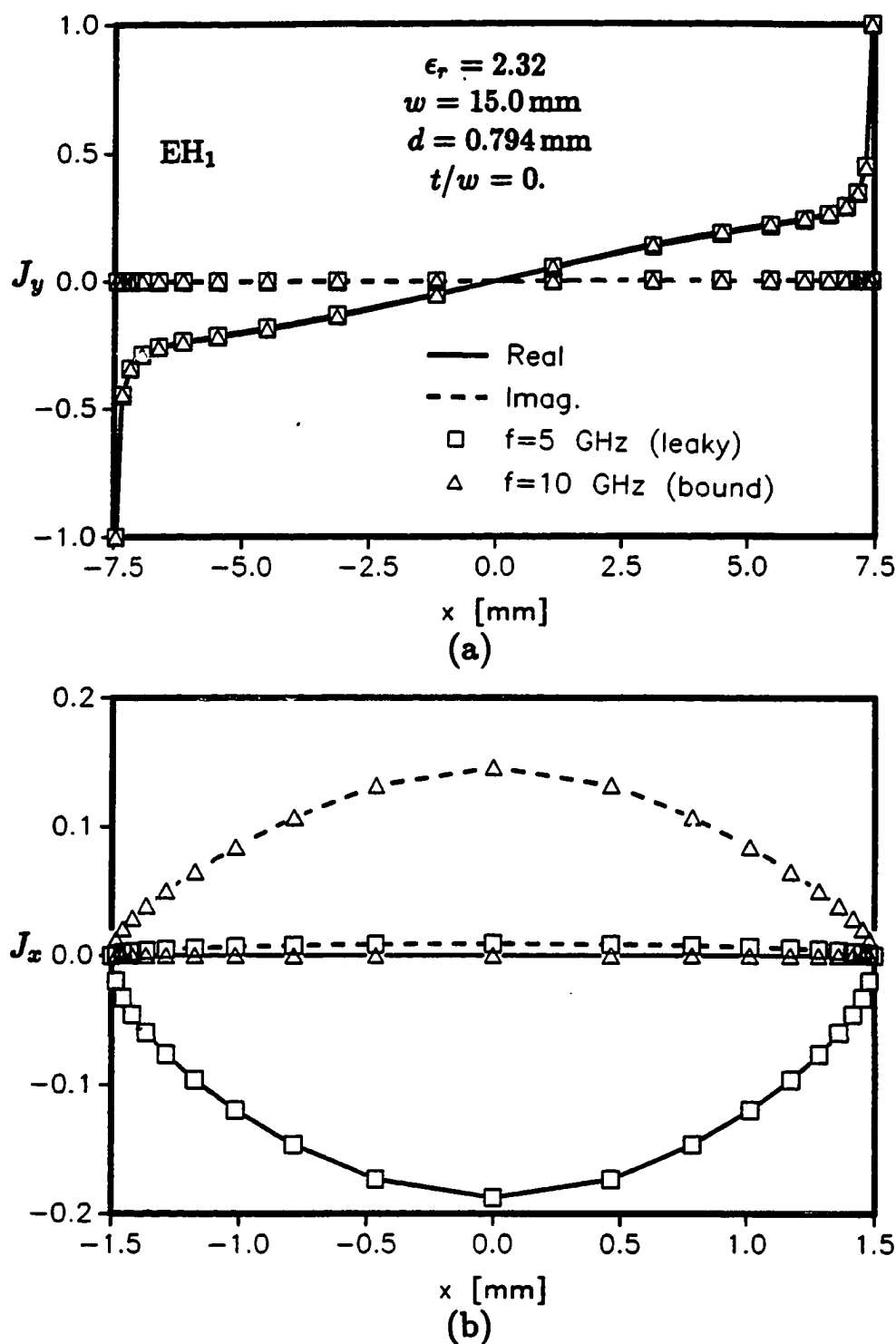


Fig. 7.19. (a) Longitudinal and (b) transverse current distribution of the EH_1 mode at $f = 5 \text{ GHz}$ (leaky regime (iii)) and $f = 10 \text{ GHz}$ (bound regime (i)) for the microstrip: $w = 1.5 \text{ cm}$, $d = 0.794 \text{ mm}$, $t/w = 0.$, $\epsilon_r = 2.32$.

plotted in Figs. 7.18a and 7.19a, and the transverse currents (J_x) in Figs. 7.18b and 7.19b. The symbols correspond to the locations where the current values are actually computed. Observe that nonuniform-width basis functions were used to better capture the singular behavior of the longitudinal current near the edges of the strip. It is noted in Figs. 7.18 and 7.19 that there is very little change in the longitudinal current distribution as the mode passes from the bound regime to the leaky regime. However, there is a noticeable change in the transverse current distribution.

In Figs. 7.20 and 7.21, we show the current distributions of the EH_0 and EH_1 modes for a strip with finite thickness ($t/w = 0.1$) at $f = 5 \text{ GHz}$ and $f = 10 \text{ GHz}$, respectively. It is noted that the current is concentrated on the lower face of the strip, as expected.

In Fig. 7.22, we present the dispersion curves for the lowest mode (EH_0) and the first three higher modes (EH_1 , EH_2 , and EH_3) for an infinitely thin microstrip line with $w = 3 \text{ mm}$, $d = 0.635 \text{ mm}$, and $\epsilon_r = 9.8$. One should keep in mind that the actual boundary corresponding to the leaky mode region (iii) for each mode is $(1 + (\alpha/k_0)^2)^{\frac{1}{2}}$, which obviously depends on the attenuation constant of the mode (cf. (6-44)). As illustrated in Fig. 7.22, the phase constants for the higher modes increase again after reaching a minimum and continue to increase as the frequency is lowered further. It is noted that k_y stays in region (iii) as the frequency decreases. In Fig. 7.23, we show the normalized phase constant for the EH_1 mode and the region (iii) boundary corresponding to this mode. In Fig. 7.24, we present the current distribution for the EH_2 mode at $f = 25 \text{ GHz}$ (leaky regime (iii)) and $f = 35 \text{ GHz}$ (bound regime). In Fig. 7.25, we show the current distribution for the

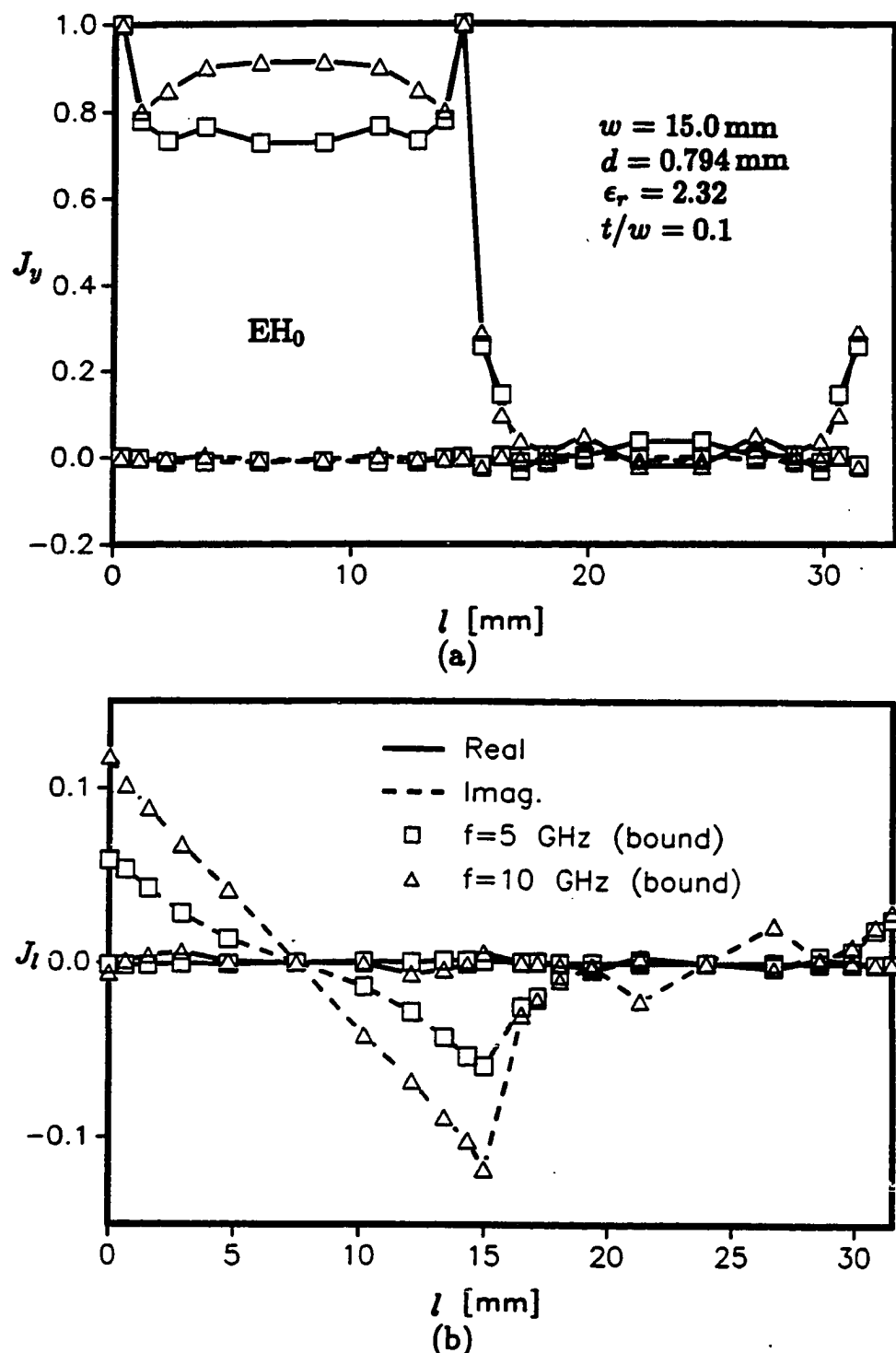


Fig. 7.20. (a) Longitudinal and (b) transverse current distribution of the EH_0 mode at $f = 5 \text{ GHz}$ and $f = 10 \text{ GHz}$ for the microstrip line with finite thickness: $w = 1.5 \text{ cm}$, $d = 0.794 \text{ mm}$, $t/w = 0.1$, $\epsilon_r = 2.32$.

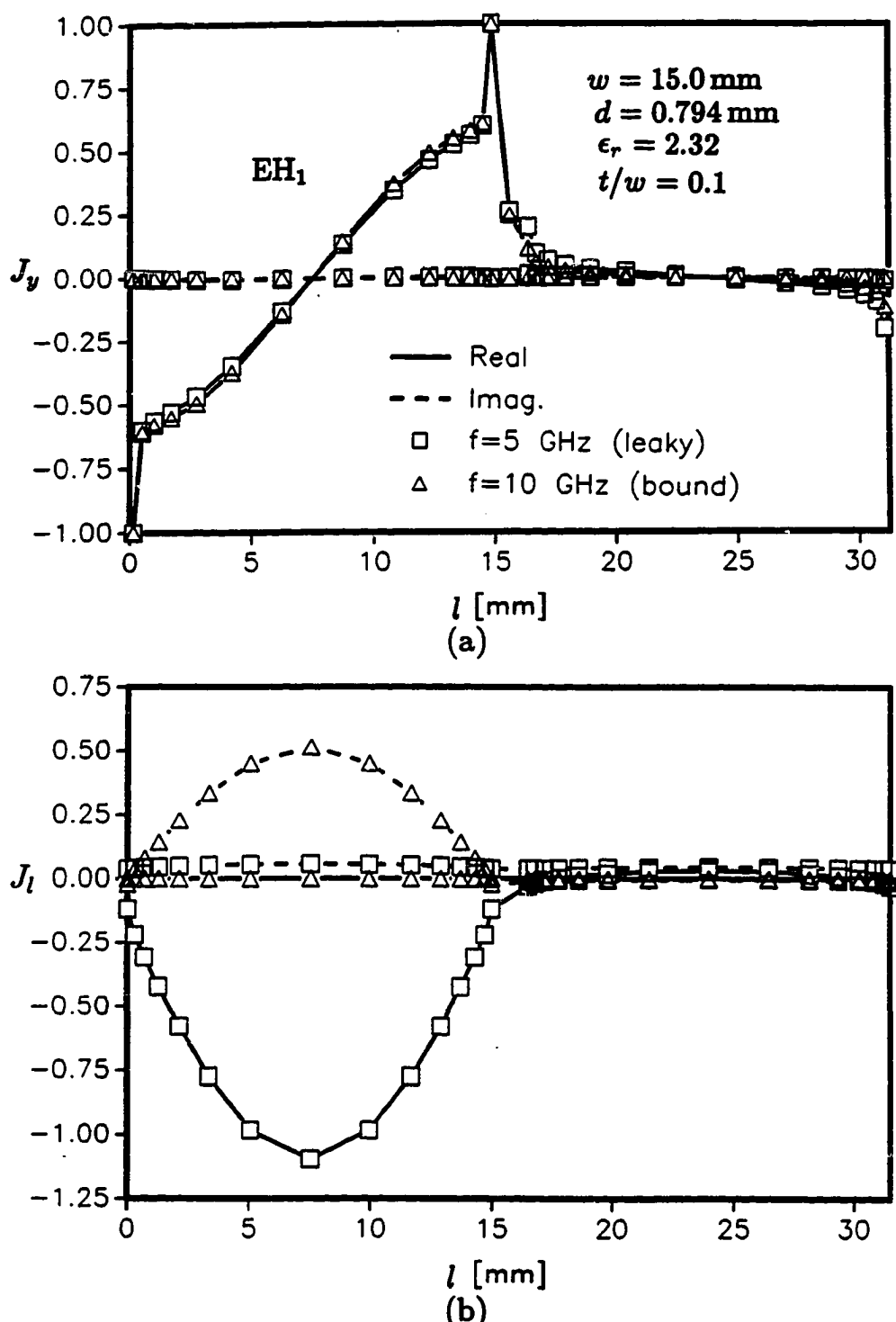


Fig. 7.21. (a) Longitudinal and (b) transverse current distribution of the EH_1 mode at $f = 5 \text{ GHz}$ (leaky regime (iii)) and $f = 10 \text{ GHz}$ (bound regime (i)) for the microstrip line with finite thickness with $w = 1.5 \text{ cm}$, $d = 0.794 \text{ mm}$, $t/w = 0.1$, $\epsilon_r = 2.32$.

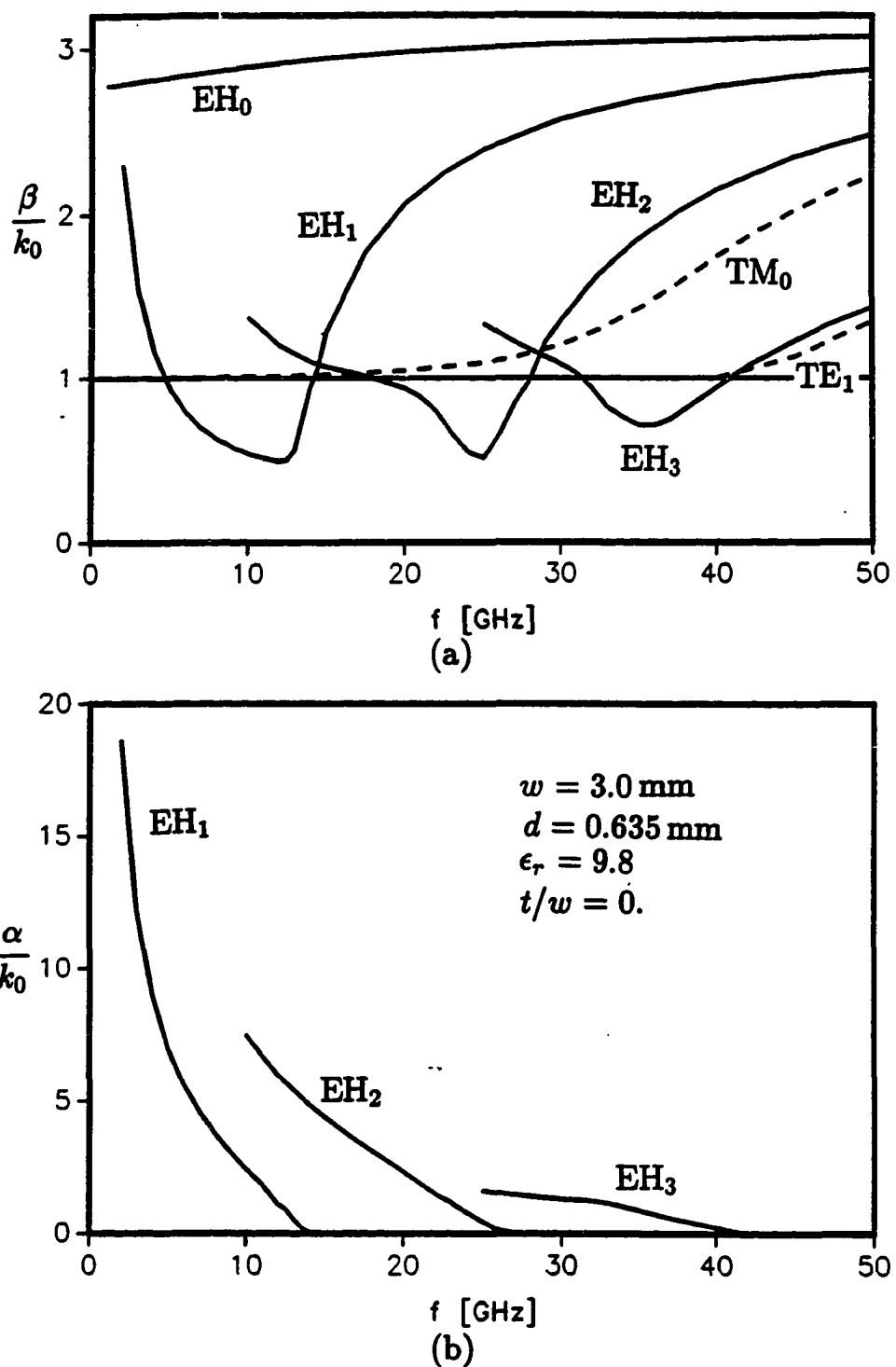


Fig. 7.22. Variation with frequency (a) of the normalized phase constant for the lowest mode (EH_0) and the first three higher modes (EH_1 , EH_2 , EH_3), and (b) of the normalized attenuation constant for the EH_1 , EH_2 and EH_3 modes. The microstrip line dimensions are: $w = 3 \text{ mm}$, $d = 0.635 \text{ mm}$, $t/w = 0$, $\epsilon_r = 9.8$.

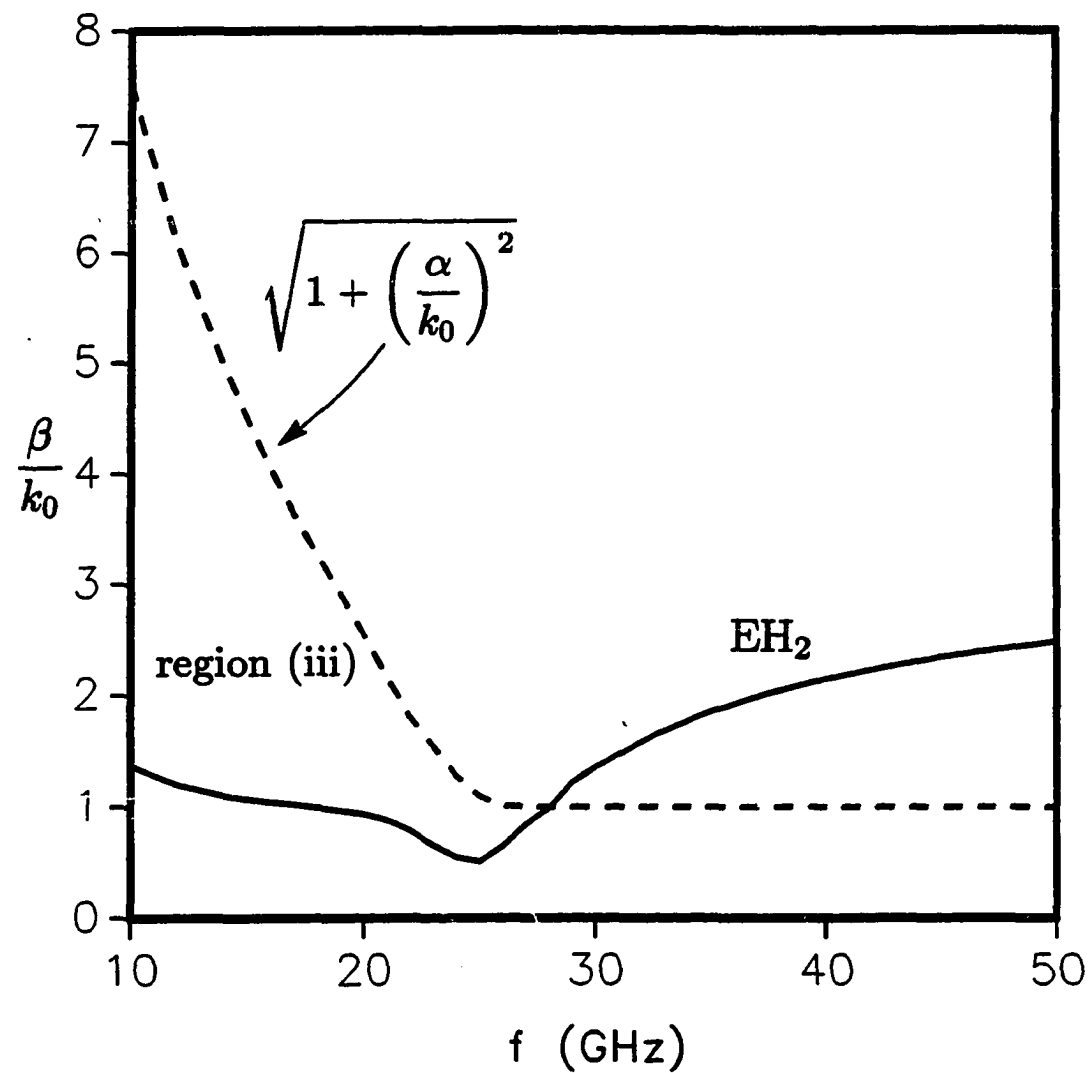


Fig. 7.23. Normalized phase constant for the EH_2 mode and the boundary of region (iii) corresponding to this mode.

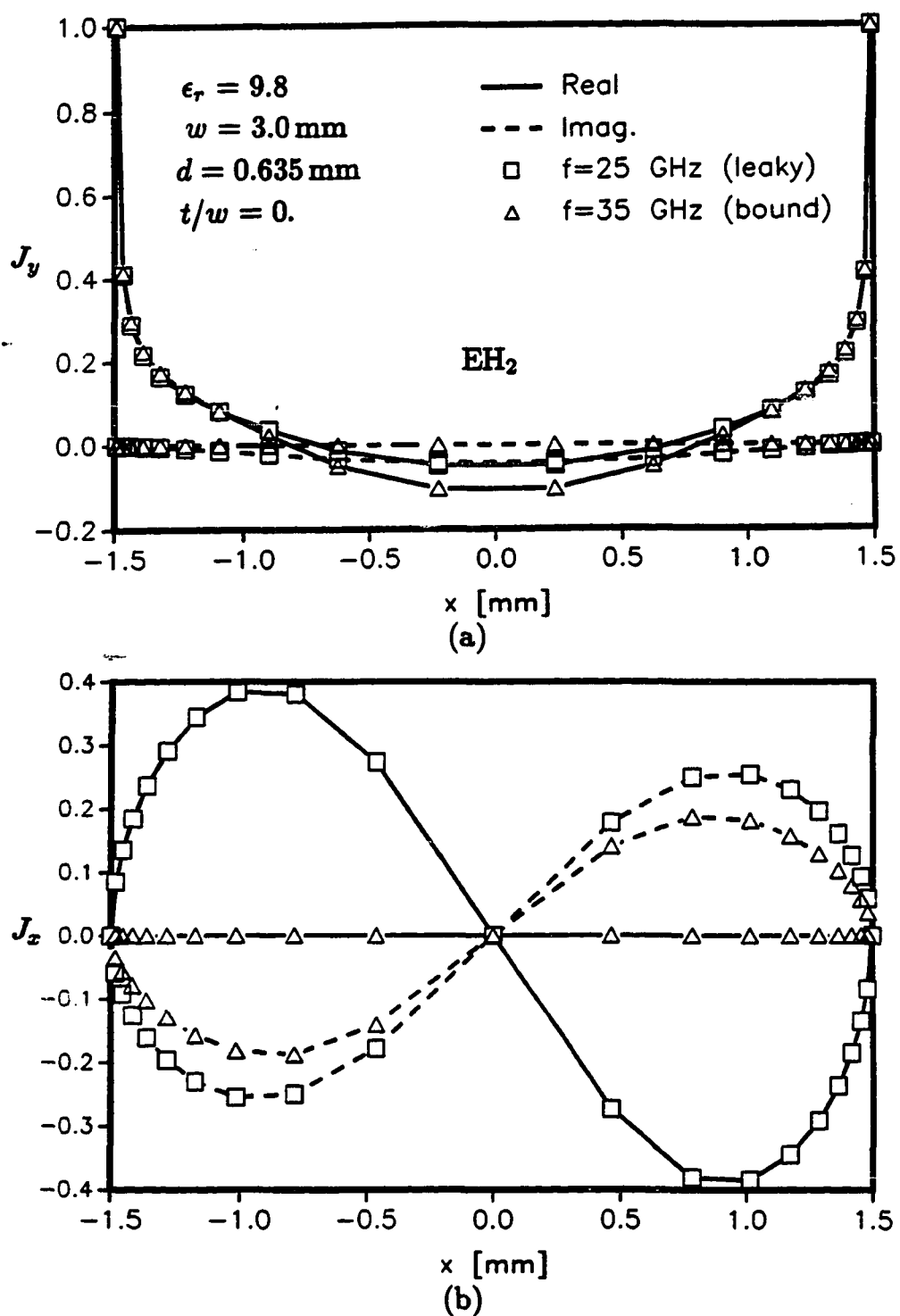


Fig. 7.24. (a) Longitudinal and (b) transverse current distribution of the EH_2 mode at $f = 25 \text{ GHz}$ (leaky regime (iii)) and $f = 35 \text{ GHz}$ (bound regime (i)) for the microstrip line: $w = 3 \text{ mm}$, $d = 0.635 \text{ mm}$, $t/w = 0$, $\epsilon_r = 9.8$.

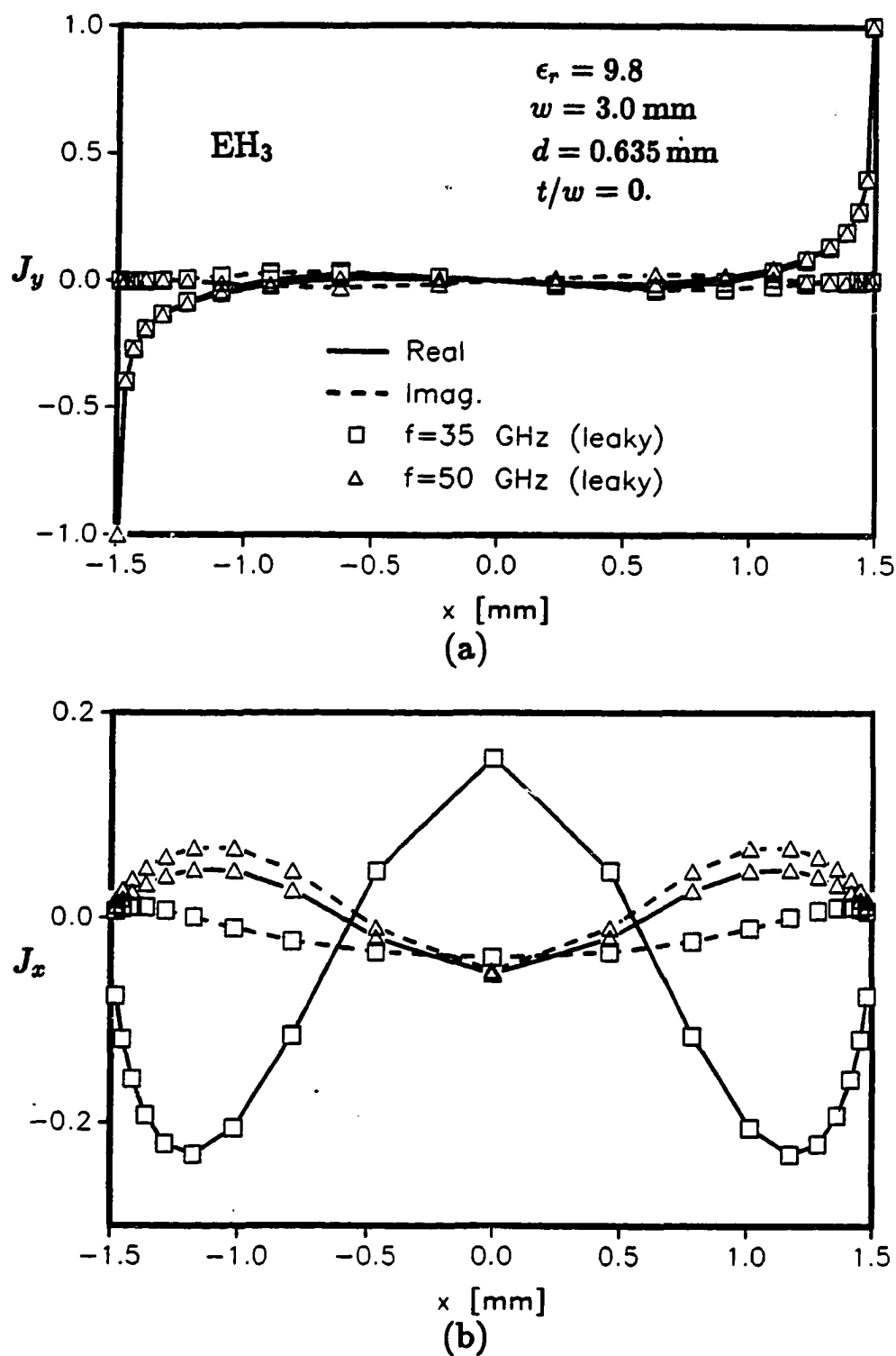


Fig. 7.25. (a) Longitudinal and (b) transverse current distribution of the EH_3 mode at $f = 35 \text{ GHz}$ (leaky regime (iii)) and $f = 50 \text{ GHz}$ (leaky regime (ii)) for the microstrip line with $w = 3 \text{ mm}$, $d = 0.635 \text{ mm}$, $t/w = 0$, $\epsilon_r = 9.8$.

EH_3 mode at $f = 35 \text{ GHz}$ (leaky regime (iii)) and at $f = 50 \text{ GHz}$ (leaky regime (ii)).

In Fig. 7.26, we plot the effective dielectric constant, defined as $\epsilon_{\text{eff}} = (\beta/k_0)^2$, as a function of d/λ_0 , where λ_0 is the free space wavelength, for various widths and thicknesses of the strip. One observes that the effective dielectric constant decreases with the thickness of the strip. This effect is more pronounced at low frequencies.

We should mention that, at this writing, the results for an open microstrip line with finite thickness by a rigorous approach are not available. We only can compare our results with those for a shielded microstrip with finite thickness. The result in Fig. 7.26 has been found to agree favorably with that given in [68] (which is not shown in the figure) for a shielded strip line with a large size of the out shield.

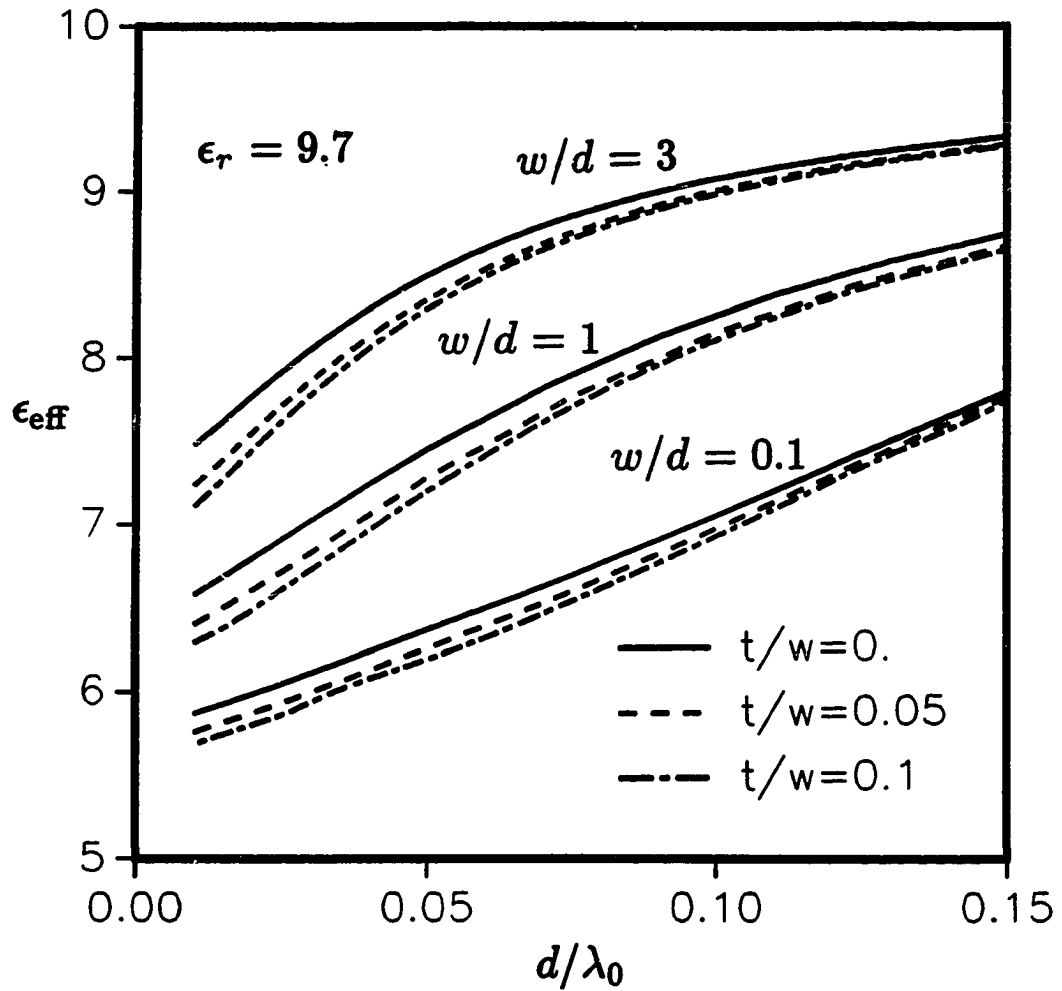


Fig. 7.26. Effective dielectric constant for the lowest mode (EH_0) for a microstrip with $\epsilon_r = 9.7$.

CHAPTER 8

CONCLUSIONS

In this work, a rigorous and general procedure has been developed for the analysis of radiation, scattering, and guidance of electromagnetic fields by conducting objects of arbitrary shape embedded in a medium consisting of an arbitrary number of planar, dielectric layers. The key step in this procedure is the transformation of the electric field integral equation into a mixed-potential form, which is amenable to the well-established numerical solution techniques originally developed for arbitrarily-shaped objects in free space. Three particularly useful mixed-potential integral equations (MPIEs) are derived and their properties discussed. One of the three MPIEs, called Formulation C, which is found to be especially well suited for the application of the moment method, is implemented to analyze arbitrarily-shaped, open or closed, conducting surfaces, which penetrate the interface between contiguous dielectric half-spaces. Thin wire structures are treated as special cases. Formulation C is also specialized to the case of an open transmission line consisting of an infinite conductor of arbitrary cross-section partially embedded in a grounded dielectric slab.

Since at this writing the capability of analyzing the problems of electromagnetic radiation and scattering by three-dimensional PEC surfaces of arbitrary shape in layered media does not exist, the task of validating our results was a difficult one. Data for comparison were only available for thin-wire antennas and for the ground stake antenna. In other cases, we had to rely on the results of two-dimensional analyses. With a few exceptions, our results presented in Chapter 7 compare favorably

with the few available measured and numerical results, thus demonstrating—we believe—the validity of the approach advanced here.

Although open microstrip lines have been analyzed by both spectral-domain [69, 70] and space-domain [71,72] integral equation methods, to our knowledge no results have been published for microstrips of finite thickness. Even for infinitely thin strips, results are only available for the bound modes. This is possibly due to the fact that the integration paths of the spectral-plane integrals that constitute the kernels of the integral equations must be chosen differently for the bound and leaky modes, respectively, as explained in Section 6.2. Hence, a computer code that is successful for bound mode is likely to fail to find a leaky mode, unless special precautions are taken in the program. This prompted some researchers to voice skepticism about the very existence of the leaky modes in a microstrip. We hope that the results presented in Chapter 7 will put to rest the controversy regarding the existence of leaky microstrip modes.

We wish to point out that, at present, matrix fill time, not the available computer memory, is the overriding factor, which puts practical limits on the size of objects that can be analyzed by the technique advanced here. This is due to the fact that the matrix elements comprise improper, Sommerfeld-type integrals, which must be repeatedly evaluated by numerical quadrature, as is discussed in Chapter 6. Although it is possible, and desirable, to develop analytical approximations for the Sommerfeld integrals—and thus drastically reduce the computational expense—we have opted in this work for rigorous treatment of those integrals, to avoid the uncertainties associated with approximations, whose ranges of applicability are usually not well-defined.

Although, for simplicity, we have concentrated in Chapter 5 on the analysis for objects embedded in a two-layer medium, we could almost as easily treat the n -layer case ($n > 2$), for which explicit MPIEs are given in Chapter 4. Also, the approach developed here can be used to analyze arbitrary configurations of surfaces and wires. One could, for example, easily adapt the JUNCTION code [7] for that purpose. As a special case, one could treat the problem of a microstrip antenna driven by a coaxial cable with the inner conductor soldered to the patch. Our method can also be directly used to calculate resonant frequencies of microstrip antennas of arbitrary—possibly exotic—shapes. One could also extend it to analyze infinite arrays of microstrip antennas of arbitrary shape.

Future work in this area might involve dielectric bodies of arbitrary shape in layered media. For homogeneous bodies, one could apply the surface integral formulation in conjunction with the triangle-patch code [6] and for inhomogeneous objects, the volume integral approach in conjunction with the tetrahedral element model [10]. These techniques can also be specialized to the analysis of dielectric waveguides consisting of infinite dielectric slabs of arbitrary cross-section embedded in layered media.

Finally, as was already mentioned, there is room for improvements in the evaluation of the Sommerfeld-type integrals, since most of the computational effort is spent on them.

APPENDIX

KERNEL ELEMENTS OF FORMULATION C FOR CONTIGUOUS HALF-SPACES AND FOR A GROUNDED SLAB

A.1. Kernel Elements for Contiguous Half-Spaces

The expressions for the elements of the kernels in (5-1)–(5-3) can be written down by specializing the formulas given in Section 4.3 to the two-layer case (Fig. 5.1a). Thus, when the source and observation points are in the i th region ($i = 1, 2$), one obtains

$$K_{xx}^{ii} = \frac{\mu_i}{4\pi} \left\{ g_i(|\underline{r} - \underline{r}'|) + \frac{\mu_p - \mu_i}{\mu_1 + \mu_2} g_i(|\underline{r} - \underline{r}''|) - \frac{2\mu_p}{\mu_1 + \mu_2} I_1^{ii} \right\} \quad (\text{A-1})$$

$$K_{xz}^{ii} = \frac{\text{sgn}(z)}{2\pi} \cos \zeta \frac{\mu_i(\mu_p \epsilon_p - \mu_i \epsilon_i)}{(\mu_1 + \mu_2)(\epsilon_1 + \epsilon_2)} \cdot \left\{ \frac{1}{\xi} [e^{-jk_i|z+z'|} - |z+z'| g_i(|\underline{r} - \underline{r}''|)] - I_3^{ii} \right\} \quad (\text{A-2})$$

$$K_{zz}^{ii} = \frac{\mu_i}{4\pi} \left\{ g_i(|\underline{r} - \underline{r}'|) + \left(2 \frac{\epsilon_p - \epsilon_i}{\epsilon_1 + \epsilon_2} + \frac{\mu_p - \mu_i}{\mu_1 + \mu_2} \right) g_i(|\underline{r} - \underline{r}''|) + 2 \left[\frac{\epsilon_i(\mu_p - \mu_i)}{\mu_p \epsilon_i - \mu_i \epsilon_p} - \frac{\mu_p}{\mu_1 + \mu_2} \right] I_1^{ii} - 2 \left[\frac{\mu_i(\epsilon_p - \epsilon_i)}{\mu_p \epsilon_i - \mu_i \epsilon_p} + \frac{2\epsilon_p}{\epsilon_1 + \epsilon_2} \right] I_2^{ii} \right\} \quad (\text{A-3})$$

$$K_\phi^{ii} = \frac{1}{4\pi \epsilon_i} \left\{ g_i(|\underline{r} - \underline{r}'|) - \frac{\epsilon_p - \epsilon_i}{\epsilon_1 + \epsilon_2} g_i(|\underline{r} - \underline{r}''|) \right\}$$

$$- 2 \frac{\epsilon_i(\mu_p - \mu_i)}{\mu_p \epsilon_i - \mu_i \epsilon_p} I_1^{ii} + 2 \left[\frac{\epsilon_p}{\epsilon_1 + \epsilon_2} + \frac{\mu_i(\epsilon_p - \epsilon_i)}{\mu_p \epsilon_i - \mu_i \epsilon_p} \right] I_2^{ii} \quad (\text{A-4})$$

with $K_{zz}^{ii} = -K_{xz}^{ii}$ and $K_{zy}^{ii} = -K_{yz}^{ii}$, where K_{yz}^{ii} is given by (2-4) with $\cos \zeta$ replaced by $\sin \zeta$. In the above, we have introduced the notation (cf. (3-3))

$$I_1^{ii} = S_0 \left\{ \frac{j \mu_i (k_{zi} - k_{zp}) e^{-jk_{zi}|z+z'|}}{\mu_1 k_{z2} + \mu_2 k_{z1}} \right\} \quad (\text{A-5})$$

$$I_2^{ii} = S_0 \left\{ \frac{j \epsilon_i (k_{zi} - k_{zp}) e^{-jk_{zi}|z+z'|}}{\epsilon_1 k_{z2} + \epsilon_2 k_{z1}} \right\} \quad (\text{A-6})$$

$$I_3^{ii} = S_1 \left\{ \left[\frac{(\mu_1 + \mu_2)(\epsilon_1 + \epsilon_2)}{(\mu_1 k_{z2} + \mu_2 k_{z1})(\epsilon_1 k_{z2} + \epsilon_2 k_{z1})} + \frac{1}{k_p^2} \right] e^{-jk_{zi}|z+z'|} \right\} \quad (\text{A-7})$$

$$g_i(r) = \frac{e^{-jk_ir}}{r} \quad (\text{A-8})$$

and $r'' = r' + 2\hat{z}z'$. The index p in (A-1)–(A-7) assumes the values 1 or 2, but not equal to i (i.e., $p = 1, 2$ and $p \neq i$).

When the source point is in region i and the observation point in region $m \neq i$, one obtains

$$K_{xx}^{mi} = \frac{\mu_m}{2\pi} \frac{\mu_i}{\mu_1 + \mu_2} \left\{ g_m(|r - r'|) - I_1^{mi} \right\} \quad (\text{A-9})$$

$$\begin{aligned} K_{xz}^{mi} &= \frac{\text{sgn}(z)}{2\pi} \cos \zeta \frac{\mu_i(\mu_i \epsilon_i - \mu_m \epsilon_m)}{(\mu_1 + \mu_2)(\epsilon_1 + \epsilon_2)} \\ &\cdot \left\{ \frac{1}{\xi} [e^{-jk_m|z-z'|} - |z - z'| g_m(|r - r'|)] - I_3^{ii} \right\} \quad (\text{A-10}) \end{aligned}$$

$$K_{zz}^{mi} = \frac{\mu_m}{2\pi} \left\{ \left[\frac{\mu_i \epsilon_i}{\mu_m (\epsilon_1 + \epsilon_2)} - \frac{\mu_i \epsilon_i - \mu_m \epsilon_m}{\mu_i \epsilon_m - \mu_m \epsilon_i} \left(\frac{\mu_i}{\mu_1 + \mu_2} - \frac{\epsilon_i}{\epsilon_1 + \epsilon_2} \right) \right] \cdot g_m(|\underline{r} - \underline{r}'|) + \frac{\mu_i \epsilon_i - \mu_m \epsilon_m}{\mu_i \epsilon_m - \mu_m \epsilon_i} \frac{\mu_i}{\mu_1 + \mu_2} I_1^{mi} - \frac{\epsilon_1 \epsilon_2}{\epsilon_1 + \epsilon_2} \frac{\mu_i^2 - \mu_m^2}{\mu_m (\mu_i \epsilon_m - \mu_m \epsilon_i)} I_2^{mi} \right\} \quad (\text{A-11})$$

$$K_{\phi}^{mi} = \frac{1}{2\pi} \frac{1}{\epsilon_1 + \epsilon_2} \left\{ g_m(|\underline{r} - \underline{r}'|) - \frac{\epsilon_1 + \epsilon_2}{\mu_i \epsilon_m - \mu_m \epsilon_i} \left[(\mu_i - \mu_m) I_1^{mi} - \frac{\mu_i \epsilon_i - \mu_m \epsilon_m}{\epsilon_1 + \epsilon_2} I_2^{mi} \right] \right\} \quad (\text{A-12})$$

with $K_{xx}^{mi} = -\frac{\mu_m}{\mu_i} K_{zz}^{mi}$ and $K_{zy}^{mi} = -\frac{\mu_m}{\mu_i} K_{yz}^{mi}$, where K_{yz}^{mi} is given by (A-10) with $\cos \zeta$ replaced by $\sin \zeta$. In these equations, we have introduced the notation

$$I_1^{mi} = S_0 \left\{ \left[\frac{j(\mu_1 + \mu_2)}{\mu_1 k_{z2} + \mu_2 k_{z1}} e^{-jk_{zi}|z'|} + \frac{e^{-jk_{zm}|z'|}}{jk_{zm}} \right] e^{-jk_{zm}|z|} \right\} \quad (\text{A-13})$$

$$I_2^{mi} = S_0 \left\{ \left[\frac{j(\epsilon_1 + \epsilon_2)}{\epsilon_1 k_{z2} + \epsilon_2 k_{z1}} e^{-jk_{zi}|z'|} + \frac{e^{-jk_{zm}|z'|}}{jk_{zm}} \right] e^{-jk_{zm}|z|} \right\} \quad (\text{A-14})$$

$$I_3^{mi} = S_1 \left\{ \left[\frac{(\mu_1 + \mu_2)(\epsilon_1 + \epsilon_2) e^{-jk_{zi}|z'|}}{(\mu_1 k_{z2} + \mu_2 k_{z1})(\epsilon_1 k_{z2} + \epsilon_2 k_{z1})} + \frac{e^{-jk_{zm}|z'|}}{k_p^2} \right] e^{-jk_{zm}|z|} \right\}. \quad (\text{A-15})$$

Several comments are in order concerning the form of the above expressions, which resulted—after a considerable amount of manipulations—from the corresponding formulas derived in Section 4.3. The chosen forms have the advantage that most of the contribution to the value of a given kernel element comes from the closed form term, thus deemphasizing the importance of the Sommerfeld-type integral. We also note that for the given \underline{r} and \underline{r}' , only three distinct Sommerfeld integrals are called for. Another advantage of this particular formulation is that the

Sommerfeld integrals are well-behaved, even when $\underline{r} = \underline{r}'$ on the interface.

A.2. Kernel Elements for a Grounded Slab

We now specialize the formulas of Section 4.3 to the grounded slab case (see Fig. 5.1b). When the source and observation points are both in region 1, we obtain

$$K_{xx}^{11} = \frac{\mu_1}{4\pi} \left\{ g_1(|\underline{r} - \underline{r}'|) - S_0 \left[\frac{\mu_1 k_{z2} \cot(k_{z2}d) - j\mu_2 k_{z1}}{D^h} \frac{e^{-jk_{z1}(z+z')}}{jk_{z1}} \right] \right\} \quad (\text{A-16})$$

$$K_{zz}^{11} = -\frac{\mu_1}{2\pi} (\mu_1 \epsilon_1 - \mu_2 \epsilon_2) \cos \zeta S_1 \left\{ \frac{e^{-jk_{z1}(z+z')}}{D^e D^h} \right\} \quad (\text{A-17})$$

$$K_{zx}^{11} = -K_{xz}^{11} \quad (\text{A-18})$$

$$\begin{aligned} K_{zz}^{11} = \frac{\mu_1}{4\pi} & \left\{ g_1(\underline{r} - \underline{r}') + S_0 \left\{ \left[\frac{j\epsilon_2 k_{z1} + \epsilon_1 k_{z2} \tan(k_{z2}d)}{D^e j k_{z1}} \right. \right. \right. \\ & \left. \left. \left. + 2(\mu_2 \epsilon_2 - \mu_1 \epsilon_1) \frac{j k_{z1}}{D^e D^h} \right] e^{-jk_{z1}(z+z')} \right\} \right\} \end{aligned} \quad (\text{A-19})$$

$$\begin{aligned} K_{\phi}^{11} = \frac{1}{4\pi \epsilon_1} & \left\{ g_1(\underline{r} - \underline{r}') - S_0 \left\{ \left[\frac{\mu_1 k_{z2} \cot(k_{z2}d) - j\mu_2 k_{z1}}{D^h j k_{z1}} \right. \right. \right. \\ & \left. \left. \left. + 2(\mu_2 \epsilon_2 - \mu_1 \epsilon_1) \frac{j k_{z1}}{D^e D^h} \right] e^{-jk_{z1}(z+z')} \right\} \right\}. \end{aligned} \quad (\text{A-20})$$

When the source point is in region 1 and the observation point is in region 2 ($i = 1$, $m = 2$), we obtain

$$K_{xz}^{21} = \frac{\mu_2}{2\pi} S_0 \left\{ \frac{\mu_1}{D^h} \frac{\sin[k_{z2}(z+d)]}{\sin(k_{z2}d)} e^{-jk_{z1}z'} \right\} \quad (\text{A-21})$$

$$K_{zz}^{21} = \frac{\mu_1}{2\pi} (\mu_2 \epsilon_2 - \mu_1 \epsilon_1) \cos \zeta S_1 \left\{ \frac{1}{D^e D^h} \frac{\sin[k_{z2}(z+d)]}{\sin(k_{z2}d)} e^{-jk_{z1}z'} \right\} \quad (\text{A-22})$$

$$K_{zz}^{21} = -\frac{\mu_2}{2\pi} (\mu_2 \epsilon_2 - \mu_1 \epsilon_1) \cos \zeta S_1 \left\{ \frac{1}{D^e D^h} \frac{\cos[k_{z2}(z+d)]}{\cos(k_{z2}d)} e^{-jk_{z1}z'} \right\} \quad (\text{A-23})$$

$$K_{zz}^{21} = \frac{1}{2\pi} S_0 \left\{ \left[\frac{\mu_2 \epsilon_2}{D^e} - (\mu_2 \epsilon_2 - \mu_1 \epsilon_1) \frac{\mu_1 k_{z2} \cot(k_{z2}d)}{D^e D^h} \right] \frac{\cos[k_{z2}(z+d)]}{\cos(k_{z2}d)} e^{-jk_{z1}z'} \right\} \quad (\text{A-24})$$

$$K_\phi^{21} = \frac{1}{2\pi} S_0 \left\{ \frac{j\mu_1 k_{z1} - \mu_2 k_{z2} \tan(k_{z2}d)}{D^e D^h} \frac{\sin[k_{z2}(z+d)]}{\sin(k_{z2}d)} e^{-jk_{z1}z'} \right\}. \quad (\text{A-25})$$

When the source point is in region 2 and the observation point is in region 1 ($i = 2$, $m = 1$), we obtain

$$K_{zz}^{12} = \frac{\mu_1}{2\pi} S_0 \left\{ \frac{\mu_2}{D^h} \frac{\sin[k_{z2}(z'+d)]}{\sin(k_{z2}d)} e^{-jk_{z1}z} \right\} \quad (\text{A-26})$$

$$K_{zz}^{12} = -\frac{\mu_1}{2\pi} (\mu_1 \epsilon_1 - \mu_2 \epsilon_2) \cos \zeta S_1 \left\{ \frac{1}{D^e D^h} \frac{\cos[k_{z2}(z'+d)]}{\cos(k_{z2}d)} e^{-jk_{z1}z} \right\} \quad (\text{A-27})$$

$$K_{zz}^{12} = \frac{\mu_1}{2\pi} (\mu_1 \epsilon_1 - \mu_2 \epsilon_2) \cos \zeta S_1 \left\{ \frac{1}{D^e D^h} \frac{\sin[k_{z2}(z'+d)]}{\sin(k_{z2}d)} e^{-jk_{z1}z} \right\} \quad (\text{A-28})$$

$$K_{zz}^{12} = \frac{1}{2\pi} S_0 \left\{ \left[\frac{\mu_1 \epsilon_1}{D^e} - (\mu_1 \epsilon_1 - \mu_2 \epsilon_2) \frac{j k_{z1}}{D^e D^h} \right] \frac{\cos[k_{z2}(z'+d)]}{\cos(k_{z2}d)} e^{-jk_{z1}z} \right\} \quad (\text{A-29})$$

$$K_\phi^{12} = \frac{1}{2\pi} S_0 \left\{ \frac{j\mu_1 k_{z1} - \mu_2 k_{z2} \tan(k_{z2}d)}{D^e D^h} \frac{\sin[k_{z2}(z'+d)]}{\sin(k_{z2}d)} e^{-jk_{z1}z} \right\}. \quad (\text{A-30})$$

Finally, when the source and observation points are in region 2 ($i = 2, m = 2$), we obtain

$$K_{zz}^{22} = \frac{\mu_2}{2\pi} S_0 \left\{ \frac{-j\mu_2 k_{z1} + \mu_1 k_{z2} \cot(k_{z2} z_>)}{D^h} \frac{\sin(k_{z2} z_>) \sin[k_{z2}(z_< + d)]}{k_{z2} \sin(k_{z2} d)} \right\} \quad (\text{A-31})$$

$$K_{zz}^{22} = \frac{\mu_2}{2\pi} (\mu_2 \epsilon_2 - \mu_1 \epsilon_1) \cos \zeta S_1 \left\{ \frac{1}{D^h D^e} \frac{\sin[k_{z2}(z + d)]}{\sin(k_{z2} d)} \frac{\cos[k_{z2}(z' + d)]}{\cos(k_{z2} d)} \right\} \quad (\text{A-32})$$

$$K_{zz}^{22} = -\frac{\mu_2}{2\pi} (\mu_2 \epsilon_2 - \mu_1 \epsilon_1) \cos \zeta S_1 \left\{ \frac{1}{D^h D^e} \frac{\sin[k_{z2}(z' + d)]}{\sin(k_{z2} d)} \frac{\cos[k_{z2}(z + d)]}{\cos(k_{z2} d)} \right\} \quad (\text{A-33})$$

$$\begin{aligned} K_{zz}^{22} = & \frac{\mu_2}{2\pi} S_0 \left\{ \frac{-j\epsilon_2 k_{z1} + \epsilon_1 k_{z2} \cot(k_{z2} z_>)}{D^e} \frac{\sin(k_{z2} z_>) \cos[k_{z2}(z_< + d)]}{k_{z2} \cos(k_{z2} d)} \right. \\ & \left. - (\mu_2 \epsilon_2 - \mu_1 \epsilon_1) \frac{k_{z2}}{D^h D^e} \frac{\cos[k_{z2}(z + d)] \cos[k_{z2}(z' + d)]}{\sin(k_{z2} d) \cos(k_{z2} d)} \right\} \quad (\text{A-34}) \end{aligned}$$

$$\begin{aligned} K_{\phi}^{22} = & \frac{1}{2\pi \epsilon_2} S_0 \left\{ \frac{-j\mu_2 k_{z1} + \mu_1 k_{z2} \cot(k_{z2} z_>)}{D^h} \frac{\sin(k_{z2} z_>) \sin[k_{z2}(z_< + d)]}{k_{z2} \sin(k_{z2} d)} \right. \\ & \left. - (\mu_2 \epsilon_2 - \mu_1 \epsilon_1) \frac{k_{z2}}{D^h D^e} \frac{\sin[k_{z2}(z + d)] \sin[k_{z2}(z' + d)]}{\cos(k_{z2} d) \sin(k_{z2} d)} \right\} \quad (\text{A-35}) \end{aligned}$$

where $z_<$ and $z_>$ denote, respectively, the lesser and the greater of z and z' . K_{yz}^{mi} and K_{zy}^{mi} ($m = 1, 2, i = 1, 2$) are given by K_{zz}^{mi} and K_{zz}^{mi} , respectively, with $\cos \zeta$ replaced by $\sin \zeta$. In the above equations, we have introduced the notation

$$D^h = j\mu_2 k_{z1} + \mu_1 k_{z2} \cot(k_{z2} d) \quad (\text{A-36})$$

$$D^e = j\epsilon_2 k_{z1} - \epsilon_1 k_{z2} \tan(k_{z2} d). \quad (\text{A-37})$$

REFERENCES

- [1] R. F. Harrington, *Field Computation by Moment Methods*. New York: Macmillan, 1968.
- [2] A. W. Glisson, "On the development of numerical techniques for treating arbitrarily-shaped surfaces," Ph.D. dissertation, Dept. Elec. Eng., Univ. Mississippi, 1978.
- [3] D. R. Wilton, "Wire problems," in *Numerical and Asymptotic Techniques for Electromagnetics and Antennas* (R. F. Harrington and R. Mittra, eds.), Syracuse Univ. and Univ. Illinois, 1979.
- [4] A. W. Glisson and D. R. Wilton, "Simple and efficient numerical methods for problems of electromagnetic radiation and scattering from surfaces," *IEEE Trans. Antennas Propagat.*, vol. AP-28, pp. 593-603, Sept. 1980.
- [5] S. M. Rao, D. R. Wilton, and A. W. Glisson, "Electromagnetic scattering by surfaces of arbitrary shape," *IEEE Trans. Antennas Propagat.*, vol. AP-30, pp. 409-418, May 1982.
- [6] K. Umashankar, A. Taflove, and S. M. Rao, "Electromagnetic scattering by arbitrary shaped three-dimensional homogeneous lossy dielectric objects," *IEEE Trans. Antennas Propagat.*, vol. AP-34, pp. 758-766, June 1986.
- [7] S. U. Hwu and D. R. Wilton, "Electromagnetic scattering and radiation by arbitrary configurations of conducting bodies and wires," Technical Report No. 87-17, Applied Electromagnetics Lab., Dept. of Electrical Engr., Univ. of Houston, Dec. 1987.
- [8] J. J. H. Wang, "Numerical analysis of three-dimensional arbitrarily-shaped conducting scatterers by trilateral surface cell modelling," *Radio Sci.*, vol. 13, pp. 947-952, Nov.-Dec. 1978.
- [9] A. J. Poggio and E. K. Miller, "Integral equation solutions of three-dimensional scattering problems," in *Computer Techniques for Electromagnetics* (R. Mittra, ed.), pp. 159-264, New York: Pergamon Press, 1973.
- [10] D. H. Schaubert, D. R. Wilton, and A. W. Glisson, "A tetrahedral modeling method for electromagnetic scattering by arbitrarily shaped inhomogeneous dielectric bodies," *IEEE Trans. Antennas Propagat.*, vol. AP-32, pp. 77-85, Jan. 1984.

- [11] W. A. Johnson, D. R. Wilton, and R. M. Sharpe, *PATCH CODE User's Manual*. Sandia National Laboratories, Albuquerque, N. M., 1988.
- [12] J. W. Rockway, J. C. Logan, D. W. S. Tam, and S. T. Li, *The MININEC System: Microcomputer Analysis of Wire Antennas*. Boston: Artech House, 1988.
- [13] J. C. Logan and J. W. Rockway, "The new MININEC (version 3): A mini-numerical electromagnetic code," Technical Report No. 938, Naval Ocean Systems Center, San Diego, CA, Sept. 1986.
- [14] A. Erteza and B. K. Park, "Nonuniqueness of resolution of Hertz vector in presence of a boundary, and a horizontal dipole problem," *IEEE Trans. Antennas Propagat.*, vol. AP-17, pp. 376–378, May 1969.
- [15] K. A. Michalski, "On the scalar potential of a point charge associated with a time-harmonic dipole in a layered medium," *IEEE Trans. Antennas Propagat.*, vol. AP-35, pp. 1299–1301, Nov. 1987.
- [16] A. Sommerfeld, *Partial Differential Equations*. New York: Academic Press, 1949.
- [17] J. R. Mosig and F. E. Gardiol, "A dynamical radiation model for microstrip structures," in *Advances in Electronics and Electron Physics* (P. W. Hawkes, ed.), vol. 59, pp. 139–237, New York: Academic Press, 1982.
- [18] J. R. Mosig and F. E. Gardiol, "General integral equation formulation for microstrip antennas and scatterers," *IEE Proc.*, vol. 132, Pt. H, pp. 424–432, Dec. 1985.
- [19] W. A. Johnson, "Analysis of a vertical, tubular cylinder which penetrates an air-dielectric interface and which is excited by an azimuthally symmetric source," *Radio Sci.*, vol. 18, pp. 1273–1281, Nov.-Dec. 1983.
- [20] D. R. Wilton and S. Singh, "Analysis of an infinite periodic array of slots with dielectric loading," *1985 AP-S Int. Symp.*, Vancouver, Canada, pp. 229–232, 1985.
- [21] K. A. Michalski, C. E. Smith, and C. M. Butler, "Analysis of a horizontal two-element antenna array above a dielectric halfspace," *IEE Proc.*, vol. 132, Pt. H, pp. 335–338, Aug. 1985.

- [22] K. A. Michalski and C. E. Smith, "Analysis of parallel monopole antennas residing in contiguous media," *Nat'l Radio Sci. Meeting Digest*, p. 230, Boulder, CO, Jan. 13-16, 1986.
- [23] K. A. Michalski, "On the dyadic Green's function for a grounded dielectric slab," *Nat'l Radio Sci. Meeting Digest*, p. 93, Boston, MA, June 25-29, 1984.
- [24] K. A. Michalski, "The mixed-potential electric field integral equation for objects in layered media," *Arch. Elek. Übertragung.*, vol. 39, pp. 317-322, Sept.-Oct. 1985.
- [25] X. B. Xu, "Analysis of TM- and TE- excited cylinders in a region comprising two semi-infinite half-spaces separated by a planar interface," Ph.D. dissertation, Dept. Elec. Eng., Univ. Mississippi, 1985.
- [26] G. J. Burke and E. K. Miller, "Modeling antennas near to and penetrating a lossy interface," *IEEE Trans. Antennas Propagat.*, vol. AP-32, pp. 1040-1049, Oct. 1984.
- [27] G. J. Burke, "The numerical electromagnetics code (NEC)," in *Applications of the Method of Moments to Electromagnetic Fields* (B. J. Strait, ed.), pp. 449-469, St. Cloud, Florida: The SCEEE Press, 1980.
- [28] G. W. Hohmann, "Three-dimensional EM modeling," *Geophys. Surv.*, vol. 6, pp. 27-53, 1983.
- [29] P. E. Wannamaker, G. W. Hohmann, and W. A. SanFilipo, "Electromagnetic modeling of three-dimensional bodies in layered earths using integral equations," *Geophysics*, vol. 49, pp. 60-74, Jan. 1984.
- [30] A. Karlsson and G. Kristensson, "Electromagnetic scattering from subterranean obstacles in a stratified ground," *Radio Sci.*, vol. 18, pp. 345-356, May-June 1983.
- [31] R. F. Harrington, *Time-Harmonic Electromagnetic Fields*. New York: McGraw-Hill, 1961.
- [32] A. Baños, *Dipole Radiation in the Presence of a Conducting Half-Space*. New York: Pergamon Press, 1966.
- [33] B. D. Popovic, M. B. Dragovic, and A. R. Djordjevic, *Analysis and Synthesis of Wire Antennas*. Chichester: Research Studies Press, 1982.

- [34] M. Chiba, "Singularities of Green's function in surface integral equations," *Electronics and Communications in Japan*, vol. 66-B, no. 11, pp. 85–93, 1983.
- [35] O. D. Kellogg, *Foundations of Potential Theory*. New York: Dover, 1953.
- [36] J. G. Fikioris, "Electromagnetic field inside a current-carrying region," *J. Math. Phys.*, vol. 6, pp. 1617–1620, Nov. 1965.
- [37] J. Van Bladel, *Electromagnetic Fields*. Washington: Hemisphere, 1985.
- [38] M. Marcuvitz and J. Schwinger, "On the representation of the electric and magnetic field produced by currents and discontinuities in wave guides," *J. Appl. Phys.*, vol. 22, pp. 806–819, June 1951.
- [39] L. B. Felsen and N. Marcuvitz, *Radiation and Scattering of Waves*. Englewood Cliffs, N.J.: Prentice Hall, 1973.
- [40] K. A. Michalski and D. Zheng, "Analysis of wire antennas of arbitrary shape residing in contiguous half-spaces," *5th Int. Conf. Antennas Propagat. (ICAP 87)*, York, UK, pp. 507–511, 1987.
- [41] D. R. Wilton, S. M. Rao, A. W. Glisson, D. H. Schaubert, O. M. Al-Bundak, and C. M. Butler, "Potential integrals for uniform and linear source distributions on polygonal and polyhedral domains," *IEEE Trans. Antennas Propagat.*, vol. AP-32, pp. 276–281, Mar. 1984.
- [42] A. Hessel, "General characteristics of traveling-wave antennas," in *Antenna Theory Part II* (R. E. Collin and J. Zucker, eds.), pp. 151–258, New York: McGraw-Hill, 1969.
- [43] M. Siegel and R. W. P. King, "Electromagnetic fields in a dissipative half-space—a numerical approach," *J. Appl. Phys.*, vol. 41, pp. 245–2423, May 1970.
- [44] W. C. Kuo and K. K. Mei, "Numerical approximations of the Sommerfeld integrals for fast convergence," *Radio Sci.*, vol. 13, pp. 407–415, May-June 1978.
- [45] C. C. Lin and K. K. Mei, "Radiation and scattering from partially buried vertical wires," *Electromagn.*, vol. 2, pp. 309–334, Oct.-Dec. 1982.

- [46] P. B. Katehi and N. G. Alexopoulos, "Real axis integration of Sommerfeld integrals with applications to printed circuit antennas," *J. Math. Phys.*, vol. 24, pp. 527–533, Mar. 1983.
- [47] W. A. Johnson and D. G. Dudley, "Real axis integration of Sommerfeld integrals: Source and observation points in air," *Radio Sci.*, vol. 18, pp. 175–186, Mar.-Apr. 1983.
- [48] J. R. Mosig and F. E. Gardiol, "Analytic and numerical techniques in the Green's function treatment of microstrip antenna and scatterers," *IEE Proc.*, vol. 130, Pt. H, pp. 175–182, Mar. 1983.
- [49] E. K. Miller, A. J. Poggio, and E. S. Selden, "Analysis of wire antennas in the presence of a conducting half-space. Part I: The vertical antenna in free space," *Can. J. Phys.*, vol. 50, pp. 879–888, 1972.
- [50] T. K. Sarkar, "Analysis of arbitrarily oriented thin wire antennas over a plane imperfect ground," *Arch. Elek. Übertragung.*, vol. 31, pp. 449–457, 1977.
- [51] G. J. Burke, E. K. Miller, J. N. Brittingham, D. L. Lager, R. J. Lytle, and J. T. Okada, "Computer modeling of antennas near the ground," *Electromagn.*, vol. 1, pp. 29–49, Jan.-Mar. 1981.
- [52] K. A. Michalski and C. M. Butler, "Evaluation of Sommerfeld integrals arising in the ground stake antenna problem," *IEE Proc.*, vol. 134, Pt. H, pp. 93–97, Feb. 1987.
- [53] J. A. Fuller and J. R. Wait, "A pulsed dipole in the earth," in *Transient Electromagnetic Fields* (L. B. Felsen, ed.), pp. 237–269, New York: Springer, 1976.
- [54] J. A. Kong, L. C. Shen, and L. Tsang, "Field of an antenna submerged in a dissipative dielectric medium," *IEEE Trans. Antennas Propagat.*, vol. AP-25, pp. 887–889, Nov. 1977.
- [55] V. Hansen, "Approximate equations for the nearfield of a horizontal electric dipole on a grounded dielectric slab," *IEE Proc.*, vol. 129, Pt. H, pp. 29–31, Feb. 1982.
- [56] L. Grun and Y. Rahmat-Samii, "Polynomial approximations of Bessel, Neumann and Hankel functions for complex arguments," Technical Report No. 77-15, Electromagnetics Lab., Dept. Elec. Eng., Univ. Illinois, July 1977.

- [57] M. Abramowitz and I. A. Stegun, eds., *Handbook of Mathematical Functions*. New York: Dover, 1965.
- [58] H. Hurwitz and P. F. Zweifel, "Numerical quadrature of Fourier transform integrals," *Math. Tables Aids Comput.*, vol. 10, pp. 140-149, 1956.
- [59] L. M. Brekhovskikh, *Waves in Layered Media*. New York: Academic Press, 1980.
- [60] H. Erment, "Guiding and radiation characteristics of planar waveguides," *IEE Microwave, Optics and Acoustics*, vol. 3, pp. 59-62, Mar. 1979.
- [61] A. A. Oliner, "Leakage from higher modes on microstrip line with application to antennas," *Proc. URSI Int. Symp. on Electromagnetic Theory*, pp. 25-27, Budapest, Hungary, Aug. 1986.
- [62] A. A. Oliner and K. S. Lee, "The nature of the leakage from higher modes on microstrip line," *IEEE MTT-S Digest*, pp. 57-60, 1986.
- [63] T. T. Wu, "Theory of the microstrip," *J. Appl. Phys.*, vol. 28, pp. 299-302, Mar. 1957.
- [64] C. M. Butler and K. A. Michalski, "Analysis of a cylindrical antenna residing in two contiguous half spaces," Nat'l Radio Sci. Meeting, Boulder, CO, January 5-7, 1983.
- [65] C. E. Smith, C. M. Butler, C. A. Harrison, and K. A. Michalski, "An experimental investigation of antenna configurations which are near to or pass through an air-water interface," Final Report to the Naval Ocean Systems Center, San Diego, CA, Dept. Elec. Eng., Univ. Mississippi, June 1984.
- [66] A. A. Oliner and K. S. Lee, "Microstrip leaky wave strip antennas," *Digest of the AP-S Int'l Symp.*, pp. 443-446, Philadelphia, PA, Aug. 1986.
- [67] D. C. Chang and E. F. Kuester, "Total and partial reflection from the end of a parallel-plate waveguide with an extended dielectric slab," *Radio Sci.*, vol. 16, no. 1, pp. 1-13, Jan.-Feb. 1981.
- [68] G. Kowalski and R. Pregla, "Dispersion characteristics of shielded microstrips with finite thickness," *Arch. Elek. Übertragung.*, vol. 25, pp. 193-196, Apr. 1971.

- [69] T. Itoh and R. Mittra, "Spectral domain approach for calculating the dispersion characteristics of microstrip lines," *IEEE Trans. Microwave Theory Techn.*, vol. MTT-21, pp. 496-499, July 1973.
- [70] M. Kobayashi and F. Ando, "Dispersion characteristics of open microstrip lines," *IEEE Trans. Microwave Theory Techn.*, vol. MTT-35, pp. 101-105, Feb. 1987.
- [71] J. M. Grimm and J. S. Bagby, "Alternative integral formulation for analysis of microstrip transmission lines," *Digest of the URSI Nat'l Radio Sci. Meeting*, p. 113, Boulder, CO, Jan. 1988.
- [72] N. Fachè and D. De Zutter, "Rigorous full-wave space-domain solution for dispersive microstrip lines," *IEEE Trans. Microwave Theory Techn.*, vol. MTT-36, pp. 731-737, Apr. 1988.

BIOGRAPHICAL SKETCH OF THE AUTHOR

Dalian Zheng was born in Liaoning, China, on May 30, 1955. He received the B.E. degree in Electrical Engineering from the Beijing Institute of Aeronautics and Astronautics, Beijing, China, 1982, and the M.S. degree in Electrical Engineering from the Ohio State University, Ohio, in 1985.

Mr. Zheng worked as a Research Assistant in the Department of Electrical Engineering at the University of Mississippi from July 1985 to May 1987. Since June 1987 he has been a Research Assistant in the Department of Electrical Engineering at the Texas A&M University.

Mr. Zheng is a Student Member of the IEEE.